الجمهــــورية الجـــــزائرية الديمقـــــراطية الشعبيـــــة

REPUBLIQUE ALGERIENNE DEMOCRATIQUE ET POPULAIRE

وزارة التـــــعليم العـــــالــــي و البحث العلمـــــي

MINISTERE DE L'ENSEIGNEMENT SUPERIEUR

ET DE LA RECHERCHE SCIENTIFIQUE

جامعــــة فرحــــات عبـــــاس ـ سطيف 1

UNIVERSITE FERHAT ABBAS - SETIF 1

UFAS (ALGERIE)

THESE

Présentée à la Faculté de Technologie

Département d'Électronique

Pour l'Obtention du Diplôme de

DOCTORAT 3ème cycle (LMD)

Domaine : Sciences et Technologies

Filière : Electronique

Option : Électronique et Contrôle Industriel

Par

Hamza FEROURA

Stratégies de Commande des Onduleurs de Courant Triphasés

Soutenue le: 24 /06 /2018   devant le jury composé de:

Nourredine AMARDJIA	Professeur à l'université de Sétif 1	Président
Fateh KRIM	Professeur à l'université de Sétif 1	Rapporteur
Adel MELLIT	Professeur à l'université de Jijel	Examinateur
Lahcene ZIÉT	HDR à l'université de Sétif 1	Examinateur

الجمهـــورية الجـــزائرية الديمقـــراطية الشعبيـــة

PEOPLE'S DEMOCRATIC REPUBLIC OF ALGERIA

وزارة التـــعليم العـــالـــي و البحث العلمـــي

MINISTERY OF HIGHER EDUCATION

AND SCIENTIFIC RESEARCH

جامعـــة فرحـــات عبـــاس – سطيف 1

UNIVERSITY FERHAT ABBAS - SETIF 1

UFAS (ALGERIA)

THESIS

Presented at the Faculty of Technology

Department of Electronics

For the Graduation of

Ph. D. 3rd Cycle (LMD)

Field : Sciences and Technologies

Specialty : Electronics

Option : Electronics and Industrial Control

by

Hamza FEROURA

Control Strategies of Three Phase Current Source Inverters.

Defended on: 24 /06 /2018   in front of the jury composed of:

Nourredine AMARDJIA	Professor at university of Setif 1	President
Fateh KRIM	Professor at university of Setif 1	Reporter
Adel MELLIT	Professor at university of Jijel	Examiner
Lahcene ZIET	HDR at university of Setif 1	Examiner

Abstract

Current Source Inverter (CSI) topology is gaining acceptance as a competitive alternative for grid interface of renewable energy systems due to its unique and advantageous features. Merits of CSI over the more popular voltage source inverter (VSI) topology have been elaborated on by a number of researchers. However, there is a lack of quality work in control strategies of CSI topology for both stand-alone and grid connected modes. Therefore this thesis contributes by proposing new voltage control techniques, and power control techniques for stand-alone and grid-connected modes, respectively. Existing voltage control techniques for stand-alone CSI are conventional, and complex. They employ usually modulators and regulation loops which are designed depending on the connected load, this reduces the accuracy and stability of the controllers. For this reason, two direct voltage control methods have been proposed in this work. The proposed methods overcome the aforementioned drawbacks of conventional methods. In the other side, PV grid connected CSI systems available in the literature suffer from many problems such like complexity of control strategies, poor power control, filter resonance, and low efficiency. Therefore, new high-performance control strategies are introduced to get over these problems. The proposed techniques can fulfill all the control objectives of the system, i.e. fast and accurate maximum power point tracking, decoupled control of active and reactive powers exchanged with the grid, low distorted grid currents, unity power factor operation or reactive power injection, depending on grid operator demand, and high efficiency through the use of active damping methods. Moreover, system cost and complexity are reduced, and better performances are reached by the use of a sliding mode observer (SMO) instead of hardware sensors. Simulation results using Matlab/Simulink, experimental results, and real-time (RT) implementation results have been carried out to assess the different control techniques proposed in this thesis.

Acknowledgement

First and above all, I praise the almighty **ALLAH** for granting me the capability to proceed successfully. This thesis would not have been possible without the support of several individuals who in one way or another contributed their valuable assistance in the completion of this work.

I would like to express my utmost gratitude and thanks to my academic supervisor, **Pr. Fateh KRIM**, who has advised, guided and supported me throughout this research work.

I would like to express my thanks to the examiners committee, **Pr. Nourredine AMARDJIA**, **Dr. Lahcene ZIÉT**, and **Pr. Adel MELLIT** for their valued time and interests in my thesis.

Special thanks to all the members of our laboratory group (**LEPCI**), and to all my colleagues.

I am so grateful to **Dr. Miguel CASTILLA**, and **Pr. Luis Garcia DE VICUNA** for giving me the opportunity to have a long duration training at their laboratory in Barcelona. My thanks go also to all the laboratory group.

Finally, I would like to acknowledge the financial support of the Algerian ministry of higher education and scientific research that have granted me a long duration training abroad.

Dedications

Dedicated

To my parents;

To my wife;

To my sister and my brothers;

And to my friends.

Hamza Feroura

Contents

List of tables

List of figures

XIII

List of abbreviations

AC	Alternating current
DC	Direct current
DG	Distributed generation
SG	Smart grid
RES	Renewable energy source
GHG	Greenhouse gas
SMES	Superconducting magnetic energy storage
ICT	Information and communication technology
VSI	Voltage source inverter
MVSI	Multi-level VSI
NPC	Neutral point clamped
CHB	Cascaded H-bridge
ASCI	Auto-Sequentially commutated inverter
LCI	Load commutated inverter
CSI	Current source inverter
CSR	Current source rectifier
MCSI	Multi-level CSI
PV	Photovoltaic
MPP	Maximum power point
MPPT	Maximum power point tracking (tracker)
P&O	Perturb & observe
PWM	Pulse width modulation
SPWM	Sinusoidal PWM
CSPWM	Carrier based SPWM
TPWM	Trapezoidal PWM
SVM	Space vector modulation
SHE	Selective harmonic elimination
THD	Total harmonic distortion
IGBT	Insolated gate bipolar transistor

RB-IGBT	Reverse blocking-IGBT
GCT	Gate commutated thyristor
CL	Capacitive-inductive
TF	Transfer function
PI	Proportional integral
PR	Proportional resonant
SRF	Synchronously rotating frame
PLL	Phase locked loop
FS	Finite-Set
MPC	Model predictive control
VOC	Voltage oriented control
DPC	Direct power control
RL	Resistive-inductive
SMO	Sliding mode observer
HIL	Hardware-in-the-loop
RT	Real-time
PCB	Printed circuit board

List of symbols

The following provides definition to the symbols that are commonly used in this thesis. Other symbols which only appear in specific sections are defined in the context where they appear.

a, b, c	Natural frame components
d, q	synchronously rotating reference frame components
α, β	stationary reference frame components
I_{pv}	PV array current
V_{pv}	PV array voltage
P_{pv}	PV array power
I_{dc}	DC link current
I_o	CSI output current
I_g	Grid current
V_g	Grid voltage
I_c	Capacitor current
V_c	Capacitor voltage
I_L	Load current
V_L	Load voltage
ε	Voltage error
P	Active power
P_{dc}	DC-side power
P_{ac}	AC-side active power
Q	Reactive power
θ	Grid voltage vector angle
ω	Grid angular pulsation
C_f	Filter capacitance
L_f	Filter inductance
R_f	Internal filter inductor resistance
L_{dc}	DC link inductor inductance
R_{dc}	Internal DC link inductor resistance
R_d	Damping resistor

XVII

s	Laplace operator
K_p	Proportional gain
K_i	Integral gain
ΔI	P&O step-size
$\overrightarrow{I_{ref}}$	Reference current vector
$\vec{I_1}\ to\ \vec{I_9}$	CSI current vectors
$S_1\ to\ S_6$	Inverter power switches
S	Sliding surface
T_s	Sampling time
g	Cost function
$(\ )_{op}$	Index of optimal value
k	Actual sampling instant
G	Irradiance
T	Temperature
R_s	PV Series resistance
R_p	PV parallel resistance
I_d	Diode current
V_d	Diode voltage
I_{ph}	Photovoltaic current
I_o	Saturation current
V_{oc}	Open-circuit voltage
I_{sc}	Short-circuit current
V_t	Thermal voltage
$(\ )_n$	Index of nominal value
$(\ )_{,cell}$	Index of cell value
q	Electron charge $q = 1.60217646 \times 10^{-19}$ C
E_g	Semiconductor band gap energy
a	Diode ideality constant
k	Boltzmann constant $k = 1.3806503 \times 10^{-23}$ J/K

XVIII

Chapter 1

Introduction

1.1 Background and motivation

Electric energy consumption has been growing dramatically over the past few years to meet the energy needs related to global population and high economic growth [1.1]-[1.3]. Currently fossil fuels present the majority of electricity productions, approximately 78.4% [1.1]. The burning of fossil fuels release carbon dioxide and other greenhouse gases (GHG), as well as, many other pollutants such as sulfur dioxide and nitrogen oxides. The carbon dioxide released when fossil fuels are burned is leading to global climate change. Global GHG emissions have increased with 70% between 1970 and 2016. During this same time period, global GHG emissions from the electric energy sector have increased with about 145% [1.4].

Demand for clean, economical, and renewable energy has increased consistently over the past few decades, especially as a consequence of the energy crisis and environmental issues such as global warming and pollution. There has been a significant progress in the development of renewable energy sources such as biomass, hydropower, solar photovoltaic energy, and wind energy [1.5]-[1.16]. Approximately 19.3% of global electricity production in the world is from renewable energy sources (RES) [1.1]. The sub-divisions of RES percentages are depicted in Figure1.1
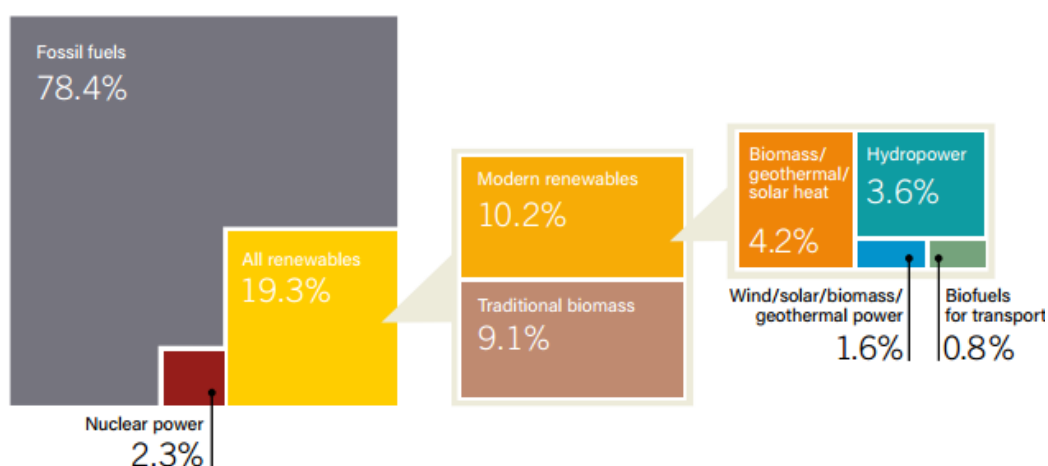
Figure 1.1 Estimated renewable energy share of total final energy consumption, 2016 [1.1]

Among a variety of renewable energy resources available, solar energy appears to be a major contender due to its abundance and pollution-free conversion to electricity through photovoltaic (PV) process [1.5]-[1.16]. PV energy installed capacity has increased exponentially over the recent years, and has become a real alternative to boost renewable energy penetration [1.1]-[1.3], Figure 1.2 shows the worldwide cumulative PV power installed.
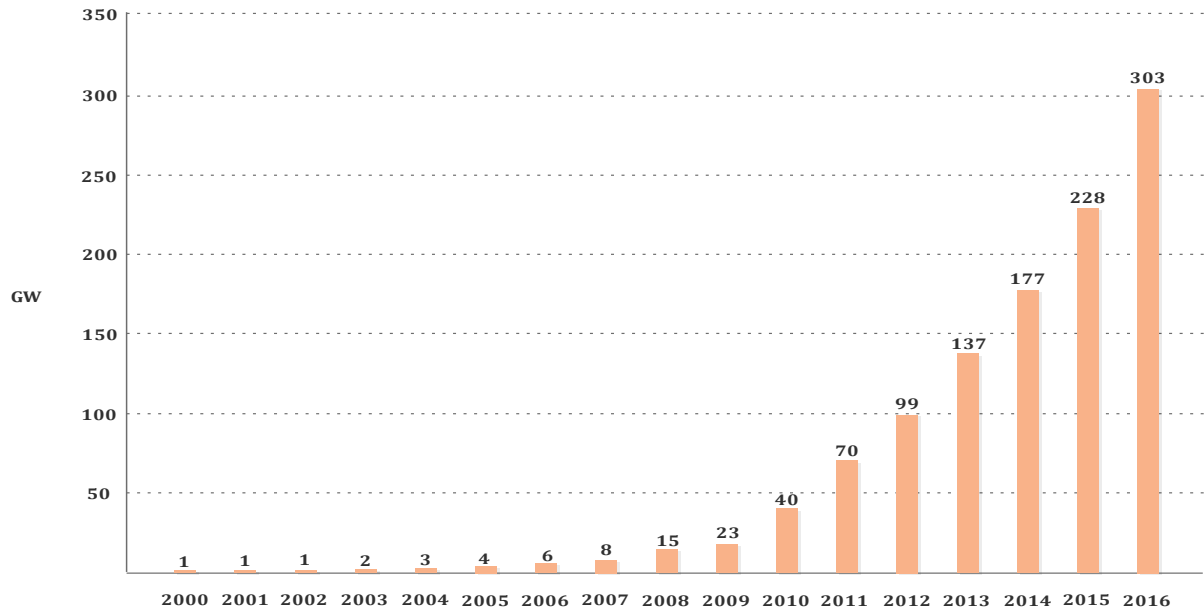
Figure 1.2 Evolution of cumulative PV installations (GW). [1.2]

Increasing interest in PV systems, demands growth in research and development activities in various aspects such as Maximum Power Point Tracking (MPPT), PV arrays, anti-islanding protection, stability and reliability, power quality and power electronic interface [1.15]. With increase in penetration level of PV systems in the existing power systems, these issues are expected to become more critical in time since they can have noticeable impact on the overall system performance [1.4]-[1.10]. More efficient and cost-effective PV modules are being developed and manufactured, in response to the concerns raised by the PV system developers, utilities and customers [1.4], [1.8], [1.13]. Numerous standards have been designed to address power quality and grid-integration issues [1.6]. Extensive research in the field of MPPT has resulted in fast and optimized method to track the maximum power point [1.13], [1.15].

Regarding power electronic converters to interface PV arrays to the grid, voltage source inverter (VSI) is the most used topology to date [1.16]-[1.18]. However, this topology has some limitation when it comes to PV applications. The VSI topology has buck (step-down) characteristics; therefore to step-up the low voltage output from the PV array, an extra power

electronic converter is required, this is known as dual-stage topology [1.17], [1.18]. These drawbacks can be overcome by the use another type of inverters known as Current source inverters (CSIs). CSIs appear to be direct competitors of VSIs, especially in medium, and high power applications, due to the advantages listed below [1.19]-[1.23]:

✓ CSI outputs grid and motor friendly waveforms. Its AC voltage and current waveforms are close to sinusoidal with low harmonics distortion. It also inherently avoids high *dv/dt* resulting from filtering effect of output capacitors.

✓ DC-side current regulation offers an inherent current limiting, over-current, and short-circuit protection features during AC-side faults.

✓ The most important feature of CSI is the boosting capability, namely it can operate with a low-voltage DC source. Thus, AC voltages required in certain applications such like uninterruptible power supply (UPS) can be obtained from a low battery voltage in one single power stage. On the other hand, PV sources can be interfaced to grid using CSI in a single-stage topology. This decreases the power losses and increases the system's efficiency in comparison with dual-stage topologies.

Despite CSI's many favorable features for PV application, its use has been limited due to the following drawbacks [1.19]-[1.25]:

o The on-state losses in the switching elements, where the semiconductor switches used are not capable of withstanding negative voltage, and thus have to be connected in series with a diode, this makes CSI losses higher than those in VSI. However, with new advances in the power semiconductor technologies, CSI switching losses have been reduced to great extent; since, insolated gate bipolar transistor (IGBT) in series with diodes could now be replaced by only one component, which is reverse-blocking IGBT (RB-IGBT).

o The losses in the DC inductor of CSI are known to be higher than those in the DC capacitor of the VSI. However, with recent developments in Superconducting Magnetic Energy Storage (SMES) technology, there is hope that concerns regarding inductor can be removed in the future.

o The AC-side filter capacitors can resonate with the filter's inductance or distribution line inductance.

o The complexity of the control techniques represents one of the major drawbacks of CSI.

Though researchers have studied CSI for different applications, there still exist many points that could be investigated and improved.

Motivated by the huge demand for solar energy and immediate need for improvements in PV systems, the research reported in this thesis intends to add to the existing knowledge on PV system applications of CSI and make quality contributions to the field.

1.2 Objectives

The main objectives of the research can be summarized as follows:

- To achieve a complete survey on CSIs, in terms of working principle, modeling, design, and existing modulation and control techniques.
- To develop new control strategies for voltage control of CSI that could be used when switching from grid-connected to stand-alone modes due to grid disconnection of local loads during islanding of DG systems. The developed techniques should ensure fast and accurate voltage and frequency control and should also pass the robustness tests.
- To develop new control strategies for single-stage three phase PV grid connected CSI. The developed strategies should be capable of extracting maximum power from the PV arrays at all insolation levels, and injecting a clean sinusoidal current into the power grid in accordance with grid codes.
- To develop a sliding mode observer (SMO) observer for AC-side that must be able to estimate the required variables accurately.
- To introduce active resonance damping methods for PV grid connected CSI to increase the systems efficiency and enhance the power quality.

1.3 Thesis outline

To achieve the aforementioned objectives and facilitate the presentation of results derived in the course of this research, the thesis is organized as follows:

- ❖ **Chapter 2** Provides a literature survey on distributed generation systems in the first part. Then, an overview of inverter topologies is presented. In the next section of the

chapter, the existing inverters modulation techniques and control strategies are studied and explained. Finally, literature reviews on stand-alone and grid connected CSI are performed.

❖ **Chapter 3** Presents the design and modeling of the different components of the systems of this research. First, the PV panel has been modeled using the equivalent single diode circuit. Then, the model of CSI and its possible switching states and space vectors are exhibited. Finally, the design and modeling of the output filter have been studied.

❖ **Chapter 4** Proposes new voltage control strategies for stand-alone CSIs. The developed techniques ensure a fast and accurate voltage control independently of the type of the load, directly, i.e. without any regulations loops, and with no modulators. Simulation results using Matlab/Simulink of the proposed techniques has been carried out for different loads and during different tests. In the last part of this chapter, experimental results for a low power CSI prototype controlled by a digital signal processor (DSP) are exposed.

❖ **Chapter 5** develops a single-stage grid connected PV system based on CSI. First, it has been presented the different parts of the control strategies proposed in this chapter. Starting by the PV MPPT, where perturb and observe (P&O) algorithm is chosen due to its simplicity and good performance. A SMO is proposed for the grid-side variables estimation in order to reduce system's cost and complexity and avoid sensor noise. After that, two novel control techniques both based on model predictive control (MPC) have been analyzed. Besides that, an active damping method for each technique is introduced instead of passive damping method. Simulation results and real-time (RT) implementation results are presented and discussed in the last part of this chapter.

❖ **Chapter 6** presents the conclusions, the contributions of this research, and the recommendations for future work plans.

References

[1.1]   "Renewables 2017, Global Status Report" [Online]. Available:
         http://www.iea-pvps.org

[1.2]   "Trends in Photovoltaic Applications 2017" [Online]. Available:
         http://www.iea-pvps.org

[1.3]   "Global Trends in Renewable Energy Investment 2017" [Online]. Available:
         http://fs-unep-centre.org

[1.4]   C. Bauer, K. Treyer, T. Heck, S. Hirschberg, "Greenhouse Gas Emissions from
         Energy Systems, Comparison, and Overview," *Encyclopedia of the
         Anthropocene*, Vol. 1, No. 1, Jan. 2018, pp. 473–484

[1.5]   F. Blaabjerg, D. M. Ionel, "Renewable Energy Devices and Systems – State-of-
         the-Art Technology, Research and Development, Challenges and Future
         Trends," *Electric Power Components and Systems*, Vol. 43, No. 12, Jul. 2015,
         pp. 1319–1328

[1.6]   M. G. Simoes, F. A. Farret, *Modeling Power Electronics and Interfacing Energy
         Conversion Systems*, John Wiley & Sons, Ltd, 2017.

[1.7]   Y. Wu, J. Lin, H. Lin, "Standards and Guidelines for Grid-connected
         Photovoltaic Generation Systems: a Review and Comparison," *IEEE Trans. on
         Industry Applications*, Vol. 53, No. 4, Mar. 2017, pp. 3205–3216

[1.8]   A. Anzalchi, A. Sarwat, "Overview of Technical Specifications for Grid-
         Connected Photovoltaic Systems," *Energy Conversion and Management*, Vol.
         152, No. 15, Nov. 2017, pp. 312–327

[1.9]   O. P. Mahela, A. G. Shaik, "Comprehensive Overview of Grid Interfaced Solar
         Photovoltaic Systems," *Renewable and Sustainable Energy Reviews*, Vol. 68,
         No. 1, Feb. 2017, pp. 316–332

[1.10]   F. L. Lyo, H. Ye, *Advanced DC/AC Inverters Application in Renewable Energy*.
         CRC Press, 2013.

[1.11]   D. Rekioua, E. Matagne, *Optimisation of Photovoltaic Power Systems:
         Modelisation, Simulation, and Control*. Springer-Verlag, 2012.

[1.12]   H. Abu-Rub. M. Malinowski, K. Al-Haddad, *Power Electronics for Renewable
         Energy Systems, Transportation, and Industrial Applications*. John Wiley &
         Sons, Ltd, 2015.

[1.13] Z. Mirhassani, H. C. Ong, W. T. Chong, K. Y. Lyong , "Advances and Challenges in Grid Tied Photovoltaic Systems," *Renewable and Sustainable Energy Reviews*, Vol. 49, No. 1, Sep. 2015, pp. 121–131

[1.14] Q. Zhong, T. Hornik, *Control of Power Inverters in Renewable Energy and Smart Grid Integration*. John Wiley & Sons, Ltd, 2013.

[1.15] N. Femia, G. Petrone, G. Spagnuolo, M. Vitelli, *Power Electronics and Control Techniques for Maximum Energy Harvesting in Photovoltaic Systems*. CRC Press, 2013.

[1.16] R. Teodorescu. M. Liserre, P. Rodriguez, *Grid Converters for Photovoltaic and Wind Power Systems*. John Wiley & Sons, Ltd, 2011.

[1.17] M. Islam, S. Mekhilef, M. Hasan "Single Phase Transformerless Inverter Topologies for Grid-tied Photovoltaic System: A Review," *Renewable and Sustainable Energy Reviews*, Vol. 45, No. 1, May. 2015, pp. 69–86

[1.18] C. Photong, C. Klumpner, P. Wheeler, "Evaluation of Single-Stage Power Converter Topologies for Grid-Connected Photovoltaics," *in Proc. IEEE Int. Conf. on Industrial Technology*, Chile, 2010, pp. 1161–1168.

[1.19] B. Sahan, S. V. Araujo, C. Noding, P. Zacharias, "Comparative Evaluation of Three-Phase Current Source Inverters for Grid Interfacing of Distributed and Renewable Energy Systems," *IEEE Trans. on Power Electronics*, Vol. 26, No. 8, Aug. 2011, pp. 2304–2318

[1.20] B. K. Bose, *Modern Power Electronics and AC drives*, Prentice Hall PTR, 2002.

[1.21] B. Wu, *High-power Converters and AC drives*, John Wiley & Sons, Ltd, 2006.

[1.22] M. H. Rashid, *Power Electronics Handbook, Third Edition*, Butterworth-Heinemann, Ltd, 2011.

[1.23] P. P. Dash, M. Kazerani, "Dynamic Modeling and Performance Analysis of a Grid-Connected Current-Source Inverter-Based Photovoltaic System," *IEEE Trans. on Sustainable Energy*, Vol. 2, No. 4, Oct. 2011, pp. 443–450

[1.24] Y. W. Li, "Control and Resonance Damping of Voltage-Source and Current-Source Converters With LC Filters," *IEEE Trans. on Industrial Electronics*, Vol. 56, No. 5, Nov. 2008, pp. 1511–1521

[1.25] S. Jayalath, M. Hanif, "CL-Filter Design for Grid Connected CSI," *in Proc. IEEE 13th Brazilian Power Electronics Conf.*, Brazil, 2015, pp. 1–6.

Chapter 2

Literature survey

2.1 Introduction

The rapid depletion of fossil based energy resources such as coal, natural gas and oil, together with an effort to reduce CO2 emission into the atmosphere has required a demand for a larger share of clean energy to be produced from renewable energy sources (RES). Recently, there has been a great interest on distributed generation (DG) in order to replace the conventional electrical distribution systems and achieve better performance and management of energy. In this chapter; a brief review on DG trends has been presented. DG systems can be sourced by different renewable energy sources such as photovoltaic (PV), wind, and others. The focus in this chapter was on photovoltaic energy, where the electricity generation process is discussed and the possible grid integration configurations are presented. Generally, there exist two configuration single- and dual-stage. In dual-stage configuration the generator side converter is responsible for the extraction of the maximum power, whereas the grid-side converter is responsible for injecting the resulting power in a suitable form. Nevertheless, in single-stage configuration the inverter can fulfill both control objectives. A classification and description of the most common inverter topologies used to interface PV systems is done in the third part of this chapter. In the next section, different modulation techniques of current source inverter (CSI) have been exposed and analyzed. Finally literature reviews on stand-alone and grid-connected CSIs are completed to evaluate the state of the art of available control strategies.

2.2 Distributed generation systems

The existing power grids can be considered as a hierarchical systems where power plants are at the top of the chain and loads are at the bottom, resulting in a unidirectional electrical power flow managed with limited informations about the exchange between sources and terminal points. This situation present serious drawbacks, including the following [2.1]-[2.2]:

o   System sensitivity to voltage and frequency instabilities as well as to power security problems caused by load variations and dynamic network reconfigurations.

o   Risks of failures and blackouts and decreased system efficiency.

o   Unsuitability for the integration of renewable energy.

During the last decade, the electrical energy market has been characterized by a growing demand for energy and two important innovations: the quick growth and massive diffusion of RESs and the subsequent rapid development of DG systems and smart grids (SGs) [2.1]–[2.5]. The basic gist of DG is the process of generating energy close to its point of delivery. So, rather than having a big power plant (coal, nuclear, hydroelectric, etc.) that generates massive amounts of energy, which is then transmitted over a vast and complicated network of power lines and transfer stations to be delivered to eventual homeowners or businesses, smaller power plants that generate a moderate amount of energy are located at closer proximity to the homes and businesses that will use it. [2.2]

According to many analyses, future electrical systems should have the following parameters [2.2],[2.3]:

➢   High power capability: electricity is becoming the main power source of the modern world and hence the need for it will increase significantly during the next years, this trend is expected to remain positive for many decades and will be marginally influenced by external perturbations such as economic or political crises.

➢   High power quality and reliability: electricity must be available whenever it is needed with the lowest or no latency, stable voltage and frequency and low harmonic distortion.

➢   High efficiency: electricity should not be dispersed during production, transportation and distribution processes. The grid and the loads should be managed to achieve maximum system efficiency.

➢   High flexibility: the power system should be highly configurable and should allow smooth integration among different power sources, moreover, dynamic changes of loads and power sources should not influence system performance and power quality.

➢   Low environmental impact: renewable energy sources should progressively replace traditional polluting sources.

Previous requirements cannot be satisfied by conventional power systems, therefore, during the next years a huge revision of the present systems is expected with the introduction of many new functionalities, systems, commonly referred to as DG and SG revolution. This is changing the way in which next generation power systems have to be designed, operated and maintained,

and can be achieved only by introducing new technologies, functionalities and operational approaches, which are as follows [2.1]–[2.3]:

- ✓ Full exploitation of all renewables.
- ✓ Technological enhancements and large-scale diffusion of energy storage systems.
- ✓ Massive introduction of Information and Communication Technologies (ICTs).
- ✓ Implementation of high-granularity self-healing and resiliency against unwanted situations, such as blackouts or natural disasters.
- ✓ Consumers' active participation to the electricity market.
- ✓ Introduction of new products, services and markets.

2.2.1 Distributed generators

As it has been mentioned above, it is necessary for the engineering society to pay more interest on the researches of RESs. There exist many forms of renewable energy resources that are currently available for the integration into the power grid, the top four energy sources are wind, solar photovoltaic, hydroelectric, and geothermal. Only photovoltaic generator will be discussed in this section, since it presents the subject of this research.

2.2.1.1 Photovoltaic generators

PV cells are direct current (DC) generators which use semiconductor technology to transform the energy in sunlight into electricity. Silicon is the most widely used semiconductor material in PV cell, which consists of a junction consisting of n- and p-doped silicon. When light (photons) strikes the junction, the energy in the photons is converted to electric power. The voltage level of PV cells depends on the intrinsic cell characteristics, the number of cascaded cells and their temperature, whereas the available current depends on cell characteristics, the number of parallel strings (a string is a group of cascaded cells) and sunlight irradiation. With present technology, they are arranged in panels providing up to 220–250 W at a voltage rating of 48–60 V [2.6],[2.7].

In order to supply standard loads operating with alternating current (AC), panels are connected in series and/or in parallel, thus reaching the desired level of voltage and current, to supply an inverter [2.7]. PV sources can also feed the distribution grid using a suitable conversion chain. Generally a PV system connected to the grid can be either in single- or dual-stage configurations. Figure 2.1. However, single-stage configuration can fulfill all the control objectives with lower switching losses, and thus, providing higher efficiency. [2.2],[2.6],[2.7]
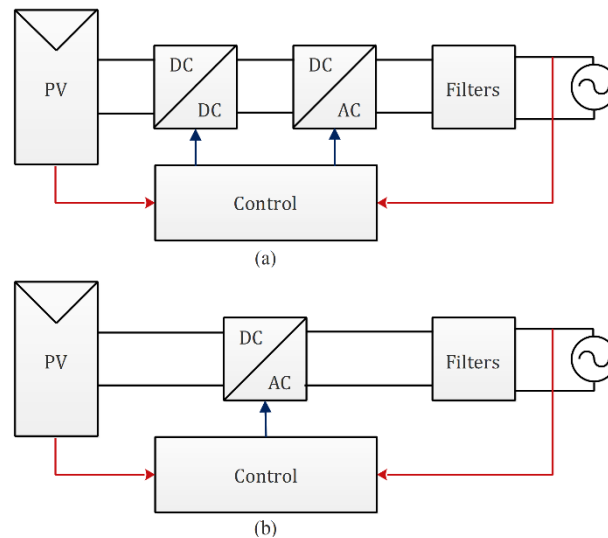
Figure 2.1 Schematic diagram of photovoltaic grid-connected system configurations:

(a) Single-stage (b) Dual-stage.

2.3 Inverter topologies

The power electronic interface is an important part of DG units as it influences the overall system efficiency and performance [2.7]. Many converter types have been used for this purpose, depending on the DG source, system requirements, and control objectives. In PV applications, DC-DC converters and DC-AC inverters are needed to ensure MPPT and efficient power conversion into AC loads. However, in single-stage configuration only DC-AC inverters are required to interface PV sources to the distribution grid.

Fundamentally, as shown in Figure 2.2, there are two types of inverters existed, the voltage source inverter (VSI) and the current source inverter (CSI). In general, an inverter that exploits the input voltage while producing controlled output voltage is classified as VSI whereas an inverter that exploits the input current while producing controlled output current is classified as CSI. The VSI is the more mature and proven technology where it has been successfully implemented in industry for decades [2.6]-[2.10]. While the 2-Level VSI has found applications in many conventional industrial machines, the multi-level VSIs (MVSIs) are more recent and established in industry due to their advantages in particular the ability to generate multilevel stepped-waveform with reduced harmonic distortion, and to reach higher voltage operation, and higher modularity [2.6]. On the other hand, the auto-sequentially commutated inverter (ASCI) and the load-commutated inverters (LCI) and are among the earliest inverters used for variable speed drives before slowly being replaced by the pulse-width modulation (PWM) CSI mostly

in induction motor drives. Quite recently, similar to the VSIs, multi-level CSIs (MCSIs) are gaining attention in new research activities [2.8],[2.10]. While both types of inverters have substantial differences topologically, they do share the same working principles. Thus, in general, common control methods and common power semiconductor switches used for VSI can also be applied to CSI with some modifications.
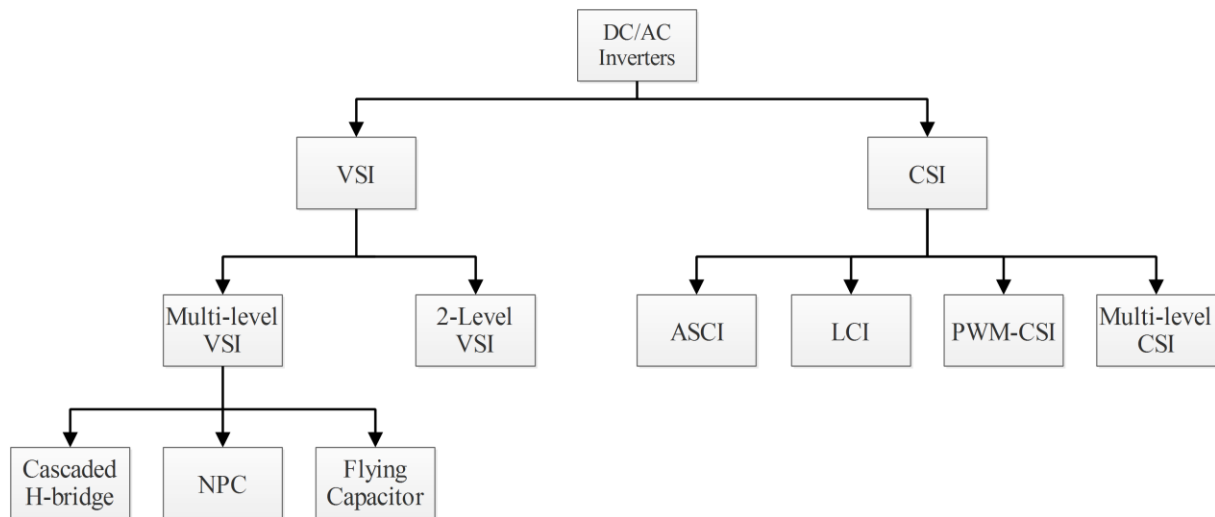
Figure 2.2 Inverters classification

Today the majority of the worldwide installed power inverters are VSIs followed by CSIs. CSIs are available in industrial drives, and have also been connected to wind power and solar power generators and fuel cell systems. Comparison between VSIs and CSIs have been reported many times [2.11] concluding that the decision lies with the performance of the application. Both inverters, however, face the same challenges. Generally they have to be small, light and cost-effective and technically they have to operate at high efficiencies, produce low harmonics, and be simple to control and reliable. For high voltage and high current application this has led to the introduction of multi-level topologies, first for VSIs like the diode-clamped, flying capacitor and cascaded topologies and later to CSIs [2.6]-[2.10]. With the dominating VSI market research into MCSI has been limited. The reason for the lag of interest is, beside the dominance of the VSI in the market, the large component count that is required to build MCSI in particular for a level higher than five i.e. an existing nine-level CSI requires three inductors and twelve power switches. This number goes up rapidly when upgrading the inverter to even higher level of currents. For example a seventeen-level CSI can have seven inductors and twenty power switches.

2.3.1 Voltage source inverters

The primary function of a VSI is to convert a fixed DC voltage to a three-phase AC voltage with variable magnitude and frequency. This section discusses the different VSI topologies used commonly in DG systems, and highlights description and features of each one. The topologies discussed are two-level and multi-level VSI. MVSI can be subdivided into three main topologies: cascaded H-bridge (CHB), diode-clamped, flying capacitor.

2.3.1.1 Two-level VSI

A simplified circuit diagram for a two-level VSI for high-power medium-voltage applications is shown in Figure 2.3. The inverter is composed of six groups of active switches with a free-wheeling diode in parallel with each switch. Depending on the DC operating voltage of the inverter, each switch group consists of two or more IGBT or gate commutated thyristor (GCT) switching devices connected in series [2.6]-[2.10].
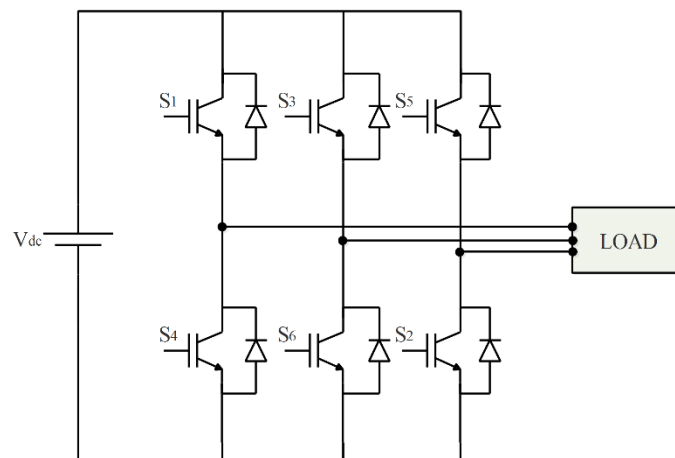
Figure 2.3 Three phase VSI

2.3.1.2 Multi-level VSIs

A. Cascaded H-bridge

CHB multilevel inverter is one of the popular converter topologies used in high-power medium-voltage (MV) drives. It is composed of a multiple units of single-phase H-bridge power cells. The H-bridge cells are normally connected in cascade on their AC side to achieve medium-voltage operation and low harmonic distortion [2.7].

B. Neutral point clamped inverters

The diode-clamped multilevel inverter employs clamping diodes and cascaded DC capacitors to produce AC voltage waveforms with multiple levels. The inverter can be generally configured as a three or more levels topology, but only the three-level inverter, often known as neutral-point clamped (NPC) inverter, has found wide application in high-power medium-voltage drives. The main features of the NPC inverter include reduced *dv/dt* and THD in its AC output voltages in comparison with the two-level inverter discussed earlier. More importantly, the inverter can be used in the medium voltage drive to reach a certain voltage level without switching devices in series. [2.7]-[2.10]

C. Multi-level flying capacitor

It is evolved from the two-level inverter by adding DC capacitors to the cascaded switches. There are four complementary switch pairs in each of the inverter legs. Therefore, only four independent gate signals are required for each inverter phase. The flying-capacitor inverter can produce an inverter phase voltage with five voltage levels. [2.7]

2.3.2 Current source inverters

The CSI (also called current fed inverter) converts the input DC current into three phase AC currents. In CSI, the input current remains constant but could be adjustable. The output currents of a CSI are independent of the load. Nevertheless, the load voltage are dependent of load. This section discusses the different three phase CSI topologies which are subdivided according to their type of commutation into forced-commutated, and natural commutated CSIs (PWM CSIs). The forced-commutated CSIs which are ASCI and LCI represent the earliest types of CSIs. However, the development of power electronics and fast switching devices have permitted lately the appearance of two-level and multi-level (parallel) PWM CSIs.

2.3.2.1 Auto-sequentially commutated inverter

The conventional auto-sequentially commutated inverter (ASCI) shown in Figure 2.5 has six thyristors connected in series with a diode for each. A respective commutating capacitor is interconnected between the junctures of the thyristor and diode of each respective branch sub-circuit and the thyristor and diode of the next adjacent branch sub-circuit. ASCI inverters were developed especially for high power variable-speed drives. The major drawbacks of this topology is limited control strategies applicable since a thyristor cannot be switched off. [2.10]
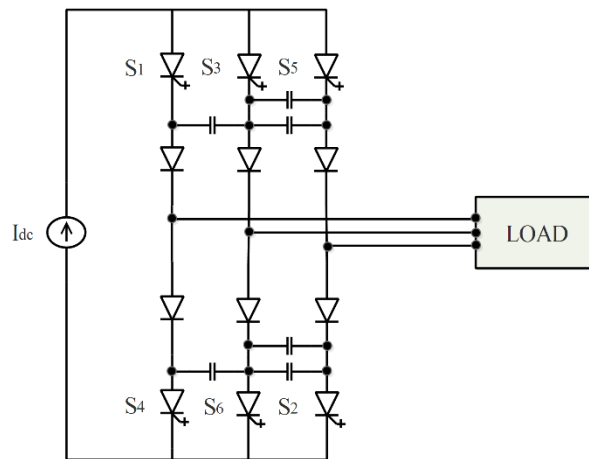
Figure 2.4 Auto-Sequentially commutated inverter

2.3.2.2 Load commutated CSI

The thyristor-based LCI is also one of the earliest inverters developed for variable-speed drives. A three-phase LCI has three parallel legs represented by two series connected thyristors per leg, which in total requires six thyristors. An AC capacitor filter is installed at the output of LCI in order to reduce harmonics content. As shown in Figure 2.6, the thyristor switches are numbered according to their firing sequence. The same major drawback reported for ASCIs is present for LCI, since a thyristor can only be switched on intentionally, Therefore, the most common control technique applied is the six-step switching, in which each thyristor conducts for 120° degrees interval. [2.10]
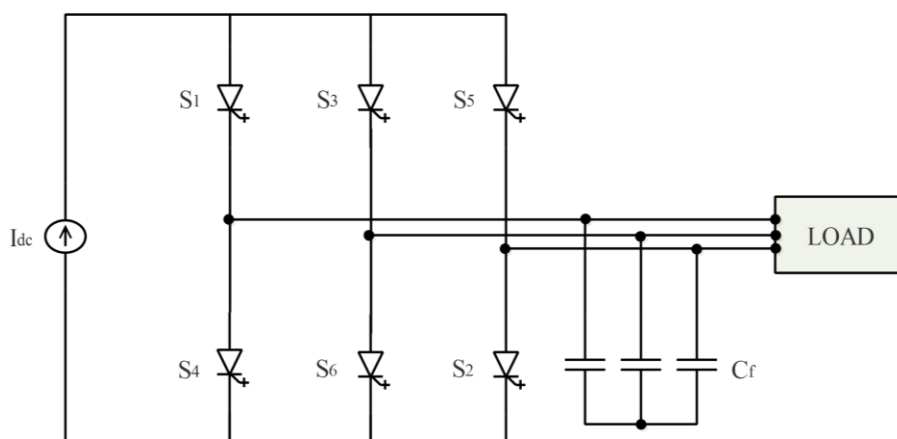
Figure 2.5 Load commutated CSI

2.3.2.3 Two-level CSI

An idealized PWM CSI is shown in Figure 2.4. The inverter is composed of six unidirectional devices, each of which can be replaced with two or more devices in series for medium-voltage

operation. The switching devices used in the CSI are of symmetrical type with a reverse voltage blocking capability. The inverter produces a defined PWM output current. The DC side of the inverter is an ideal DC current source I_{dc}. In practice, I_{dc} can be obtained by a current source rectifier (CSR) or a current controlled buck converter [2.8]-[2.10].
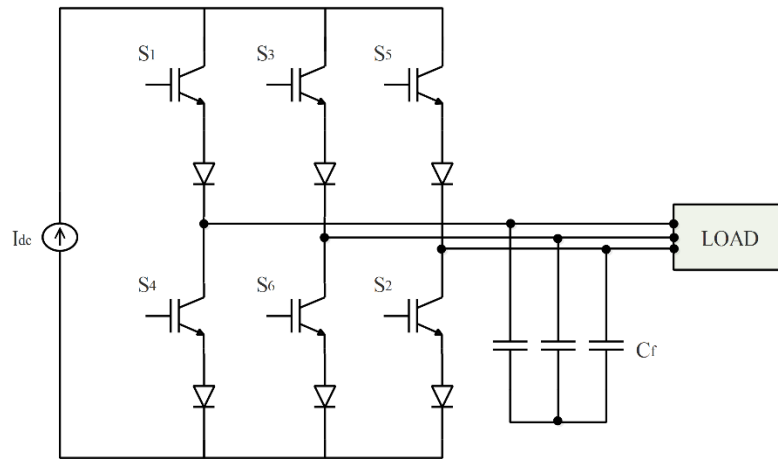
Figure 2.6 Ideal three phase CSI

2.3.2.4 Multi-level CSIs

To increase the power of a CSI, two or more CSIs can be connected in parallel to form a MCSI. Figure 2.7 shows such a configuration where two inverters are connected in parallel. Each inverter has its own DC current source, while they share the same capacitor filter at their outputs. The main issue of this topology is the number of inductors and the unbalance of DC currents. [2.8]
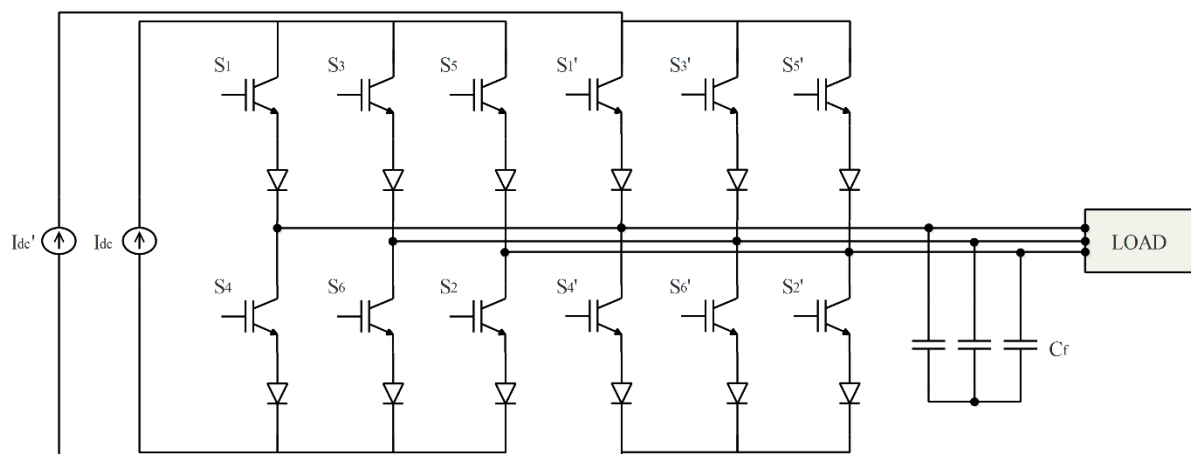
Figure 2.7 Parallel MCSI

2.4 Inverters control

The purpose of the inverter in a DG system is to convert the raw power generated into a form compatible with the local distribution grid, in order to allow the power to be used by standard appliances or to be fed back into the utility grid. Therefore, suitable inverter modulation techniques and control strategies are of high importance to satisfy all the control objectives of the DG system [2.6].

As reported previously, VSI represents the most widely used topology in industrial applications. Consequently, its modulation techniques are well-known, and have been reported widely in the literature. VSI modulation techniques include sinusoidal pulse width modulation (SPWM), third harmonic injected PWM (THIPWM), space vector modulation (SVM) and Selective harmonic elimination (SHE). In the other hand, several control strategies and methods have been investigated and developed by researchers for VSI, Figure 2.8 show the most common VSI control strategies. [2.6]-[2.10]
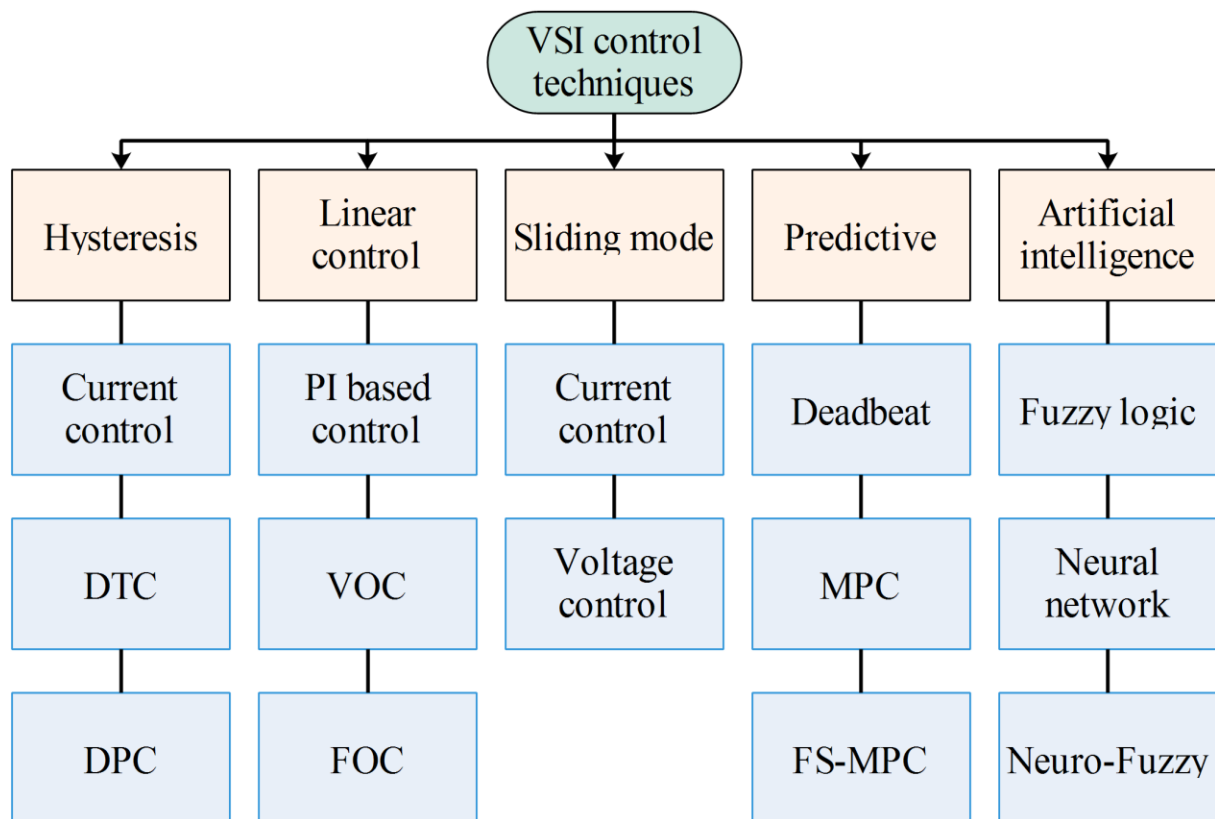
Figure 2.8 Most common VSI control strategies

In contrast, CSI modulation techniques are less-known compared to those of VSI. Moreover CSI control strategies are less developed and less investigated in the literature. Therefore, the following sections focus only on giving a detailed analysis of CSI modulation techniques and providing literature reviews of CSI control strategies for both stand-alone and grid-connected modes.

2.4.1 CSI modulation techniques

Various modulation techniques have been developed for the PWM CSI, including carrier-based sinusoidal PWM (CSPWM), Trapezoidal PWM space vector modulation (SVM), and selective harmonic elimination (SHE). Generally the switching pattern design for the CSI should generally satisfy two constraints: (1) The DC current should have a path at any time, (2) The output current of CSI should be defined. Thus, at any instant one and only one upper switch, and one and only one lower switch should be conducting. [2.8]-[2.10]

2.4.1.1 Carrier-based SPWM

A. SPWM VSI to CSI state map [2.12]

Carrier-based SPWM is simple to implement in a VSI and can be realized with a relatively low switching frequency. However, implementation of CSI carrier-based SPWM is not as straightforward as for the VSI case. The common approach used for the implementation of CSI carrier-based SPWM is to modify the gating signals of the VSI PWM using logic mapping circuitry.

Figure 2.9 depicts the principle of CSI switching signals generation using SPWM VSI to CSI state map modulation technique.
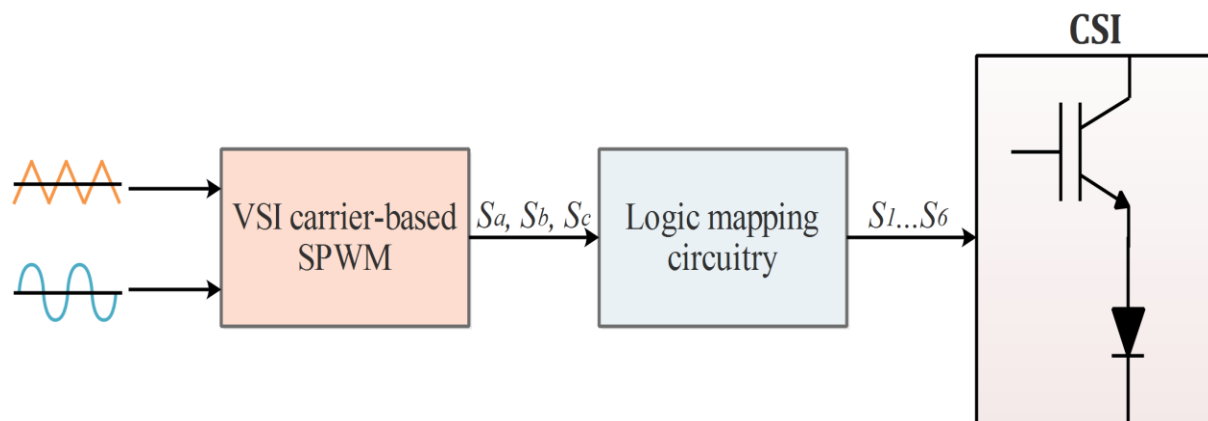
Figure 2.9 Diagram of SPWM VSI to CSI state map

B. Bi-logic/tri-logic PWM [2.13]

Bi-logic/tri-logic PWM is carried out using simple SPWM that generates X_a, X_b, X_c two-level signals (+1,-1) which are then transformed to tri-logic (-1,0,+1) PWM variables Y_a, Y_b, Y_c via a transformation matrix as follows

$$\begin{bmatrix} Y_a \\ Y_b \\ Y_c \end{bmatrix} = \frac{1}{2} \begin{bmatrix} 1 & -1 & 0 \\ 0 & 1 & -1 \\ -1 & 0 & 1 \end{bmatrix} \begin{bmatrix} X_a \\ X_b \\ X_c \end{bmatrix} \tag{1}$$

The resulting tri-logic PWM variables satisfy always the following equation

$$Y_a + Y_b + Y_c = 0 \tag{2}$$

Finally, the tri-logic signals are used by gating logic block to trigger the power switches of CSI, in such a way that the pth CSI output current I_{op} is given in terms of Y_p and DC current I_{dc} as

$$I_{op} = Y_p I_{dc} \tag{3}$$

However, it has to be pointed out that the tri-logic state ($Y_a=Y_b=Y_c=0$) can be realized by short-circuiting one of the CSI legs (freewheeling state)

According to the above analysis, it can noted that this modulation technique fulfills always the CSI switching constraints.

Table2.1 lists all possible bi-logic and tri-logic states with their corresponding switching signals

Table 2.1 CSI bi-logic/tri-logic states with corresponding switches triggering signals

Bi-logic signals			Tri-logic signals			Upper switches			Lower switches		
X_a	X_b	X_c	Y_a	Y_b	Y_c	S_1	S_3	S_5	S_2	S_4	S_6
+1	*+1*	*+1*	*0*	*0*	*0*	Freewheeling through one of CSI legs					
+1	*+1*	*-1*	*0*	*+1*	*-1*	*0*	*1*	*0*	*1*	*0*	*0*
+1	*-1*	*+1*	*+1*	*-1*	*0*	*1*	*0*	*0*	*0*	*0*	*1*
+1	*-1*	*-1*	*+1*	*0*	*-1*	*1*	*0*	*0*	*1*	*0*	*0*
-1	*+1*	*+1*	*-1*	*0*	*+1*	*0*	*0*	*1*	*0*	*1*	*0*
-1	*+1*	*-1*	*-1*	*+1*	*0*	*0*	*1*	*0*	*0*	*1*	*0*
-1	*-1*	*+1*	*0*	*-1*	*+1*	*0*	*0*	*1*	*0*	*0*	*1*
-1	*-1*	*-1*	*0*	*0*	*0*	Freewheeling through one of CSI legs					

Figure 2.10 shows the block diagram of bi-logic/tri-logic modulation technique.
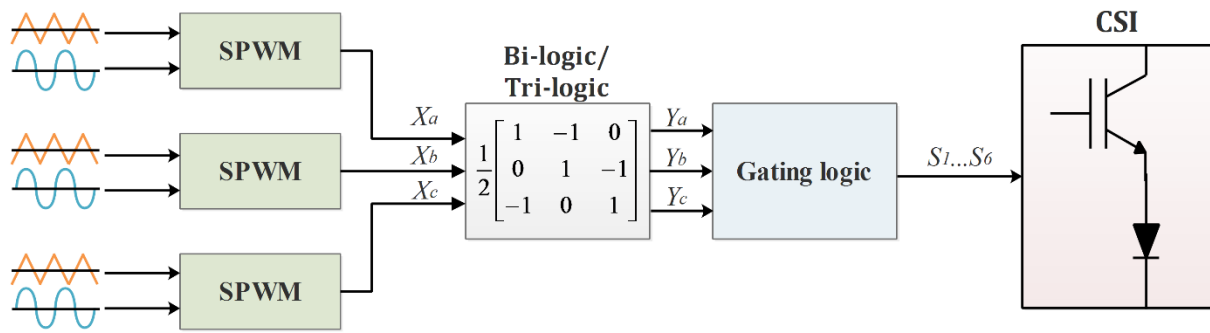
Figure 2.10 Diagram of bi-logic/tri-logic modulation technique

2.4.1.2 Trapezoidal PWM

The principle of TPWM is similar to PWM applied in VSIs, where the gate signals for one switch are generated by comparing the trapezoidal modulator with a defined triangular carrier. [2.8]. The gate signals of the rest of switches are derived by phase shifting by $\pi/3$ the gate signals of the previous switch as shown in Figure 2.8.
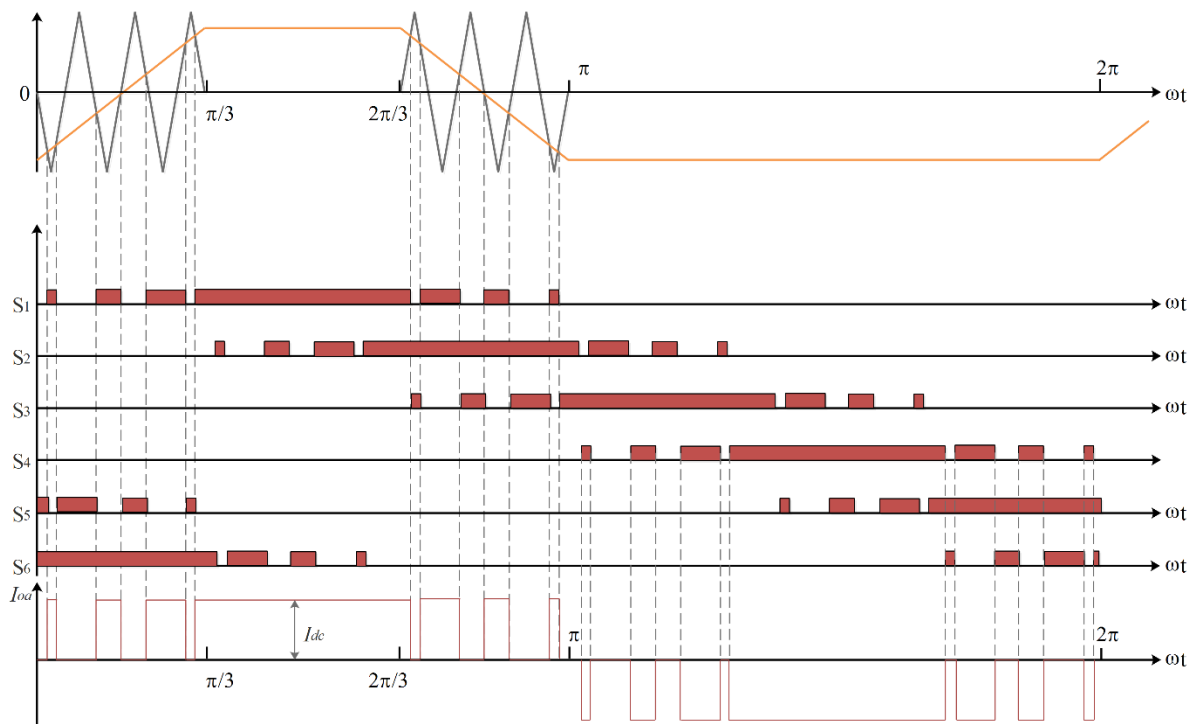
Figure 2.11 Trapezoidal PWM pattern

2.4.1.3 Space vector modulation (SVM)

Similar to VSIs, CSIs can also be controlled using SVM technique. To satisfy the aforementioned CSI switching constraints, the CSI can output nine current vectors in the stationary reference frame $\alpha\beta$, of which six are active vectors and three are null vectors. Table 2.1.

Table 2.2 CSI switching states and space vectors

		Switches					Current Vectors
	S_1	S_2	S_3	S_4	S_5	S_6	
Active States	1	1	0	0	0	0	$\vec{i_1} = 2I_{dc}e^{(j\pi/6)}/3^{1/2}$
	0	1	1	0	0	0	$\vec{i_2} = 2I_{dc}e^{(j\pi/2)}/3^{1/2}$
	0	0	1	1	0	0	$\vec{i_3} = 2I_{dc}e^{(j5\pi/6)}/3^{1/2}$
	0	0	0	1	1	0	$\vec{i_4} = 2I_{dc}e^{(j7\pi/6)}/3^{1/2}$
	0	0	0	0	1	1	$\vec{i_5} = 2I_{dc}e^{(j3\pi/2)}/3^{1/2}$
	1	0	0	0	0	1	$\vec{i_6} = 2I_{dc}e^{(j11\pi/6)}/3^{1/2}$
Zero states	1	0	0	1	0	0	$\vec{i_7} = 0$
	0	1	0	0	1	0	$\vec{i_8} = 0$
	0	0	1	0	0	1	$\vec{i_9} = 0$

A typical space vector diagram for the CSI is shown in Figure 2.9 (a), where $\vec{I_1}$ to $\vec{I_6}$ are active vectors, and $\vec{I_7}$ to $\vec{I_9}$ are zero vectors symbolized for simplification as $\vec{I_0}$. The active vectors form a regular hexagon with six equal sectors, whereas the zero vector lies in the center of the hexagon.

For a given length and position, $\overrightarrow{I_{ref}}$ can be synthesized by two adjacent vectors and one zero vector based on the ampere-second balance principle, that is, the product of the reference vector $\overrightarrow{I_{ref}}$ and the sampling period T_s equals the sum of the current vectors by the time interval of chosen space vectors [2.8]-[2.10]. Figure 2.9 (b). The ratio between the magnitudes of output current and the DC link current determines the modulation index m_a, and θ is defined as the phase displacement between the reference vector and α-axis of the stationary reference frame.

(a)   (b)
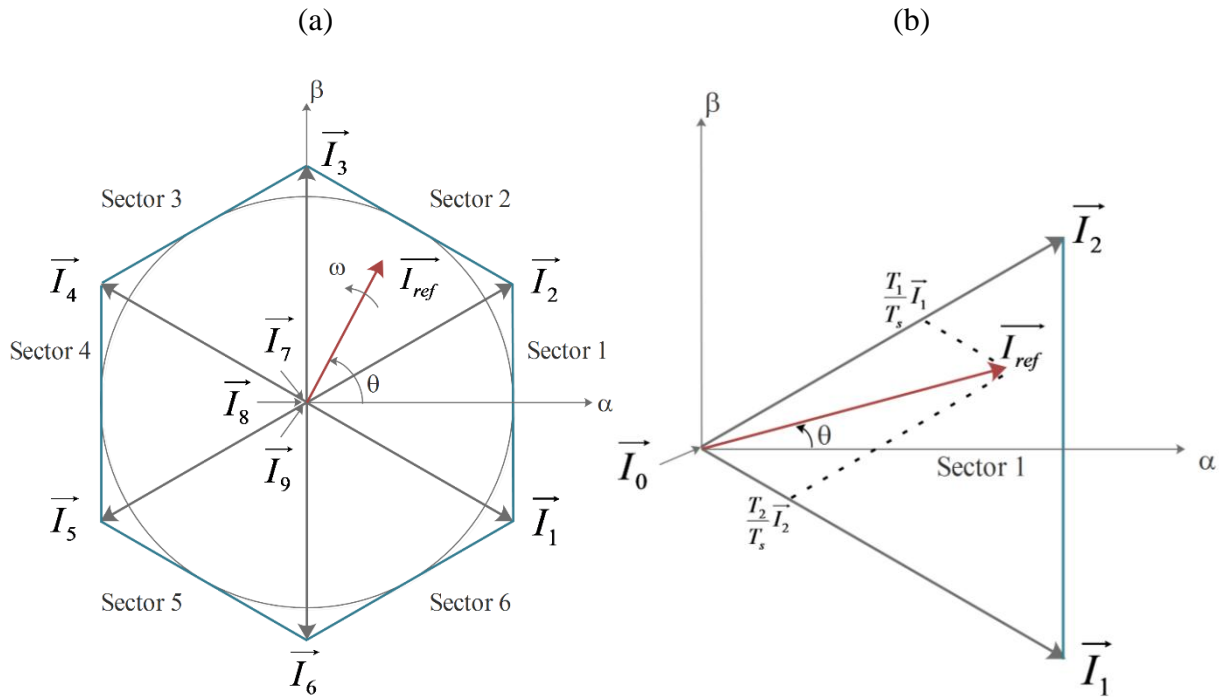
Figure 2.9 CSI SVM scheme: (a) space vector diagram (b) Synthesis of reference vector in sector 1

The ampere-second balancing equation is thus given by

$$\begin{cases} \overrightarrow{I_{ref}}T_s = \overrightarrow{I_1}T_1 + \overrightarrow{I_2}T_2 + \overrightarrow{I_0}T_0 \\ T_s = T_1 + T_2 + T_0 \end{cases}$$

(4)

The vector dwelling times can be derived by solving equations in (4)

$$\begin{cases} T_1 = m_a \sin(\pi/3 - \theta)T_s \\ T_2 = m_a \sin(\theta)T_s \\ T_0 = T_0 - T_1 - T_2 \end{cases}$$

(5)

Once the vector dwelling times are calculated, the vector sequence in a sampling period needs to be determined for the generation of PWM pulses. Different sequence patterns can be generated in function of zero vector used for each sampling time and its placement to achieve the desired switching frequency and harmonic profile.

2.4.1.4 Selective harmonic elimination

The SHE technique is an offline modulation scheme that can eliminate a number of unwanted low-order harmonics with a limited number of pulses. In this technique, the switching angles are pre-calculated and then imported into a digital controller for implementation [2.10]. In order to achieve a better harmonic profile and to reduce the complexity in finding switching pattern

solutions, the calculated pulses are normally arranged in such a way that the derived PWM waveform has a quarter-wave symmetrical shape. In high power applications, where the SHE is usually preferable, low switching frequency is needed to reduce the losses. Therefore, three, five or seven switching angles per quarter of cycle are preferred [2.9]. In the case shown in Figure 2.10, five pulses are employed. This figure shows a typical SHE pattern that satisfies the CSI switching constraint. There are five pulses per half cycle with five switching angles in the first $\pi/2$ period. However, only two out of the five angles, i.e., θ_1 and θ_2 are independent. Given these two angles, all other switching angles can be derived [2.8].

The two switching angles provide the ability to eliminate two harmonics such as the 5th and 7th harmonic from the inverter output current. This can be considered as the main advantage of this technique, since this is hardly possible by using other modulation techniques to remove these low order harmonics. Nevertheless, the main disadvantage of this technique is the lack of flexibility for control as the offline calculated set of angles is valid at only a certain modulation index. Moreover, the calculation of SHE angles with a large number of pulses per fundamental cycle sometimes involves transcendental equations that have no solutions, which prevents the SHE from being applied to a full frequency range.[2.10]
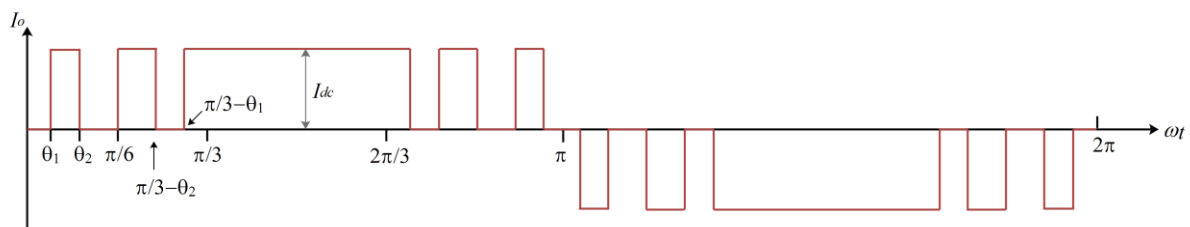
Figure 2.10 Selective harmonic elimination (SHE) PWM pattern

Table 2.2 Comparison of most common CSI modulation techniques [2.8]

Item	TPWM	SVM	SHE
Modulation index	0.74	0.707	0.73-0.78
Dynamic performance	Medium	High	Low
Digital implementation	Real time/ Look-up table	Real time	Look-up table
Harmonic performance	Good	Adequate	Best
DC current freewheeling	No	Yes	Optional

The table above presents a comparison between the three most common modulation techniques which are TPWM, SVM, and SHE. It is obvious that SVM is the more adequate technique due the features it offers, especially the fast dynamic. However SHE is the best choice in terms of harmonics elimination. But, it has to be pointed out that TPWM is simplest technique for digital implementation.

2.5 Literature review of CSI based stand-alone systems

There exist numerous researches on stand-alone CSIs feeding linear and non-linear loads. Some of them address voltage regulation, whereas the rest consider current control only. Among the proposed current control strategies reported in the literature: In [2.14] SVM is utilized and analyzed in details, whilst in [2.15] a modified SVM named direct regular sampled SVM is proposed. It is based on the modification of the switching sequences of conventional SVM, in order to reduce the switching frequency. Authors in [2.16] proposed a predictive current control strategy and addressed the issue of reducing switching frequency also. A 7 switches (CSI7) topology with a new modulation technique have been proposed in [2.17]. The purpose was to achieve lower switching frequency and reduce the size of the inductor and attain high performances. In [2.18] it has been proposed a four leg CSI to overcome the problem of common-mode voltage.

Though these control technique offer a suitable current control, voltage control is required for standalone systems, since the majority of loads need a defined voltage for their operation. The available researches on voltage control for stand-alone CSIs [2.19]-[2.24] are achieved through current control by employing controllers and voltage regulation loops that are designed and tuned for a predefined load types and values. Hence, their stability and accuracy are not guaranteed for change in load. This problem has been overcome in this thesis.

2.6 Literature review of CSI based grid connected systems

A fair amount of researches have been carried out for grid connected CSI systems. The available researches focused in general on the following points:

- **Modified CSI topologies:** In [2.25] a PV grid connected CSI is introduced using a double-tuned parallel resonant circuit to attenuate the second- and fourth-order harmonics at the inverter DC side, and proportional-resonant (PR) current controller along with a modified carrier based modulation technique. In [2.26], a multi-level structure based on CSI topology is presented. Each inverter unit in the multi-level

structure is fed with a PV source and equipped with its own MPPT and DC-side current controller. On the AC-side, a combined *dq*-frame current controller is adopted using SHE. The same topology is investigated in [2.27] but by considering equal and unequal DC link currents. [2.28] presented a transformer-less grid connected PV systems using a four-leg CSI topology in order to overcome the problem of earth leakage current. To achieve high voltage gain and a steady AC output voltage in spite of the low DC input voltage, the article of [2.29] presents a novel single-stage high gain CSI. The topology of the proposed inverter is derived from conventional tri-state CSI by introducing an impedance network with two symmetrical inductors and diodes separately. [2.30] proposes a single-stage bidirectional CSI topology to deal with the issue of unbalanced grid voltages and the resulting oscillations on the DC link current. [2.31] analyzes the performance of a grid-tied, transformer-less, modified three phase CSI, named CSI7. The proposed CSI7 topology is made by installing an additional switch in parallel with the DC source for the purpose of elimination glitches during transitions between vectors of SVM.

- **Modified modulation techniques**: [2.32] proposed a current control technique in *dq*-frame using PI regulator to control the DC link current with a modified SVM as a modulator. The goal of the modified SVM is to attenuate the common-mode currents. In [2.33], a switching pattern based on the concept of the conventional space vector PWM technique is developed for single-stage, three-phase boost-inverters using the CSI topology. [2.34] proposed a novel switching algorithm applied to CSI topology to control the charging time and discharging interval of converters inductor. A new direct regular sampled PWM derived from SVM has been proposed in [2.35]. The proposed technique is achieved by changing the dwell times of the standard SVM and the placement of the zero vectors in order to reduce the switching frequency. The same issue has been investigated in [2.36] where a modified synchronous optimal PWM technique for CSI is proposed.

- **Control strategies:** In [2.37] a PV grid connected CSI control is performed in the *dq*-frame using SHE. Authors in [2.38] investigated the AC- and DC-instabilities and proposed an active compensator in order to robustly damp the *CL* filter dynamics. [2.39] presents a control structure for a CSI-based DG system, based on a multi-synchronous reference frame (MSRF) architecture that rejects the effect of utility voltage distortion and helps attain high-quality output current. Predictive control has been investigated only two times for grid connected CSI in the literature. In [2.40] a finite-set predictive

current control is proposed where an active resonance damping is done using a virtual resistor in the controller. Whereas in [2.41] authors have proposed an indirect predictive power control via the control of the grid currents in the *dq*-frame using a two-step prediction horizon. [2.42] proposed an indirect power control technique in the *dq*-frame through the use of hysteresis current controllers along with a look-up table. [2.43] proposed a power synchronization control for CSI-based PV generator in order to overcome the drawbacks of vector control techniques applied for CSI. This technique eliminates the PLL through the use PI based power control loop in order to regulate the grid active power and generate the synchronization angle. In [2.44] a non-linear adaptive backstepping controller is proposed, where the control structure is composed with an outer control loop responsible for controlling the DC-side inductor current and the inner current control loop responsible for controlling injected current into the utility grid. Authors in [2.45] have proposed a modified single phase CSI in order to reduce the leakage current, and a multi-loop control strategy is proposed with an incorporated virtual resistor active damping.

2.7 Conclusion

In this chapter, a brief analysis and description of DG systems has been achieved, and it has been reported that conventional power grids present many drawbacks. Therefore, DGs should have more interest in the coming years. PV generators operation principle and their grid interfacing configuration were investigated, where it has been clarified that single-stage can fulfill all the objectives with better efficiency. A classification and description of the most common inverter topologies are reported in the third section of this chapter. The existing modulation techniques for CSI have been explained and analyzed as well, and comparison between them is carried out. Finally a literature review on stand-alone and grid-connected CSI based systems is performed to evaluate the state of the art of available control strategies.

References

[2.1]   Y. Cecati, C. Dillon, T. Simões, "The new frontier of smart grids.," *IEEE industrial electronics magazine*, Vol. 5, No. 3, Jul. 2011, pp. 49–63

[2.2]   H. Abu-Rub. M. Malinowski, K. Al-Haddad, *Power Electronics for Renewable Energy Systems, Transportation, and Industrial Applications*. John Wiley & Sons, Ltd, 2015.

[2.3]   F. Blaabjerg, D. M. Ionel, "Renewable Energy Devices and Systems – State-of-the-Art Technology, Research and Development, Challenges and Future Trends," *Electric Power Components and Systems*, Vol. 43, No. 12, Jul. 2015, pp. 1319–1323

[2.4]   A. Anzalchi, A. Sarwat, "Overview of Technical Specifications for Grid-Connected Photovoltaic Systems," *Energy Conversion and Management*, Vol. 152, No. 15, Nov. 2017, pp. 312–327

[2.5]   O. P. Mahela, A. G. Shaik, "Comprehensive Overview of Grid Interfaced Solar Photovoltaic Systems," *Renewable and Sustainable Energy Reviews*, Vol. 68, No. 1, Dec. 2017, pp. 316–332

[2.6]   F. L. Lyo, H. Ye, *Advanced DC/AC Inverters Application in Renewable Energy*. CRC Press, 2013.

[2.7]   R. Teodorescu. M. Liserre, P. Rodriguez, *Grid Converters for Photovoltaic and Wind Power Systems*. John Wiley & Sons, Ltd, 2011.

[2.8]   B. Wu, *High-power Converters and AC drives*, John Wiley & Sons, Ltd, 2006.

[2.9]   B. K. Bose, *Modern Power Electronics and AC drives*, Prentice Hall PTR, 2002.

[2.10] M. H. Rashid, *Power Electronics Handbook, Third Edition*, Butterworth-Heinemann, Ltd, 2011.

[2.11] B. Sahan, S. V. Araujo, C. Noding, P. Zacharias, "Comparative Evaluation of Three-Phase Current Source Inverters for Grid Interfacing of Distributed and Renewable Energy Systems," *IEEE Trans. on Power Electronics*, Vol. 26, No. 8, Aug. 2011, pp. 2304–2318

[2.12] J. R. Espinoza, G. Joos, "Current-source converter on-line pattern generator switching frequency minimization," *IEEE Trans. on Industrial Electronics*, Vol. 44, No. 2, Apr. 1997, pp. 198-206

[2.13]   X. Wang, B. T. Ooi, "Unity PF Current-Source Rectifier Based on Dynamic Trilogic PWM," *IEEE Trans. on Power Electronics*, Vol. 8, No. 3, Jul. 1993, pp. 288-294

[2.14]   D. C. Pham, S. Huang, K. Huang, "Modeling and Simulation of Current Source Inverters with Space Vector Modulation," *in Proc. Int. Conf. on Electrical Machines and Systems*, South Korea, 2010.

[2.15]   S. A. Azmi, G. P. Adam, B. W. Williams, "New Modulation Strategy for Three-Phase Current Source Inverters," *in Proc. 4th Int. Conf. on Power Engineering, Energy and Electrical Drives*, Turkey, 2013.

[2.16]   M. Rivera, S. Kouro, J. Rodriguez, B. Wu, V. Yaramasu, J. Espinoza, P. Melin, "Predictive Current Control in a Current Source Inverter Operating with Low Switching Frequency," *in Proc. 4th Int. Conf. on Power Engineering, Energy and Electrical Drives*, Turkey, 2013.

[2.17]   W. Wang, F. Gao, S. Rui, "Operation and Modulation of H7 Current Source Inverter with Hybrid SiC and Si Semiconductor Switches," *in Proc. 9th Int. Conf. on Power Electronics*, Korea, 2015.

[2.18]   X. Guo, D. Xu, B. Wu, "Four-Leg Current Source Inverter with a New Space Vector Modulation for Common-Mode Voltage Suppression," *IEEE Trans. on Industrial Electronics*, Vol. 62, No. 10, Oct. 2015, pp. 6003–6007.

[2.19]   V. D. Colli, P. Cancelliere, F. Marignetti, R. Di Stefano, "Voltage Control of Current Source Inverters," *IEEE Trans. on Energy Conversion*, Vol. 21, No. 2, Jun. 2006, pp. 451–458

[2.20]   H. Kömürcügil, O. Kükrer, "Control Strategy for Three-Phase Current-Source Inverters Based on Lyapunov's Direct Method," *in Proc. IEEE Symposium on Industrial Electronics*, UK, 2008.

[2.21]   L. Tan, Y. Li, C. Liu, P. Wang, Z. Li, "Advanced Voltage Control Methods for Current Source Inverters with Linear and Nonlinear Loads," *in Proc. IEEE Symposium on Industrial Electronics*, Korea, 2009.

[2.22]   S. A. S. Grogan, D. G. Holmes, B. P. McGrath, "High Performance Voltage Regulation of Current Source Inverters," *IEEE Trans. on Power Electronics*, Vol. 26, No. 9, Sep. 2011, pp. 2439–2448

[2.23]   L. S. Garcia, L. C. de Freitas, G. M. Buiatti, E. A. A. Coelho, V. J. Farias, L. C. G. Freitas, "Evaluation of a Single-stage Current Source Inverter with High-

voltage Gain Supplied by a Polymer Electrolyte Membrane Fuel cell," *IET Power Electronics*, Vol. 5, No. 9, Nov. 2012, pp. 1834–1846

[2.24]   A. Singh, A. K. Kaviani, B. Mirafzal, "On Dynamic Models and Stability Analysis of Three-Phase Phasor PWM-Based CSI for Stand-Alone Applications," *IEEE Trans. on Industrial Electronics*, Vol. 62, No. 5, May, 2015, pp. 2698 –2707

[2.25]   B. N. Elajmi, K. H. Ahmed, G. P. Adam, B. W. Williams , "Single-Phase Single-Stage Transformer-less Grid-Connected PV System," *IEEE Trans. on Power Electronics*, Vol. 28, No. 6, Jun. 2013, pp. 2664–2676

[2.26]   P. P. Dash, M. Kazerani, "A multilevel current-source inverter based grid-connected photovoltaic system," *in Proc. North American Power Symposium*, USA, 2011.

[2.27]   A. Chakravarthula, T. C. Reddy, B. G. Fernandes, "Multilevel Operation of a PV Fed Grid Connected Current Fed Inverter Under Equal and Unequal DC Link Currents," *in Proc. IEEE inter. Industry Technology*, Spain, 2015.

[2.28]   S. Anand, S. K. Gundlapalli, B. G. Fernandes, "Transformer-Less Grid Feeding Current Source Inverter for Solar Photovoltaic System," *IEEE Trans. on Industrial Electronics*, Vol. 61, No. 10, Oct. 2014, pp. 5334–5344

[2.29]   M. Mao, Y. Zheng, L. Chang, H. Xu, "A Single-Stage High Gain Current Source Inverter for Grid-Connected Photovoltaic System," *in Proc. inter. Conf. Power Electronics*, Korea, 2015.

[2.30]   V. Vekhande, V. K. Kanakesh, B. G. Fernandes, "Control of Three-phase Bidirectional Current Source Converter to Inject Balanced Three-phase Currents under Unbalanced Grid Voltage Condition," *IEEE Trans. on Power Electronics*, Vol. 31, No. 9, Sep. 2016, pp. 6719– 6737

[2.31]   E. Lorenzani, F. Immovilli, G. Migliazza, M. Frigieri, C. Bianchini, M. Davoli, "CSI7: A Modified Three-Phase Current-Source Inverter for Modular Photovoltaic Applications," *IEEE Trans. on Industrial Electronics*, Vol. 64, No. 7, Jul. 2017, pp. 5449–5459

[2.32]   B. Sahan, A. N. Vergara, N. Henze, A. Engler, P. Zacharias, "A Single-Stage PV Module Integrated Converter Based on a Low-Power Current-Source Inverter," *IEEE Trans. on Industrial Electronics*, Vol. 55, No. 7, Jul. 2008, pp. 2602–2609

[2.33]   B. Mirafazal, M. Saghaleini, A. K. Kaviani, "An SVPWM-Based Switching Pattern for Stand-Alone and Grid-Connected Three-Phase Single-Stage Boost Inverters," *IEEE Trans. on Power Electronics*, Vol. 26, No. 4, Apr. 2011, pp. 1102–1111

[2.34]   A. Ebrahimi, H. S. Fathi, H. Gholamrezaei, "Novel Switching Pattern for Single-stage Current Source Inverter for Grid-connected Photovoltaics," *IET Power Electronics*, Vol. 7, No. 10, Oct. 2014, pp. 2447–2454

[2.35]   S. A. Azmi, G. P. Adam, B. Williams, "New Direct Regular-Sampled Pulse-Width Modulation Applicable for Grid and Islanding Operation of Current Source Inverters," *IET Power Electronics*, Vol. 7, No. 1, Jan. 2014, pp. 220–236

[2.36]   B. Sahan, A. N. Vergara, N. Henze, A. Engler, P. Zacharias, "Optimal Low Switching Frequency Pulse width Modulation of Current-Fed Three-Level Converter for Solar Power Integration," *IEEE Trans. on Industrial Electronics*, Vol. 63, No. 11, Nov. 2016, pp. 6877–6886

[2.37]   P. P. Dash, M. Kazerani, "Dynamic Modeling and Performance Analysis of a Grid-Connected Current-Source Inverter-Based Photovoltaic System," *IEEE Trans. on Sustainable Energy*, Vol. 2, No. 4, Oct. 2011, pp. 443–450

[2.38]   A. Radwan, Y. Mohamed, "Analysis and Active Suppression of AC- and DC-Side Instabilities in Grid-Connected Current-Source Converter-Based Photovoltaic System," *IEEE Trans. on Sustainable Energy*, Vol. 4, No. 3, Jul. 2013, pp. 630–642

[2.39]   A. Morsy, S. Ahmed, A. M. Massoud, "Harmonic Rejection in Current Source Inverter-based Distributed Generation with Grid Voltage Distortion Using Multi-synchronous Reference Frame," *IET Power Electronics*, Vol. 7, No. 6, Jun. 2014, pp. 1323–1330

[2.40]   C. Du, J. Zhou, Y. Ma, "Predictive Current Control of a Current-Source Inverter with Active Damping Method," *in Proc. IEEE Conf. Energy Conversion*, Canada, 2015.

[2.41]   A. Moghadasi, A. Sargolzaei, A. Khalilnejad, M. Moghaddami, A. Sarwat, "Model Predictive Power Control Approach for Three-Phase Single-Stage Grid-Tied PV Module-Integrated Converter," *in Proc. IEEE Ann. Meeting Industry Applications*, USA, 2016.

[2.42]   T. Geury, S. Pinto, J. Gyselinck, "Current Source Inverter-based Photovoltaic System With Enhanced Active Filtering Functionalities," *IET Power Electronics*, Vol. 8, No. 12, Dec. 2015, pp. 2483–2491.

[2.43]   A. Radwan, Y. Mohamed, "Power Synchronization Control for Grid-Connected Current-Source Inverter-Based Photovoltaic Systems," *IEEE Trans. on Energy Conversion*, Vol. 31, No. 3, Sep. 2016, pp. 1023–1036

[2.44]   T. K. Roy, L. C. Paul, M. I. Sarkar, M. F. Pervej, F. K. Tumpa, "Nonlinear Adaptive Backstepping Controller Design for Grid Currents Regulation of a CSI Based PV System with External Disturbances," *in Proc. Int. Conf. Elec. Comp. Comm. Engineering*, Bangladesh, 2017.

[2.45]   M. Rajeev, V. Agarwal, "Single Phase Current Source Inverter with Multi Loop Control for Transformer-less Grid -PV Interface," *IEEE Trans. on Industry Applications*, Vol. xx, No. x, Jan. 2018, pp. xx–xx **(early access)**

Chapter 3

Design and modeling of systems components

3.1 Introduction

This chapter presents the design and modeling for stand-alone and PV grid-connected CSI system components. Starting by the PV source, where the single diode equivalent circuit is adopted. First, the model of an ideal PV cell is derived, then, in order to get a practical model the non-idealities represented by the series and parallel resistances are introduced into the ideal model. However, a PV array is composed of multiple series and parallel connected cells, therefore, the number of series and parallel connected cells is included, and the PV array model is deduced. The effects of solar irradiance and ambient temperature on the PV array characteristics have been exhibited also. The chapter also provides the operation principle, and model of CSI. The possible states and output vectors are presented as well by taking into account the CSI switching constraints. In the last part of the chapter, the filter model and design for stand-alone and grid-connected CSI are studied. For stand-alone CSI only a capacitor filter is required for the attenuation of high-frequency harmonics generated by the PWM. Nevertheless, in grid-connected CSI an inductor is introduced with the capacitor to form a *CL* filter. The inductor is required to increase the attenuation capabilities, which results in better quality of the injected currents. The filter model is derived in the natural frame *abc*, the stationary reference frame *αβ*, and in the SRF *dq*. However, the presence of *CL* filter could generate possible resonance if the frequency of one of the generated harmonics meets the resonance frequency. Therefore, damping is necessary to reduce the resonance behavior. Passive damping is the most popular method, where a resistor is connected in series or in parallel with the filter inductor or capacitor. The different configurations of the damping resistors are studied and analyzed in details this chapter.

3.2 PV model

PV system directly converts sunlight into electricity. The basic device of a PV system is the PV cell. Cells may be grouped to form panels or arrays [3.1]. The voltage and current available at

the terminals of a PV device may directly feed small loads such as lighting systems and DC motors [3.2]. More sophisticated applications require electronic converters to process the electricity from the PV device. These converters may be used to regulate the voltage and current at the load, to control the power flow in grid-connected systems, and mainly to track the maximum power point (MPP) of the device. [3.2],[3.3]

The basic building block of the PV generator is the PV cell, which is basically a semiconductor diode whose p–n junction is exposed to light. It typically produces 1 to 2 W of electrical power [3.2]. The equivalent circuit of a photovoltaic cell is shown in Figure 3.1, where the simplest ideal model can be represented by a current source in parallel with a diode. [3.1]-[3.7]
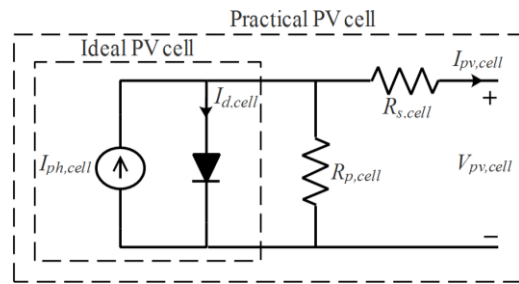
Figure 3.1 Single diode model of theoretical and practical equivalent circuit of a PV cell

The output current of an ideal PV cell can be written as [3.1]-[3.7]

$$I_{pv,cell} = I_{ph,cell} - I_{o,cell}\left[\exp\left(\frac{V_{pv,cell}}{aV_{t,cell}}\right) - 1\right] \tag{2}$$

Where, $V_{pv,cell}$ is the PV cell output voltage, and $I_{ph,cell}$, $I_{o,cell}$, $V_{t,cell}$ are the cell photovoltaic current, diode saturation current, and temperature voltage, respectively, given by [3.1]-[3.7]

$$I_{ph,cell} = \left[I_{sc,cell\_n} + K_I(T - T_n)\right]\frac{G}{G_n} \tag{3}$$

$$I_{o,cell} = I_{o,cell\_n}\left(\frac{T_n}{T}\right)^3 \exp\left[\frac{qE_g}{ak}\left(\frac{1}{T_n} - \frac{1}{T}\right)\right] \tag{4}$$

$$V_{t,cell} = \frac{kT}{q} \tag{5}$$

Where G, G_n are the operational and nominal irradiations in W/m^2, respectively; T, T_n are the operational and nominal temperatures in $^\circ$K, respectively; K_I is temperature coefficient in A/$^\circ$K, $I_{o,cell\_n}$ is the nominal saturation current; E_g is the band gap of energy of the semiconductor; a is the ideality factor of the diode; q is the unit charge; and k is the Boltzmann's constant.

In practical PV cell equivalent electrical circuit the presence of the series and parallel resistances is considered -Figure 3.1- [3.1]-[3.7], hence, the practical PV cell output current is

$$I_{pv,cell} = I_{ph,cell} - I_{0,cell}\left[\exp\left(\frac{V_{pv,cell} + R_{s,cell}I_{pv,cell}}{V_{t,cell}a}\right) - 1\right] - \frac{V_{pv,cell} + R_{s,cell}I_{pv,cell}}{R_{p,cell}} \qquad (6)$$

The basic equation (6) of the elementary PV cell does not represent the characteristic of a practical PV array. Practical arrays are composed of several series (N_s) and parallel (N_p) connected PV cells, and the observation of the characteristics at the terminals of the PV requires the inclusion of these two parameters as $I_{ph}=N_p.I_{ph,cell}$, $I_o=N_p.I_{o,cell}$, $V_{pv}=N_p.V_{pv,cell}$, $V_t=N_p.V_{t,cell}$, $R_p=N_p.R_{p,cell}$, $R_s=N_s.R_{s,cell}$. [3.1]-[3.7]

Which yields to the practical PV array output current equation

$$I_{pv} = I_{ph} - I_0\left[\exp\left(\frac{V_{pv} + R_sI_{pv}}{V_ta}\right) - 1\right] - \frac{V_{pv} + R_sI_{pv}}{R_p} \qquad (7)$$

The effects of temperature and sun irradiance on the (I-V) and (P-V) characteristics of PV array (whose parameters are given in Appendix-A) are depicted in the following figures, where $P_{pv}=V_{pv}.I_{pv}$ is the PV array output power
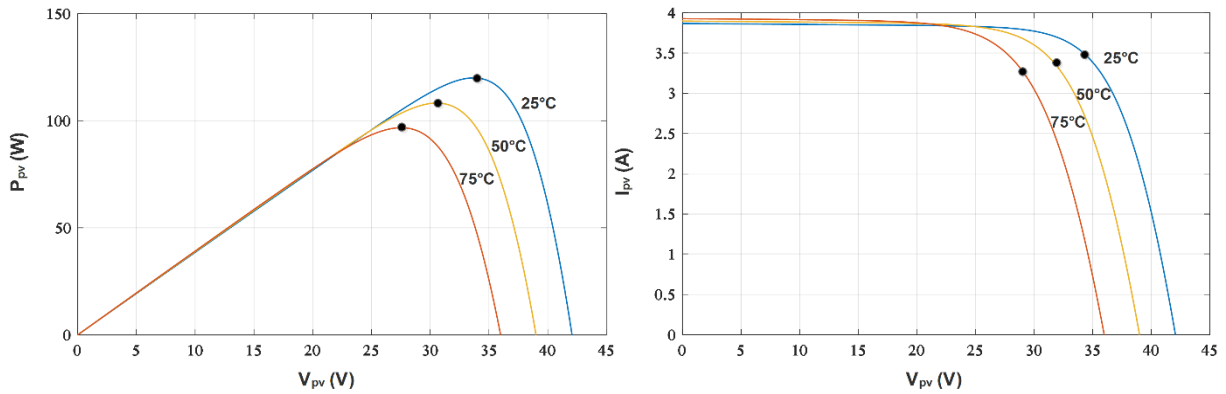

Figure 3.2 Effect temperature on PV characteristics
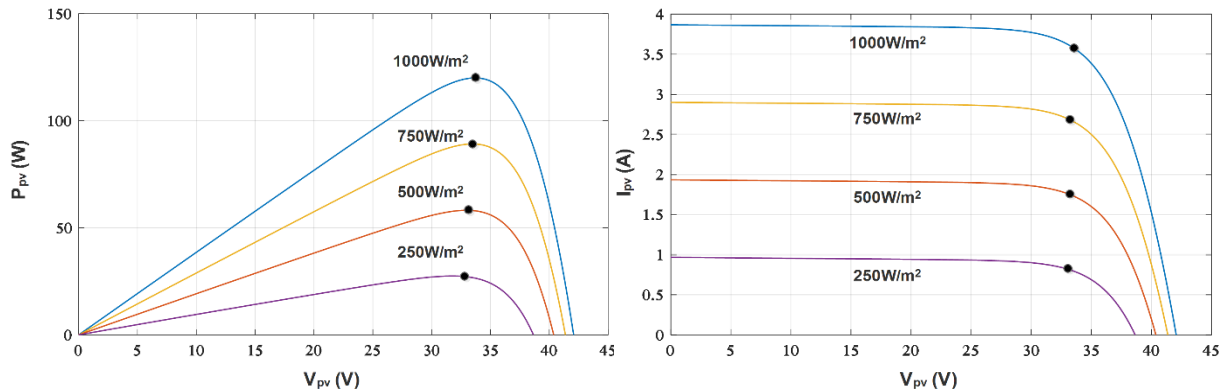
Figure 3.3 Effect of irradiance on PV characteristics

3.3 CSI model

The PWM CSI shown in Figure 3.4 is a six-pulse inverter employing six unidirectional switches (IGBT in series with a diode, or a RB-IGBT). The DC side is composed of a current source (I_{dc}), which is practically built using a voltage source in series with a DC choke (L_{dc}) to maintain and smooth the DC link current. An AC capacitor filter (C_f) is directly connected at the CSI terminals in order to significantly reduce the high frequency harmonics of the output current (I_o) generated by the switching actions of the inverter [3.7]-[3.12].

Two constraints for CSI switching must be always met. The DC link of CSI acts as a current source and cannot be open-circuited. Thus, at least one top switch and one bottom switch must be ON at any instant of time. On the other hand, in order to produce defined three-phase current waveforms at the AC side, at most one top switch and one bottom switch must be conducting at any given instant of time. In other words, one and only one top switch and one and only one bottom switch must be ON at any instant of time [3.8]-[3.11].
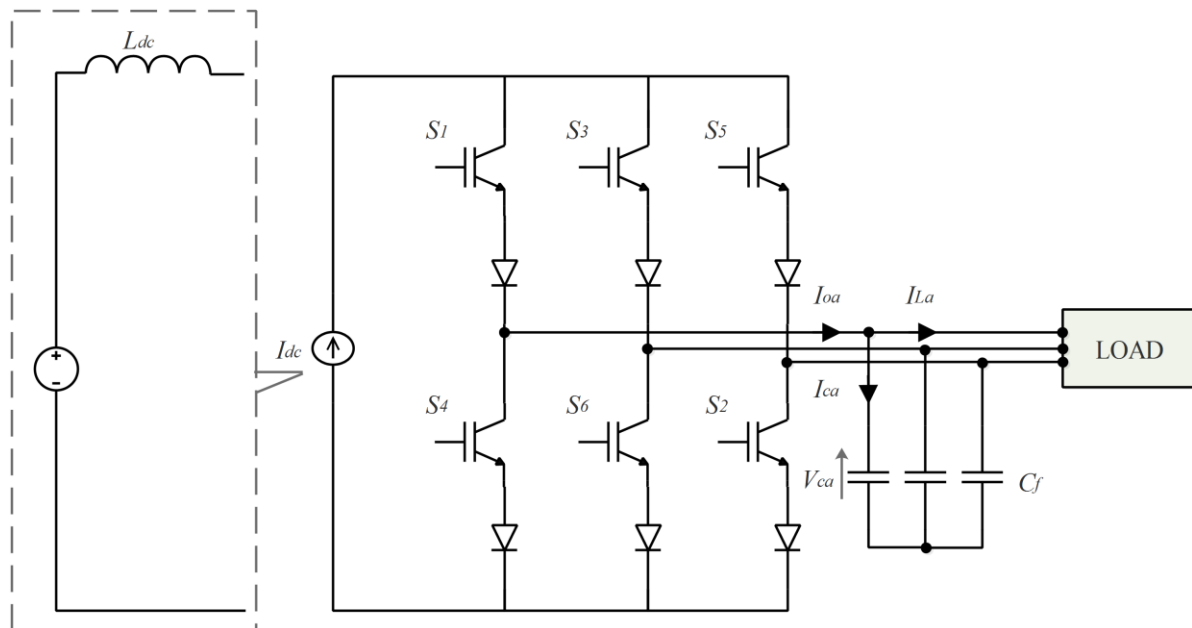
Figure 3.4 Three phase CSI

These restrictions can be summarized as follows

$$S_1 + S_3 + S_5 = S_2 + S_4 + S_6 = 1 \tag{6}$$

The output currents can be defined according to the switching signals and the DC current I_{dc} by

$$I_{oa} = (S_1 - S_4)I_{dc} \tag{7}$$

$$I_{ob} = (S_3 - S_6)I_{dc} \tag{8}$$

$$I_{oc} = (S_5 - S_2)I_{dc} \tag{9}$$

Using the coordinate transformation from the natural frame to the stationary reference frame $\alpha\beta$, the output current vector $\vec{I_o}$ can written as follows

$$\vec{I_o} = I_{o\alpha} + jI_{o\beta} = I_m e^{j\theta} \tag{11}$$

Where I_m, and θ are the magnitude and angle of the output current vector.

Based on the aforementioned constraints, the valid switching states with the corresponding output currents and output current vectors are presented in table.3.1. There are nine valid switching states in the operation of CSI, states 1 to 6 are active states, where current flows from DC-side to the load. On the other hand, states 7 to 9 are zero states, where the DC link current is short-circuited by one of the CSI legs. Thus, no power transfer from DC-side to load during these states. They are also known as shoot-through or freewheeling states.

Table. 3.1 CSI possible states and corresponding output currents and vectors

	Switches						output currents			Current Vectors
	S1	S2	S3	S4	S5	S6	I_{oa}	I_{ob}	I_{oc}	
Active States	1	1	0	0	0	0	I_{dc}	0	$-I_{dc}$	$\vec{i_1} = 2I_{dc}e^{(j\pi/6)}/3^{1/2}$
	0	1	1	0	0	0	0	I_{dc}	$-I_{dc}$	$\vec{i_2} = 2I_{dc}e^{(j\pi/2)}/3^{1/2}$
	0	0	1	1	0	0	$-I_{dc}$	I_{dc}	0	$\vec{i_3} = 2I_{dc}e^{(j5\pi/6)}/3^{1/2}$
	0	0	0	1	1	0	$-I_{dc}$	0	I_{dc}	$\vec{i_4} = 2I_{dc}e^{(j7\pi/6)}/3^{1/2}$
	0	0	0	0	1	1	0	$-I_{dc}$	I_{dc}	$\vec{i_5} = 2I_{dc}e^{(j3\pi/2)}/3^{1/2}$
	1	0	0	0	0	1	I_{dc}	$-I_{dc}$	0	$\vec{i_6} = 2I_{dc}e^{(j11\pi/6)}/3^{1/2}$
Zero states	1	0	0	1	0	0	0	0	0	$\vec{i_7} = 0$
	0	1	0	0	1	0	0	0	0	$\vec{i_8} = 0$
	0	0	1	0	0	1	0	0	0	$\vec{i_9} = 0$

The nine possible output current vectors of CSI are shown in figure 3.5
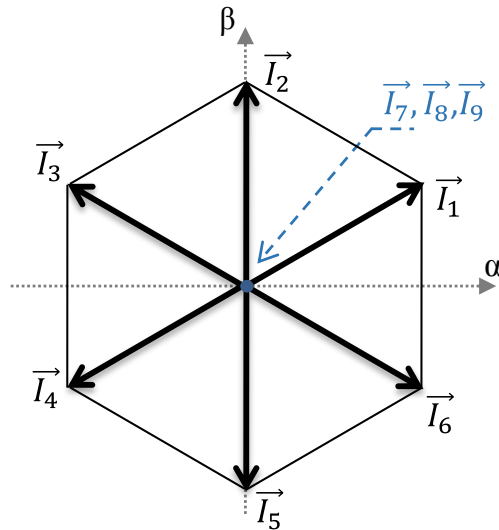
Figure 3.5 CSI output current vectors

3.4 filter modeling and design

3.4.1 Stand-alone CSI

As reported previously, a CSI requires a capacitor filter to assist the current commutations among the phases and to absorb the high frequency harmonics associated with the PWM CSI output currents. For stand-alone voltage controlled CSI, the capacitor value is chosen in order to have good quality voltages with low harmonic distortion, since undesirable harmonics may disturb other sensitive loads/equipment and may also result in extra power losses [3.13]. Moreover, the problem of resonance may not occur because the majority of loads contain resistors, so the resonance is inherently damped.

In the other hand, the stand-alone CSI can be modeled by the equation that governs the interaction between CSI output current, capacitor voltage and load current given by

$$I_{L(\alpha,\beta)} = I_{o(\alpha,\beta)} - C\frac{dV_{c(\alpha,\beta)}}{dt} \tag{12}$$

3.4.2 Grid-connected CSI

Though for stand-alone CSI a capacitor filter is sufficient, for grid-connected CSI a coupling inductor (L_f) with internal resistance (R_f) is connected between the capacitor filter and the grid. This results in a *CL* filter that provides higher attenuation capabilities [3.14], hence, reaching best quality of the injected current. Figure 3.6 shows a typical grid-connected CSI using *CL* filter.
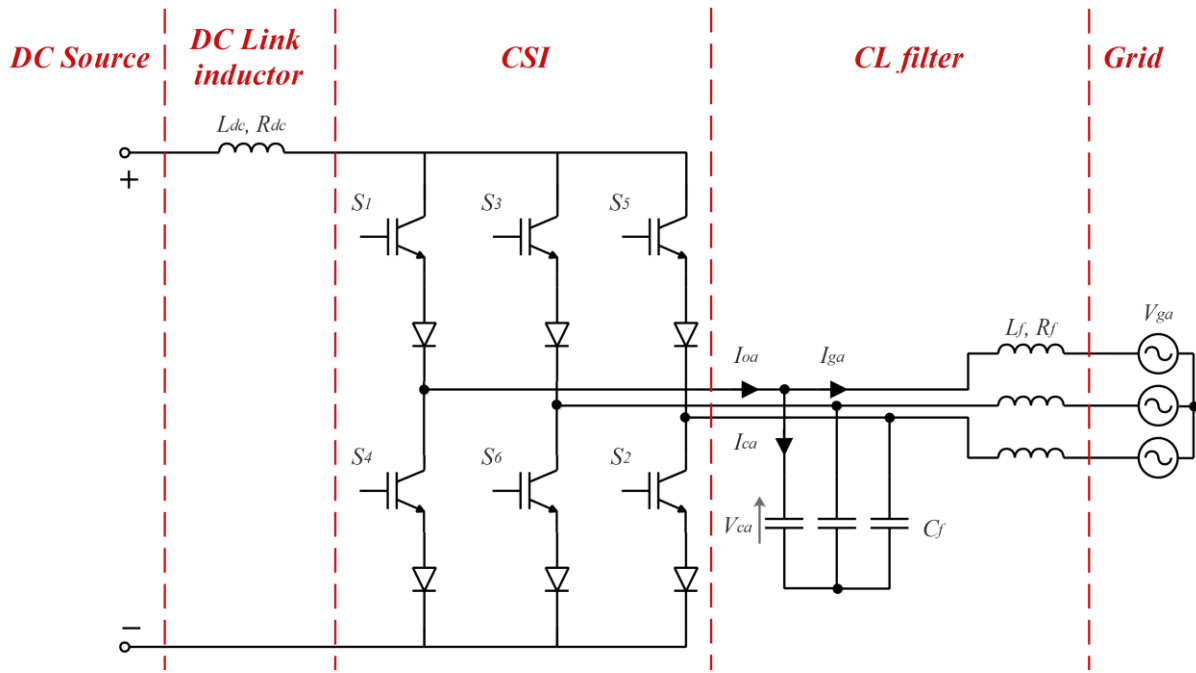
Figure 3.6 Grid-connected CSI scheme

3.4.2.1 CL Filter modeling

The application of Kirchhoff laws on the single wire circuit of grid-connected CSI through *CL* filter of Figure 3.6. yields to the following natural *abc*-frame grid-side model
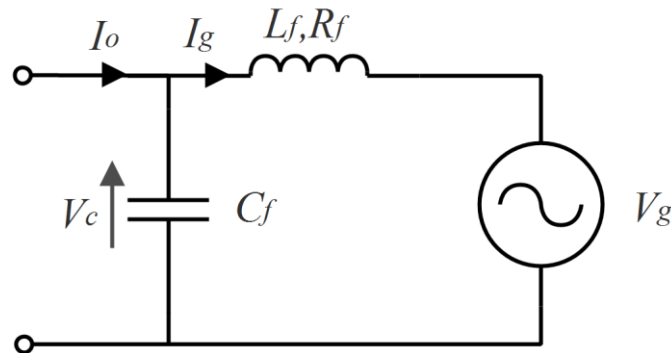
Figure 3.7 CSI connected to grid through CL filter

$$\frac{dI_{g(a,b,c)}}{dt} = -\frac{R_f}{L_f}I_{g(a,b,c)} + \frac{1}{L_f}V_{c(a,b,c)} - \frac{1}{L_f}V_{g(a,b,c)} \tag{13}$$

$$\frac{dV_{c(a,b,c)}}{dt} = \frac{1}{C_f}I_{o(a,b,c)} - \frac{1}{C_f}I_{g(a,b,c)} \tag{14}$$

The transformation of the previous model to the stationary reference frame *αβ* using Concordia matrix gives the following *αβ* state-space model

$$\frac{dI_{g\alpha}}{dt} = -\frac{R_f}{L_f}I_{g\alpha} + \frac{1}{L_f}V_{c\alpha} - \frac{1}{L_f}V_{g\alpha} \tag{15}$$

$$\frac{dI_{g\beta}}{dt} = -\frac{R_f}{L_f}I_{g\beta} + \frac{1}{L_f}V_{c\beta} - \frac{1}{L_f}V_{g\beta} \tag{16}$$

$$\frac{dV_{c\alpha}}{dt} = \frac{1}{C_f}I_{o\alpha} - \frac{1}{C_f}I_{g\alpha} \tag{17}$$

$$\frac{dV_{c\beta}}{dt} = \frac{1}{C_f}I_{o\beta} - \frac{1}{C_f}I_{g\beta} \tag{18}$$

Which can be further represented by following matrix form

$$\frac{d}{dt}\begin{bmatrix} I_{g\alpha} \\ I_{g\beta} \\ V_{c\alpha} \\ V_{c\beta} \end{bmatrix} = \begin{bmatrix} -\dfrac{R_f}{L_f} & 0 & \dfrac{1}{L_f} & 0 \\ 0 & -\dfrac{R_f}{L_f} & 0 & \dfrac{1}{L_f} \\ -\dfrac{1}{C_f} & 0 & 0 & 0 \\ 0 & -\dfrac{1}{C_f} & 0 & 0 \end{bmatrix}\begin{bmatrix} I_{g\alpha} \\ I_{g\beta} \\ V_{c\alpha} \\ V_{c\beta} \end{bmatrix} + \begin{bmatrix} \dfrac{1}{C_f} & 0 & 0 & 0 \\ 0 & \dfrac{1}{C_f} & 0 & 0 \\ 0 & 0 & -\dfrac{1}{L_f} & 0 \\ 0 & 0 & 0 & -\dfrac{1}{L_f} \end{bmatrix}\begin{bmatrix} I_{o\alpha} \\ I_{o\beta} \\ V_{g\alpha} \\ V_{g\beta} \end{bmatrix} \tag{19}$$

Where, $I_{g\alpha}$, $I_{g\beta}$, $V_{c\alpha}$, $V_{c\beta}$ are state variables and $I_{o\alpha}$, $I_{o\beta}$, $V_{g\alpha}$, $V_{g\beta}$ are inputs.

In the other side, the *dq* frame model can be derived using the Park transformation as

$$\frac{dI_{gd}}{dt} = -\frac{R_f}{L_f}I_{gd} + \omega I_{gq} + \frac{1}{L_f}V_{cd} - \frac{1}{L_f}V_{gd} \tag{20}$$

$$\frac{dI_{gq}}{dt} = -\frac{R_f}{L_f}I_{gq} - \omega I_{gd} + \frac{1}{L_f}V_{cq} - \frac{1}{L_f}V_{gq} \tag{21}$$

$$\frac{dV_{cd}}{dt} = \frac{1}{C_f}I_{od} + \omega V_{cq} - \frac{1}{C_f}I_{gd} \tag{22}$$

$$\frac{dV_{cq}}{dt} = \frac{1}{C_f}I_{oq} - \omega V_{cd} - \frac{1}{C_f}I_{gq} \tag{23}$$

And can represented by the following matrix form

$$\frac{d}{dt}\begin{bmatrix} I_{gd} \\ I_{gq} \\ V_{cd} \\ V_{cq} \end{bmatrix} = \begin{bmatrix} -\dfrac{R_f}{L_f} & \omega & \dfrac{1}{L_f} & 0 \\ -\omega & -\dfrac{R_f}{L_f} & 0 & \dfrac{1}{L_f} \\ -\dfrac{1}{C_f} & 0 & 0 & \omega \\ 0 & -\dfrac{1}{C_f} & -\omega & 0 \end{bmatrix}\begin{bmatrix} I_{gd} \\ I_{gq} \\ V_{cd} \\ V_{cq} \end{bmatrix} + \begin{bmatrix} \dfrac{1}{C_f} & 0 & 0 & 0 \\ 0 & \dfrac{1}{C_f} & 0 & 0 \\ 0 & 0 & -\dfrac{1}{L_f} & 0 \\ 0 & 0 & 0 & -\dfrac{1}{L_f} \end{bmatrix}\begin{bmatrix} I_{od} \\ I_{oq} \\ V_{gd} \\ V_{gq} \end{bmatrix} \tag{24}$$

Where, I_{gd}, I_{gq}, V_{cd}, V_{cq} are state variables and I_{od}, I_{oq}, V_{gd}, V_{gq} are inputs.

In the dq-frame, the d and q differential equations for the grid current and the capacitor voltage are dependent due to the cross-coupling terms.

3.4.2.2 Design criteria

The aim of a grid-connected inverter CSI is to supply good quality power with low distorted current to the grid while meeting the required power factor. The primary aim of the low-pass filter design is that the CSI is able to comply with the specified grid requirements while producing a negligibly small power loss of damping resistance [3.13]-[3.16].

Two steps for the design of the *CL* filter are considered [3.13]:

- First, the inductor's value is chosen in order to attenuate the current harmonics, and let its ripple within a limit, to maintain a particular THD.

- The second step is choosing the value of the capacitor in such a way to have a suitable cross-over frequency, to achieve a desired attenuation of the dominant harmonics.

3.4.2.3 Filter resonance and damping

The grid current is subjected to two disturbances: the CSI output current I_o and the grid voltage V_g. Therefore, neglecting the internal resistance of the inductor, the transfer from I_o to I_g is done by the *CL* filter's transfer function (TF) given by

$$H(s) = \frac{1}{s^2 C_f L_f + 1} \tag{25}$$

A bode plot of this TF is given in Figure 3.8.

The filter cut-off frequency f_c is commonly referred as the resonant frequency f_R, as the filter has an infinite gain at that frequency if there is no damping resistance as shown in the bode plot. [3.14]

The resonant behavior induced by the *CL* filter can be attenuated with passive or active damping methods. The output filter must be accurately damped to avoid any large amplification at the resonant frequency. There is already some damping naturally due to series losses in the capacitor and the inductor. However, it is generally the case that more damping is required. The most elementary method to damp the resonance is to add a resistor in series or in parallel with the inductor or the capacitor of the filter, which is commonly known as passive damping. [3.14]-[3.19]. The resonant frequency can be given by

$$f_R = \frac{1}{2\pi\sqrt{L_f C_f}} \hspace{3cm} (26)$$

Quality factor *Q* is the inverse of damping and it is related to the filter gain at the resonant frequency. Note that the filter gain defines the ratio of output to input current I_g/I_o. The expression for *Q* is related to the filter topology and the type of damping used. An analysis of various practical filter topologies is given below in Table 3.2.

Table 3.2 shows four different *CL* filter configurations which differ in the location of the damping resistor. The table also provides the transfer functions *H(s)*, quality factor *Q* and the high frequency attenuation or roll-off rate for each configuration.

Where, $Z_0 = \sqrt{\dfrac{L_f}{C_f}}$ is the characteristic impedance of the filter.

The first configuration uses a resistor in series with the capacitor of the *CL* filter. This causes the filter to have a first-order high frequency roll-off. The high frequency impedance of the filter is also increased. The damping resistor in this arrangement mainly sees the high-frequency current components and has a moderate power dissipation.

A resistor in parallel with the capacitor in second configuration acts essentially as a resistive load which damps the filter. As it can be seen in the circuit this resistor has the full fundamental output voltage across it, and hence the high power dissipation will make it impractical.

The third configuration in table 3.2 has a resistor in parallel with the filter inductor which gives it a first-order high frequency roll-off. The power dissipation in R_d would be expected to be

much smaller compared to the other types as the fundamental voltage drop across the inductor is small.

The last configuration however has a resistor in series with the filter inductor. This configuration has two problems: a resistive output impedance at low frequencies and high losses. At low frequencies, the impedance of the filter is equal to the damping resistor. The series resistor in the fourth configuration sees the full grid current and thus has high losses, but has a second-order roll-off at high frequencies which is a positive feature. [3.14],[3.19]

The bode plot of the undamped *CL* filter and the four configurations is depicted in Figure 3.8.

Table 3.2 Resistive damping configurations [3.14]

	Circuit	Transfer Function $H(s)$	Quality Factor Q	Roll-off Rate Beyond f_R
1		$\dfrac{sC_f R_d + 1}{s^2 C_f L_f + sC_f + 1}$	$\sqrt{\left(\dfrac{Z_0}{R_d}\right)^2 + 1}$	-20 dB/decade
2		$\dfrac{R_d}{s^2 C_f L_f R_d + sL_f + R_d}$	$\dfrac{R_d}{Z_0}$	-40 dB/decade
3		$\dfrac{sL + R_d}{s^2 C_f L_f R_d + sL_f + R_d}$	$\sqrt{\left(\dfrac{R_d}{Z_0}\right)^2 + 1}$	-20 dB/decade
4		$\dfrac{1}{s^2 C_f L_f + sC_f R_d + 1}$	$\dfrac{Z_0}{R_d}$	-40 dB/decade
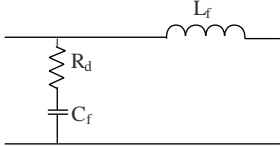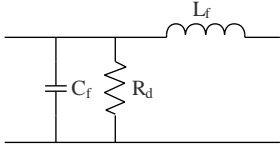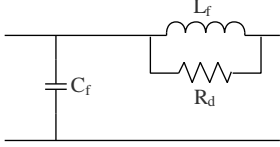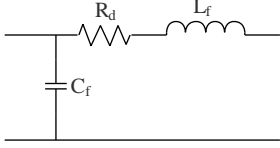
According to this analysis, among these four configurations, parallel damping resistor with the filter inductor (configuration 3) seems to be the most suitable passive damping method. Furthermore, it is still considered as the most popular technique in the literature. One constraint for the value of the damping resistor for this configuration is that it should be higher enough than the impedance of the inductor. [3.20]

$$R_d > \omega L_f \tag{27}$$
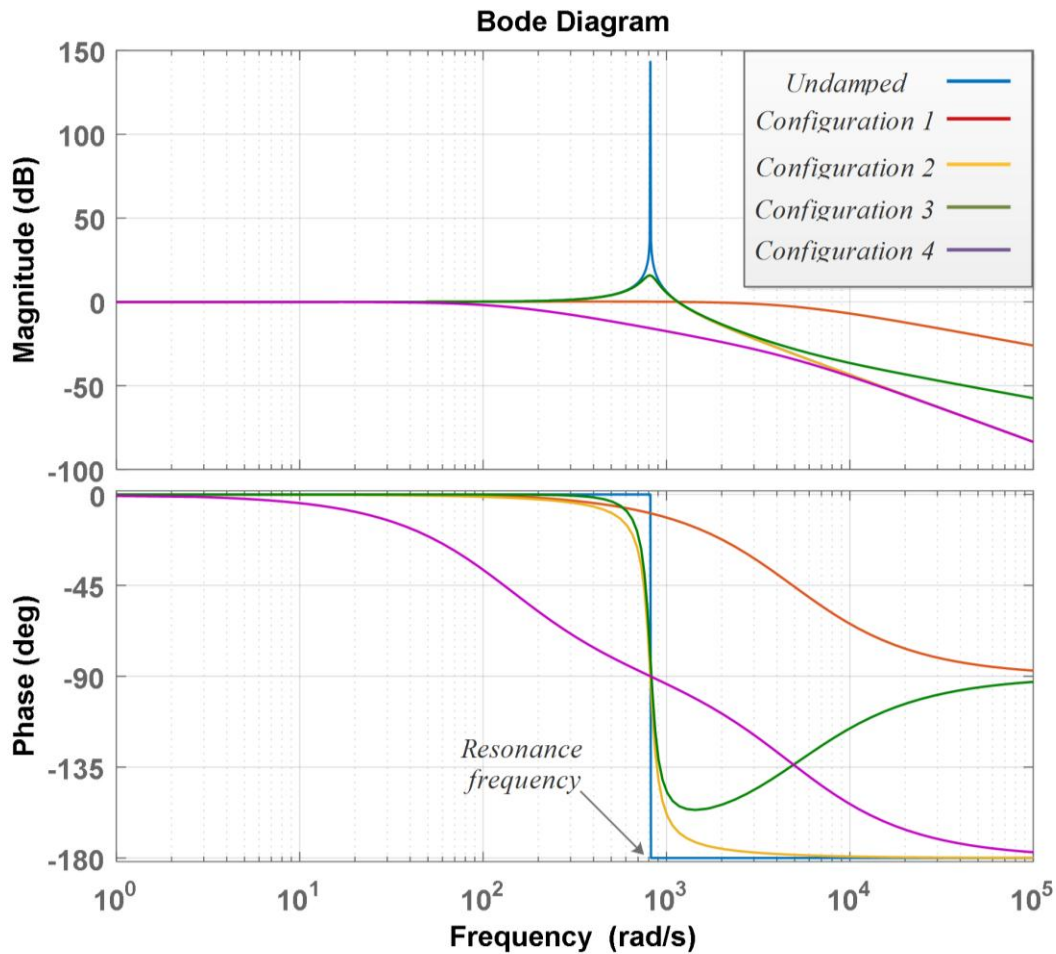
Figure 3.8 bode plot of the different CL filter configurations

Although, the passive damping provides desired resonance damping, it also causes reduction in the attenuation capability and power losses reducing the conversion efficiency by up to 1%. [3.18]. Moreover, the system costs are increased due to additional components and possible cooling elements (especially in high-power applications) [3.13].

Active damping, on the other hand, is performed with different control algorithms, which are used to attenuate the resonant behavior and, due to the absence of resistive elements, power losses are negligible in the filter. Moreover, the attenuation capability of the filter is unaffected [3.16]-[3.19]. Therefore, active damping is adopted and compared with passive damping (configuration 3) for grid-connected CSI in Chapter 5.

3.5 Conclusion

This chapter has presented the design and modeling for stand-alone and grid connected CSI system components. First, a detailed ideal PV cell model has been carried out using the single diode equivalent circuit model. Then, the practical PV cell and PV array models are derived by adding to the model other key parameters. It has been shown also the effect of sun irradiance and ambient temperature on the PV characteristics. The CSI working principle is explained, and its model, possible states and current vectors are derived based on the switching constraints. Finally, the chapter has provided the model and design for the output filter for both stand-alone and grid-connected CSI systems. It has been explained that for stand-alone only a capacitor filter is used, whereas in grid-connected CSI a *CL* filter is necessary to enhance the quality of the injected current to the utility. However, resonance may occur in this filter due to the switching harmonics. For this reason, resonance damping is mandatory. Though passive damping using resistors is sufficient to avoid resonance in the filter, it also reduces the efficiency and the filtering capabilities. Therefore, it has been concluded that active damping is the better choice.

References

[3.1]   M. Gradella, J. R. Gazoli, E. R. Filho, "Comprehensive Approach to Modeling and Simulation of Photovoltaic Arrays," *IEEE Trans. on power electronics,* Vol. 24, No. 5, May 2009, pp. 1198–1207

[3.2]   D. Rekioua, E. Matagne, *Optimisation of Photovoltaic Power Systems: Modelisation, Simulation, and Control*. Springer-Verlag, 2012.

[3.3]   N. Femia, G. Petrone, G. Spagnuolo, M. Vitelli, *Power Electronics and Control Techniques for Maximum Energy Harvesting in Photovoltaic Systems*. CRC Press, 2013.

[3.4]   A. Ghosh, S. G. Malla, C. N. Bhende, "Small-signal Modelling and Control of Photovoltaic Based Water Pumping System," *ISA Transactions,* Vol. 57, No. 1, Jul, 2015, pp. 382–389

[3.5]   M. G. Simoes, F. A. Farret, *Modeling Power Electronics and Interfacing Energy Conversion Systems*, John Wiley & Sons, Ltd, 2017.

[3.6]   O. P. Mahela, A. G. Shaik, "Comprehensive Overview of Grid Interfaced Solar Photovoltaic Systems ," *Renewable and Sustainable Energy Reviews*, Vol. 68, No. 1, Dec. 2017, pp. 316–332

[3.7]   A. Radwan, Y. Mohamed, "Power Synchronization Control for Grid-Connected Current-Source Inverter-Based Photovoltaic Systems," IEEE Trans. on Energy Conversion, Vol. 31, No. 3, Sep. 2016, pp. 1023–1036

[3.8]   K. Gnanasambandam, A. Edpuganti, A. K. Rathore, "Optimal Low Switching Frequency Pulse width Modulation of Current-Fed Three-Level Converter for Solar Power Integration," *IEEE Trans. on industrial electronics,* Vol. 63, No. 11, Nov, 2016, pp. 6877–6886

[3.9]   B. K. Bose, *Modern Power Electronics and AC drives*, Prentice Hall PTR, 2002.

[3.10]   B. Wu, *High-power Converters and AC drives*, John Wiley & Sons, Ltd, 2006.

[3.11]   M. H. Rashid, *Power Electronics Handbook, Third Edition*, Butterworth-Heinemann, Ltd, 2011.

[3.12]   A. Singh, A. K. Kaviani, B. Mirafzal, "On Dynamic Models and Stability Analysis of Three-Phase Phasor PWM-Based CSI for Stand-Alone Applications," *IEEE Trans. on industrial electronics,* Vol. 62, No. 5, May, 2015, pp. 2698–2707

[3.13] R. Teodorescu. M. Liserre, P. Rodriguez, *Grid Converters for Photovoltaic and Wind Power Systems*. John Wiley & Sons, Ltd, 2011.

[3.14] G. Ertasgin, "Low-Cost Current-Source 1-ph Photovoltaic Grid-Connected Inverter," Ph.D. dissertation, School of Electrical and Electronic Eng., Adelaide Univ., Adelaide, Australia, 2010.

[3.15] S. Jayalath, M. Hanif, "CL-Filter Design for Grid Connected CSI," *in Proc. IEEE 13th Brazilian Power Electronics Conf.*, Brazil, 2015, pp. 1–6.

[3.16] Y. W. Li, "Control and Resonance Damping of Voltage-Source and Current-Source Converters With LC Filters," *IEEE Trans. on Industrial Electronics*, Vol. 56, No. 5, Nov. 2008, pp. 1511–1521

[3.17] I. Lorzadeh, M. Savaghebi, H. A. Abyaneh, J. M. Guerrero, "Active Damping Techniques for LCL-Filtered Inverters-Based Microgrids," *in Proc. of the 2015 IEEE 10th International SDEMPED*, Portugal, 2015, pp. 1–7.

[3.18] A. Aapro, "Factors in Active Damping Design to Mitigate Grid Interactions in Three-Phase Grid-Connected Photovoltaic Inverters," Ph.D. dissertation, Dept. of Elect. Eng., Tampere Univ. of Tech., Tampere, Finland, 2017.

[3.19] M. Huang, "Control Strategies for Trap Filter Interfaced Three-Phase Grid Connected Converters," Ph.D. dissertation, Dept.of Energy Tech., Aalborg Univ., Aalborg, Denmark, 2015.

[3.20] C. Photong, "A Current Source Inverter with Series AC Capacitors for Transformerless Grid-Tied Photovoltaic Applications," Ph.D. dissertation, Dept.of Electrical and Electronic Eng., Nottingham Univ., Nottingham, UK, 2013.

[3.21] M. H. Mahlooji, H. R. Mohammadi, M. Rahimi, "A review on modeling and control of grid-connected photovoltaic inverters with LCL filter," *Renewable and Sustainable Energy Reviews*, Vol. 81, No. 1, Jan. 2018, pp. 563–578

Chapter 4
Stand-alone current source inverter

4.1 Introduction

CSIs offer many important features when compared with the well-known topology of VSIs. Nevertheless, CSI control strategies are less developed than those of VSI. Available voltage regulation schemes for stand-alone CSIs commonly use controllers such like proportional–integral (PI) controllers, or proportional-resonant (PR) controllers, etc., but this approach is known to suffer from significant steady-state error, slow dynamics, and overshoots. Besides that, the design and tuning of the regulators are always performed in function of the types and values of the connected loads. This leads to lose of stability and accuracy of voltage control during load variations. In order to get over these issues, this chapter proposes new voltage control strategies for stand-alone CSIs, or for the supply of local loads disconnected from the grid during islanding operation of CSI based DG systems. The developed techniques can ensure a fast and accurate voltage control independently of the connected loads. Moreover, they can perform without neither regulations loops, nor modulators. Simulation results using Matlab/Simulink of the proposed techniques have been carried out for different loads and during different tests. In the last part of this chapter, experimental results for a low power CSI prototype controlled by a digital signal processor (DSP) are exposed in order to demonstrate the effectiveness and the feasibility of the developed voltage control strategies for stand-alone CSI.

4.2 Finite-set model predictive voltage control (FS-MPVC)

Model predictive control (MPC) is currently one of the most appropriate approaches for the control of complex systems. MPC has a series of characteristics that make it very attractive: it is simple, intuitive, easy to implement, and can include nonlinearities, limitations, etc. MPC is an advanced method that explicitly uses the system's model to predict future changes in the process. The basic idea is to calculate, at each sampling instant, a sequence of optimal control of a prediction horizon to minimize a cost function, which expresses the objective of the control. For the control of power converters, a type of MPC called finite-set model predictive control (FS-MPC) represents one of the best options. FS-MPC is a model-based optimization algorithm

that performs a set of calculations during each sampling period. The number of iterations in the optimization algorithm are determined according to the possible number of converter switching states. The power semiconductor switch in any converter possesses two discrete states: ON ('1') or OFF ('0'). Thus the number of switching combinations (switching states) in any converter are limited to a finite set. [4.1]-[4.5]

In this chapter, a Finite-set model predictive voltage control for CSI is proposed. FS-MPVC for CSI is a new and simple control strategy that uses the system model including the inverter and the output filter for the prediction of the future behavior of the load voltages, then using a cost function, the optimal control is generated and applied during the whole next sampling period. Figure 4.1 depicts the block diagram of FS-MPVC control scheme for stand-alone CSI.
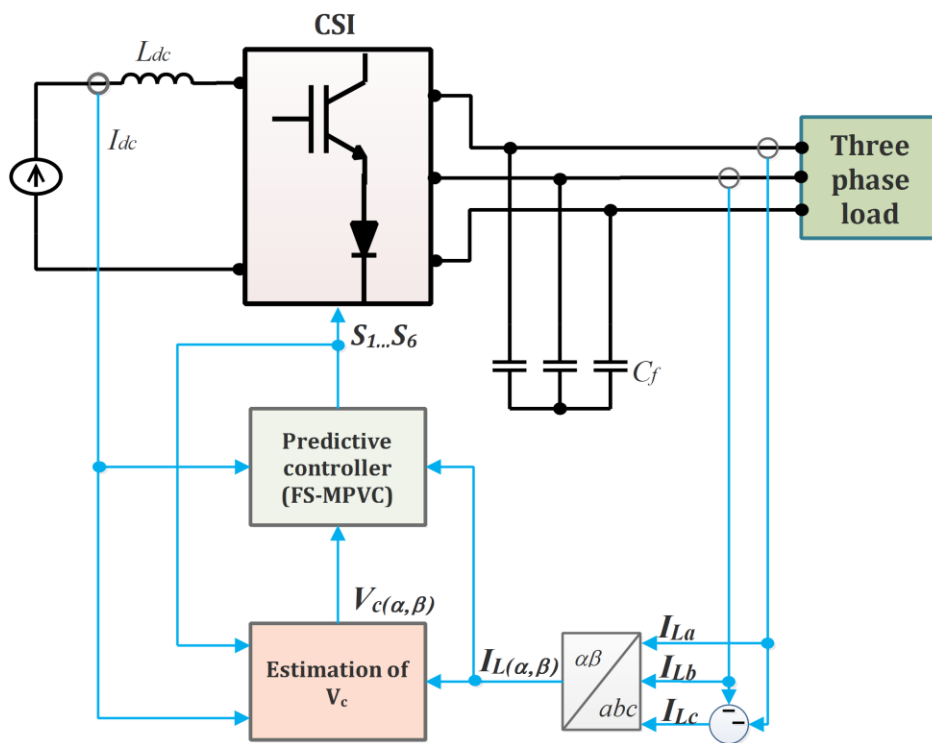

Figure 4.1 Block diagram of FS-MPVC control scheme

4.2.1 Predictive controller

In this structure, the DC current, the load currents, and voltages, are measured. These measures are necessary to predict the behavior of the controlled variables, which are the load voltages. Then, based on these predictions, a cost function is minimized and the appropriate current vector is selected. Thus, the selection generates pulses to control the power switches of the inverter.

4.2.1.1 Prediction model

The essence of predictive control is the system prediction model. In general the performance of the predictive controller depends highly on the prediction model [4.1].

Considering that the continuous-time load side model of CSI including the capacitor filter in the stationary reference frame is given by

$$I_{o(\alpha,\beta)} = C_f \frac{dV_{c(\alpha,\beta)}}{dt} + I_{L(\alpha,\beta)} \tag{1}$$

The continuous-time model of equation (1) needs to be converted to discrete-time. Several discretization methods can be used in order to obtain a discrete-time model suitable for the calculation of predictions, such as: forward difference, backward difference, bilinear transformations (combination of forward and backward difference), impulse-invariant and zero-order hold [4.2].

Due to the first order nature of the model in (1), a first-order approximation for the derivative can be obtained by forward Euler method. Such as for a generic variable x [4.1]-[4.5]

$$\frac{dx}{dt} = \frac{x(k+1) - x(k)}{T_s} \tag{2}$$

The application of the approximation in (2) gives

$$I_{o(\alpha,\beta)}[k] = C_f \left(\frac{V_{c(\alpha,\beta)}[k+1] - V_{c(\alpha,\beta)}[k]}{T_s} \right) + I_{L(\alpha,\beta)}[k] \tag{3}$$

Thus, the nine possible load voltage predictions can be obtained from the previous equation as follows

$$V_{c(\alpha,\beta)}[k+1] = \frac{T_s}{C_f} \left(I_{o(\alpha,\beta)}[k] - I_{L(\alpha,\beta)}[k] \right) + V_{c(\alpha,\beta)}[k] \tag{4}$$

It is obvious that in (4) the prediction needs measurement of load currents and voltages. However, only load currents are measured, whereas the capacitor voltages are estimated using the backward Euler formula which leads to the following equation

$$V_{c(\alpha,\beta)}[k] = \frac{T_s}{C_f} \left(I_{o(\alpha,\beta)}[k-1] - I_{L(\alpha,\beta)}[k-1] \right) + V_{c(\alpha,\beta)}[k-1] \tag{5}$$

Where, the output currents $I_{o\alpha}$, $I_{o\beta}$ can be reconstructed using the measured DC current, and the switching signals as follows

$$I_{o\alpha} = \frac{1}{3}I_{dc}\left[(2(S_1 - S_4) - (S_3 - S_6) - (S_5 - S_2)\right] \tag{6}$$

$$I_{o\beta} = \frac{1}{\sqrt{3}}I_{dc}\left[(S_3 - S_6) - (S_5 - S_2)\right] \tag{7}$$

4.2.1.2 Cost function optimization

Once all predicted variables are obtained, the different values are used to evaluate a cost function which deals with all control objectives. Since the control objective in this system is to make the load voltages pursue their references, the cost function is defined as the absolute error between the predicted references and the predicted load voltages. [4.3]

$$g_j = \left\| V_{c\alpha}^*[k+1] - V_{c\alpha}[k+1] \right\| + \left\| V_{c\beta}^*[k+1] - V_{c\beta}[k+1] \right\| \tag{8}$$

Where j denotes the index of the inverter current vector used in the prediction of the load voltages.

In (8), the future load voltage reference vector can be estimated using fourth-order Lagrange extrapolation, given by [4.5]

$$V_c^*[k+1] = 4V_c^*[k] - 6V_c^*[k-1] + 4V_c^*[k-2] - V_c^*[k-3] \tag{9}$$

However, no extrapolation is needed if the sampling time is short enough. [4.1],[4.2],[4.5]

The load voltage vector equals its reference when $g = 0$. Therefore, the goal of the cost function optimization is to achieve a g value as close to zero as possible. Hence, the switching state that minimizes the cost function is chosen and then applied at the next sampling instant.

The flowchart of the algorithm used to implement the predictive voltage controller is shown in Figure 4.2. and the predictive controller scheme is depicted in Figure 4.3.

In Figure 4.3 g_{op} denotes the optimal value of cost function g, and j_{op} is its index.
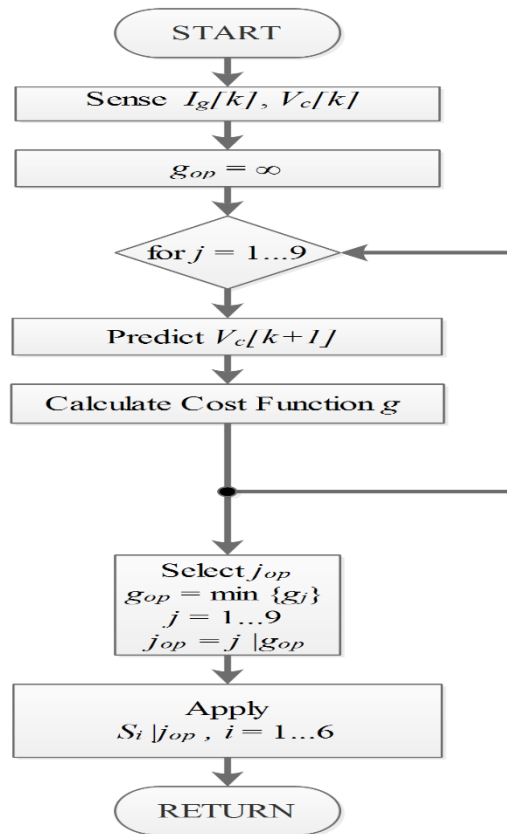
Figure 4.2 FS-MPVC algorithm flowchart
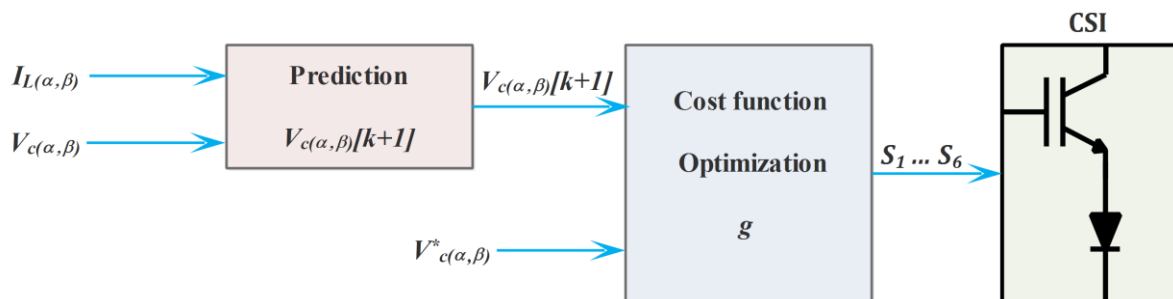
Figure 4.3 FS-MPVC controller scheme

4.3 Proposed CSI switching algorithm

A new voltage control strategy is presented in this part. It is based on a simple algorithm which evaluates the error between load voltages and their corresponding references and makes the decision by generating the suitable switching signals to the power switches of the inverter in order to reduce the voltages' errors. The block diagram of proposed switching algorithm control scheme for stand-alone CSI is shown in Figure 4.4.
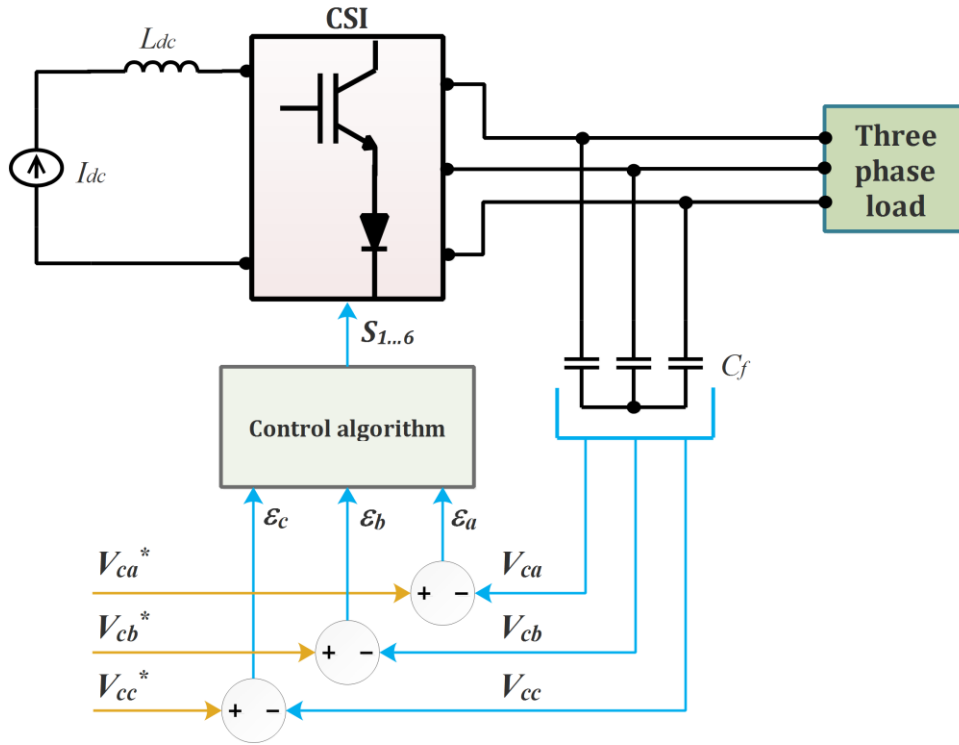
Figure 4.4 Proposed switching algorithm control scheme

4.3.1 Principle of operation

The proposed method consists in reducing the gap between the actual and the reference voltages. Since in the control of CSIs, only one of the upper switches and one of the lower switches can conduct simultaneously, the selection of the two ON switches is done in such a way to correct the two out of three largest errors. The control pulses are generated to make the DC current circulate in the two phases and reduce their errors. The third phase will be controlled only when its error will be dominating against one of the previously controlled phases.

When in an inverter leg, an upper switch is ON, the change in the corresponding load voltage (capacitor voltage) is positive, because the output current is positive ($I_o=I_{dc}$), and higher than the load current as described in the following equation.

$$I_{o(a,b,c)} > 0 \Rightarrow \frac{dV_{c(a,b,c)}}{dt} = \frac{1}{C_f}(I_{o(a,b,c)} - I_{L(a,b,c)}) > 0 \qquad (10)$$

Thus, the capacitor voltage will have a positive ramp (capacitor charging).

When, a lower switch in one of the inverter legs is ON, the corresponding output current I_o, is negative ($I_o=-I_{dc}$), hence, the change in the load voltage is negative also, as

$$I_{o(a,b,c)} < 0 \Rightarrow \frac{dV_{c(a,b,c)}}{dt} = \frac{1}{C_f}(I_{o(a,b,c)} - I_{L(a,b,c)}) < 0 \qquad (11)$$

Thus, the capacitor voltage have a negative ramp (capacitor discharging).

Whereas, in the third leg, both switches are OFF ($I_o=0$), the corresponding capacitor discharges slowly through the load, so the change in the capacitor voltage is lower than the capacitor connected to the active lower switch.

$$I_{o(a,b,c)} = 0 \Rightarrow \frac{dV_{c(a,b,c)}}{dt} = -\frac{I_{L(a,b,c)}}{C_f} < 0 \qquad (12)$$

The phase voltage error is obtained by

$$\varepsilon_{a,b,c} = V^*_{c(a,b,c)} - V_{c(a,b,c)} \qquad (13)$$

So, the selection of the two conducting switches is done by searching the maximum and the minimum voltage errors. The upper switch of the phase with maximum error, and the lower switch of the phase with minimum error will be switched ON at the actual sampling time.

Figure 4.5 gives an example to describe the working principle of the proposed algorithm. At instant (1) of Figure 4.5(a), the phase with the maximum error is phase (*a*), thus, its corresponding upper switch (S_1) is turned *ON* to increase the capacitor voltage by charging the capacitor to reduce error ε_a. In the other hand, the minimum voltage error is in phase (*c*), hence, the corresponding lower switch (S_2) is turned *ON*, to correct this error by discharging the capacitor as shown in Figure 4.5(b). The voltage error in this phase (*b*) does not represent neither the maximum nor the minimum. So, this leg of the inverter is not connected to the load, and the corresponding capacitor discharges slowly through the load. However, in the following sampling instant (2), error in phase (*b*) is dominating against the other phase errors and represents the maximum of them, so, the corresponding upper switch will be turned *ON* to reduce this error by rising the capacitor voltage. Figure 4.5 (b) show the flow paths for the three phases currents during the first sampling interval.
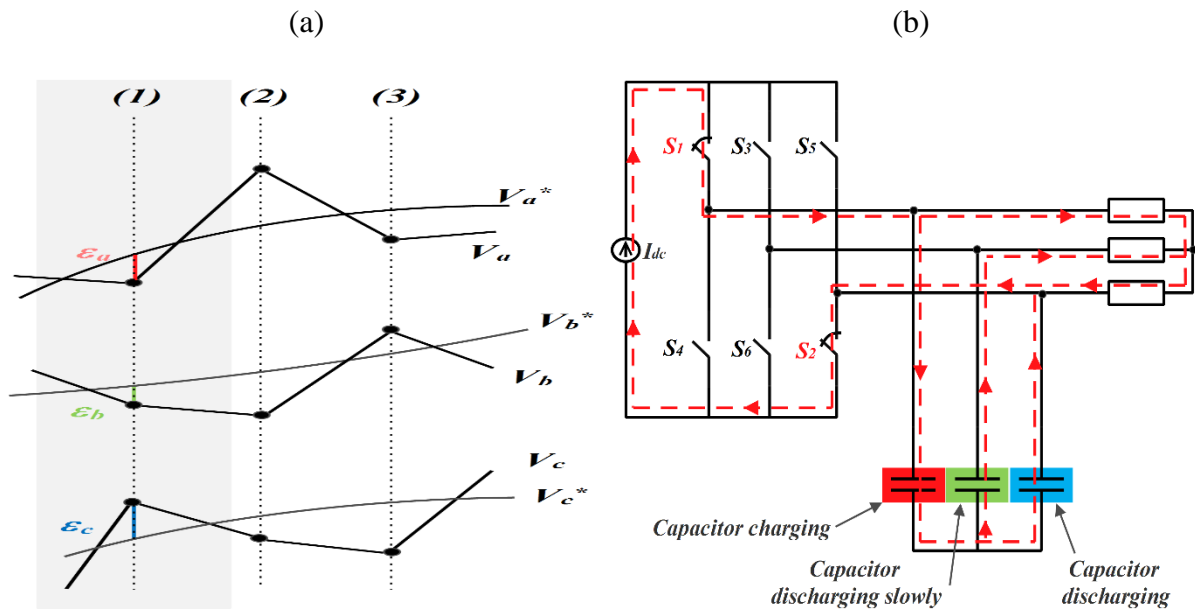
Figure 4.5 Description of switching algorithm operation principle: (a) load voltages along with their references, (b) three phase currents flow paths during first sampling intervalle

The flowchart of the proposed algorithm is shown in Figure 4.6
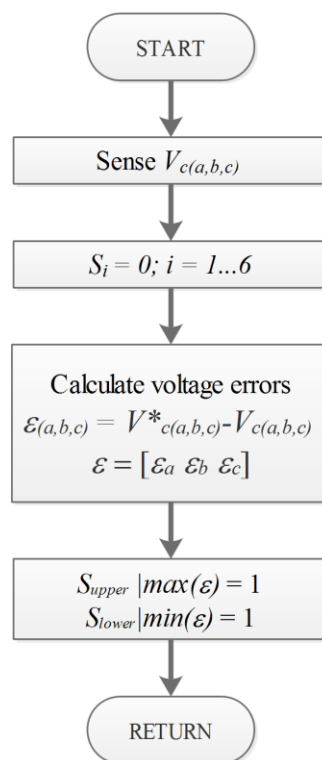
Figure 4.6 Proposed switching algorithm flowchart

The algorithm in Figure 4.6 can also be implemented using logical ports as depicted in the following figure.
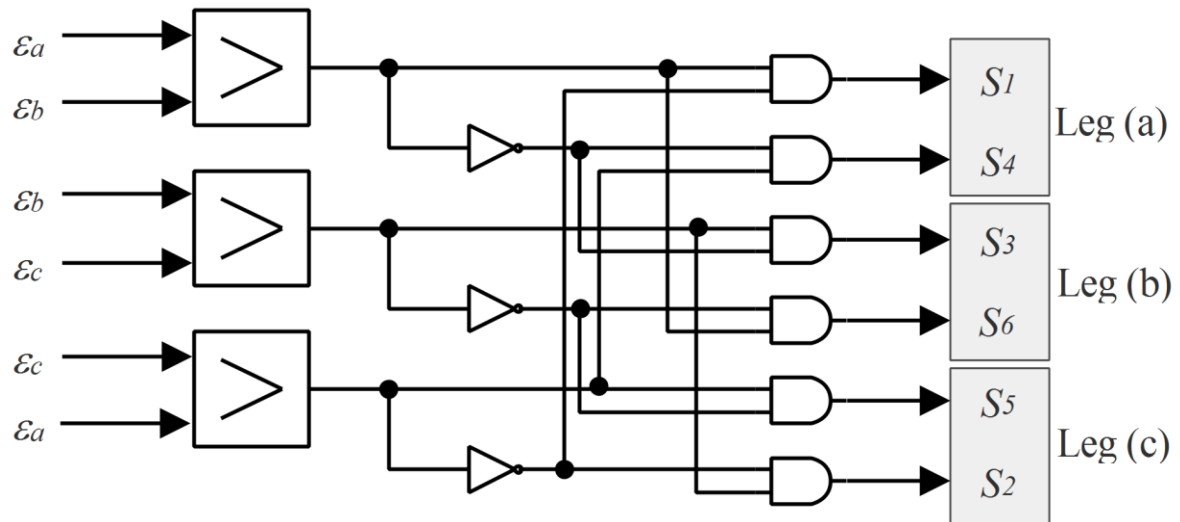
Figure 4.7 Generator of triggering signals of the proposed controller using logical ports

4.4 Simulation results

The control schemes of the proposed FS-MPVC (Figure 4.1) and the proposed switching algorithm (Figure 4.4) have been simulated using Matlab/Simulink® software, using the system parameters listed in table A.1 (Appendix A) for different types of linear and non-linear loads. Robustness tests have been accomplished also, to assess the performance of the proposed CSI voltage controllers. The simulation type is discrete with a sampling time of 40μs.

4.4.1 Resistive load

(a)

(b)

(c)
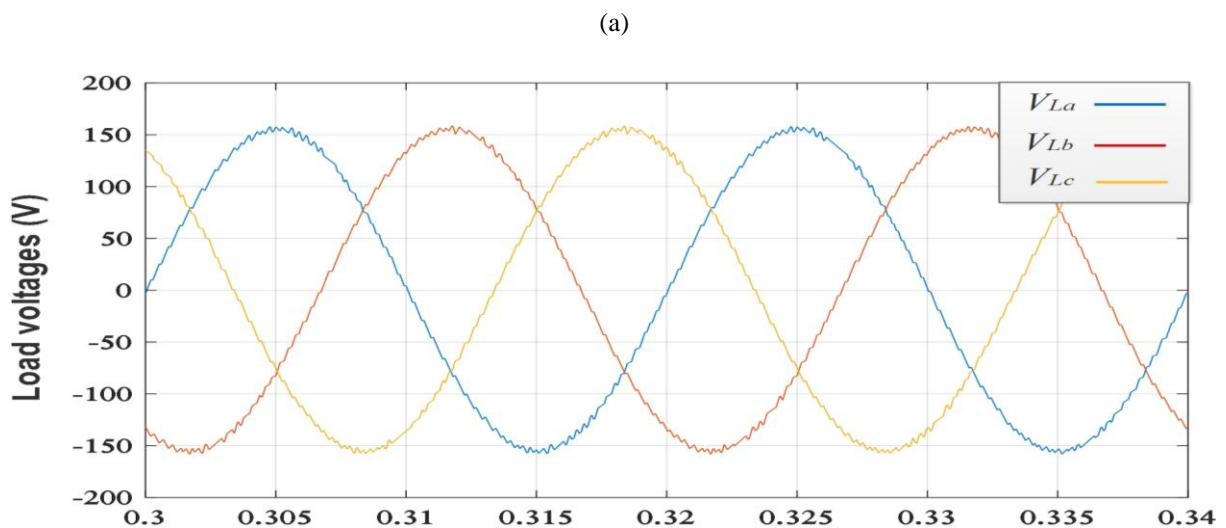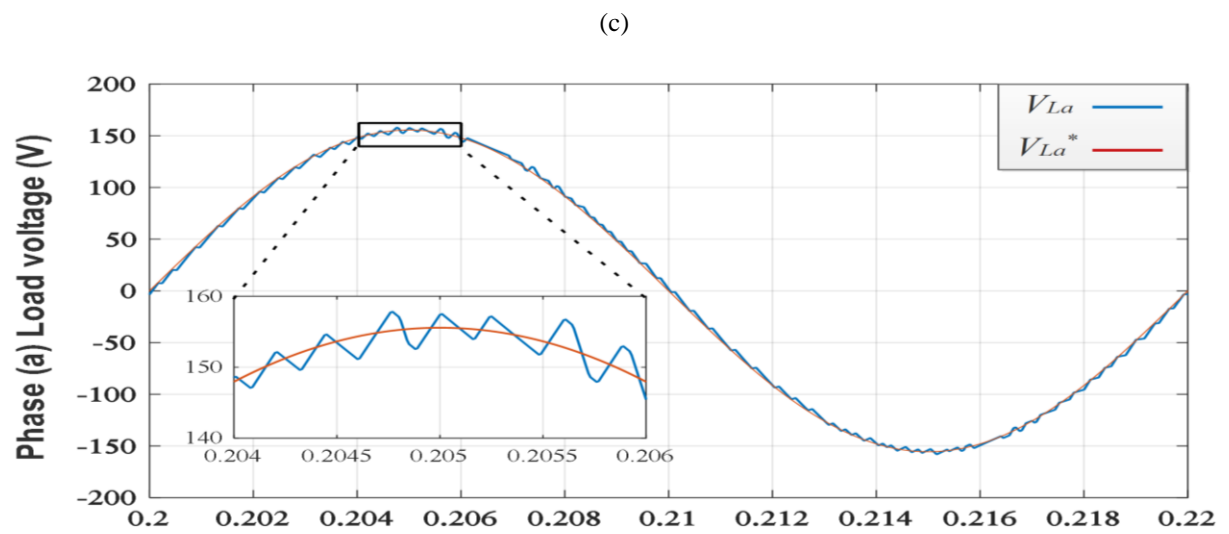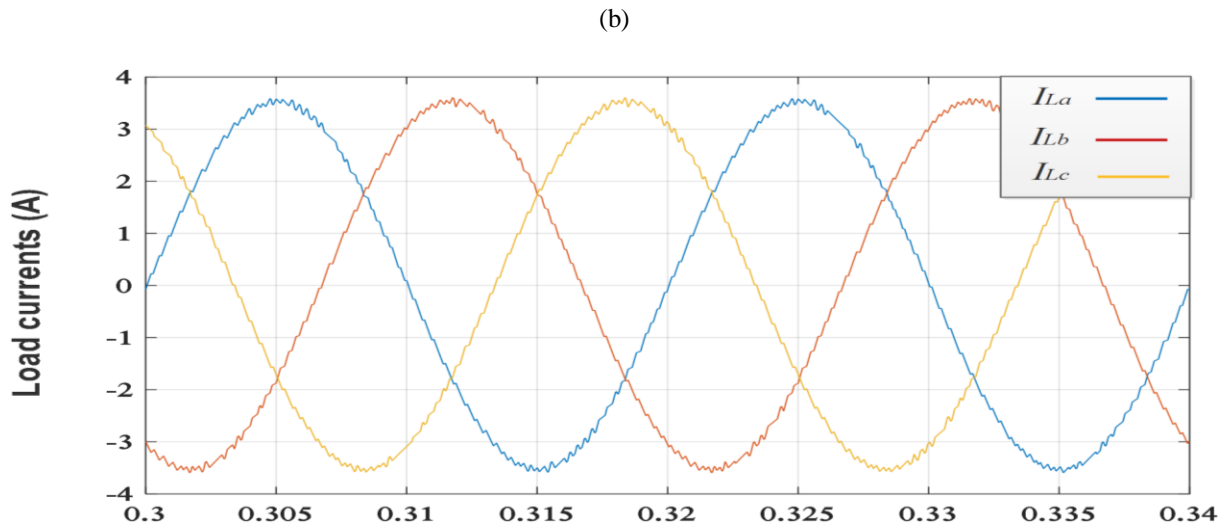
Figure 4.8 FS-MPVC responses of: (a) load voltages, (b) load currents, (c) phase (*a*) load voltage along with its reference

(a)

(b)

(c)
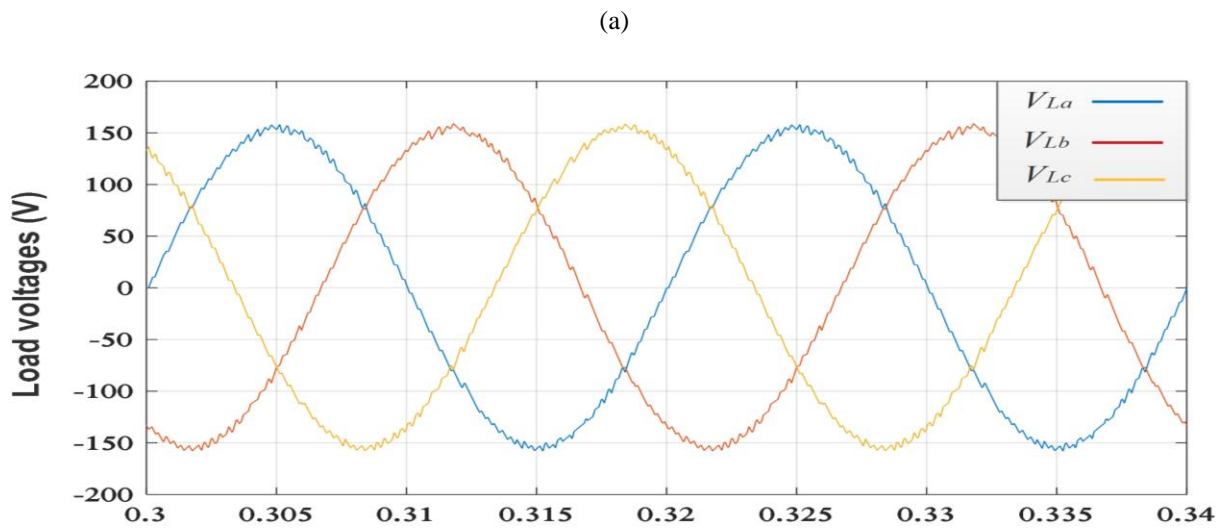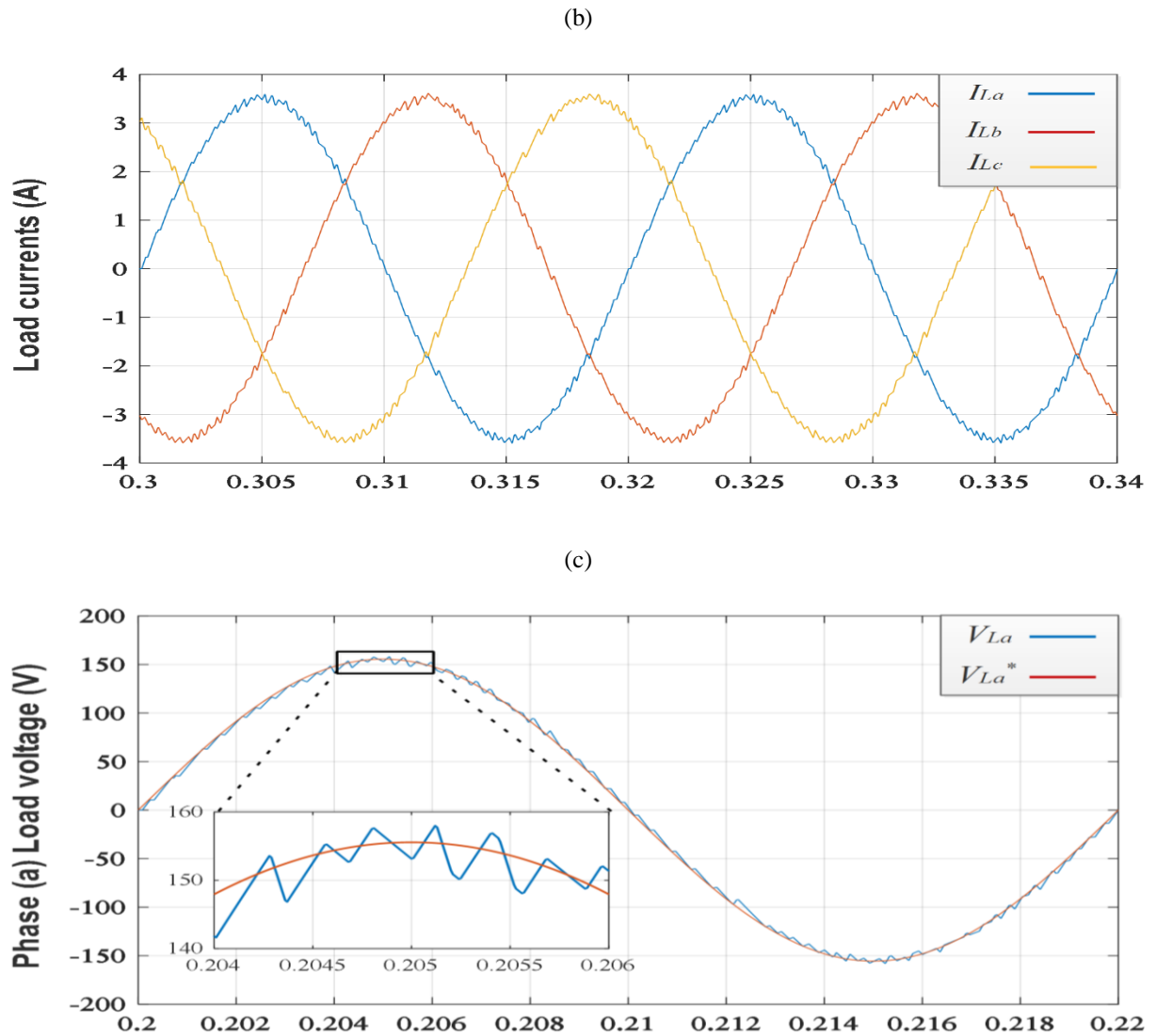
Figure 4.9 Proposed switching algorithm responses of: (a) load voltages, (b) load currents, (c) phase
(*a*) load voltage along with its reference

Figure 4.8 and Figure 4.9 show the responses of load voltages, load currents, and phase (*a*) load
voltage along with its reference, for FS-MPVC and the proposed switching algorithm,
respectively. It can be seen that the load voltages and currents are practically sinusoidal and
low distorted. The THD was computed as 1.42% for FS-MPVC and 1.66% for the switching
algorithm. It is shown also that the load voltages track their references quasi-perfectly for both
proposed methods.

4.4.2 Resistive-inductive load

(a)

(b)
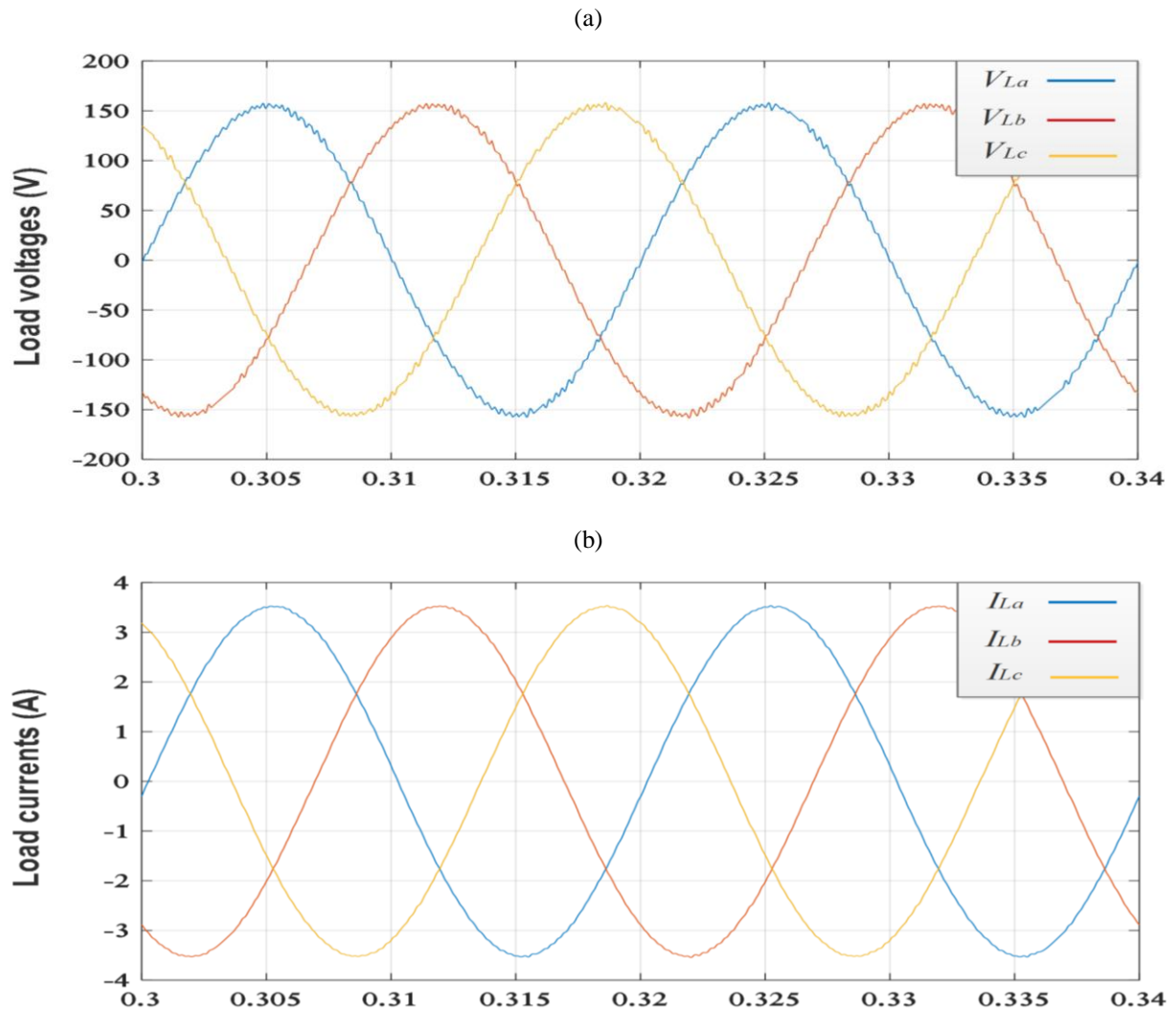
Figure 4.10 FS-MPVC responses of: (a) load voltages, (b) load currents for *RL* type load

(a)

(b)
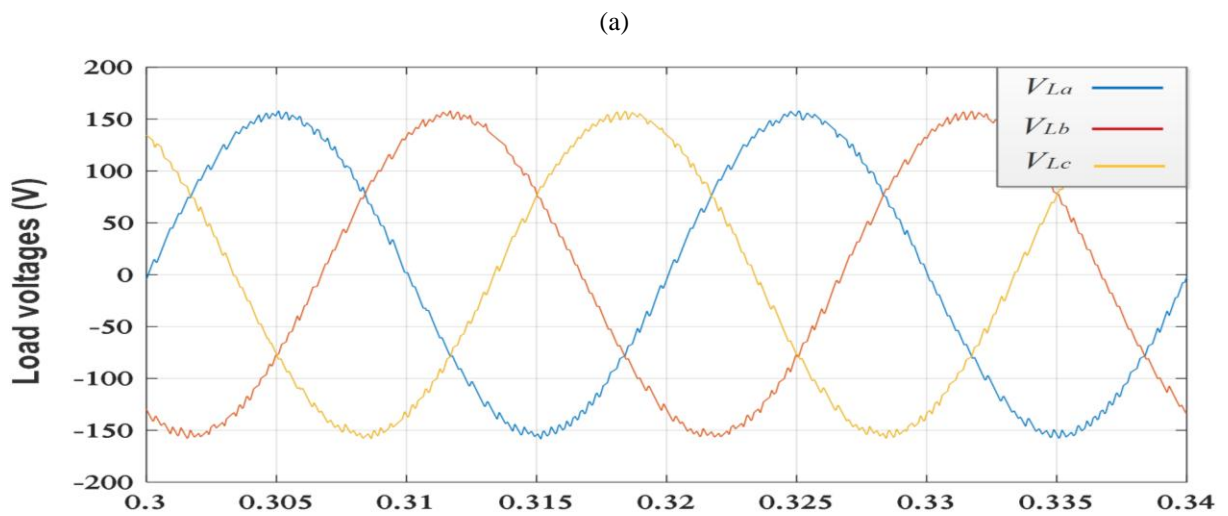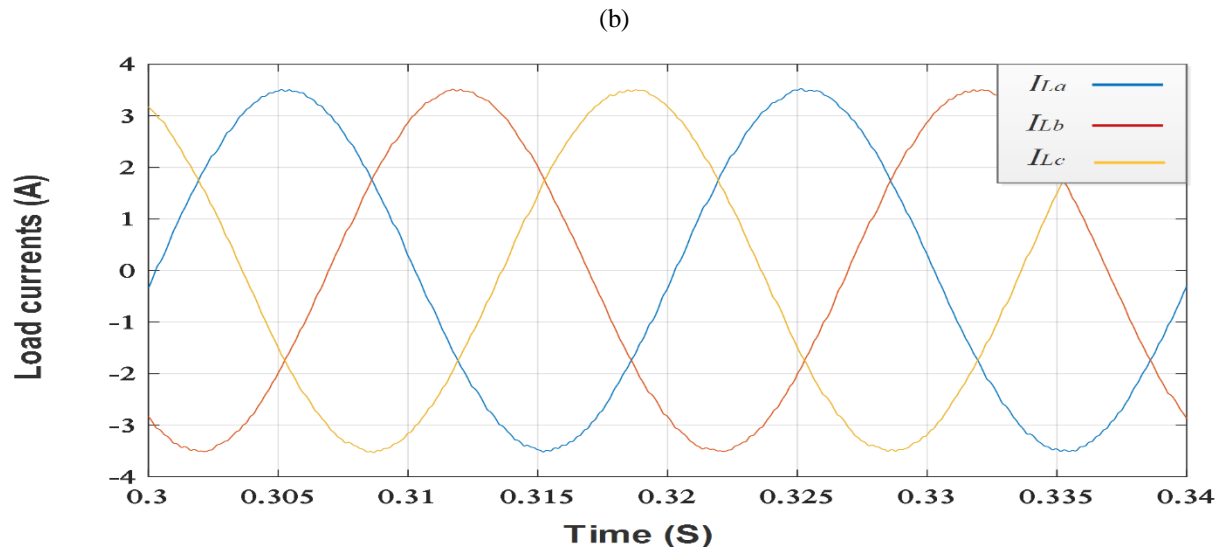
Figure 4.11 Proposed switching algorithm responses of: (a) load voltages, (b) load currents for *RL* type load

For a resistive-inductive load, the obtained waveforms of load voltages and load currents are sinusoidal, and lowly distorted. However, it is obvious that load currents are smoother than those using a pure resistive load due to the presence of inductor.

4.4.3 Non-linear load

To test the proposed voltage controllers with a non-linear load, the diode rectifier feeding a resistor in parallel with a capacitor (Figure 4.12) is used.
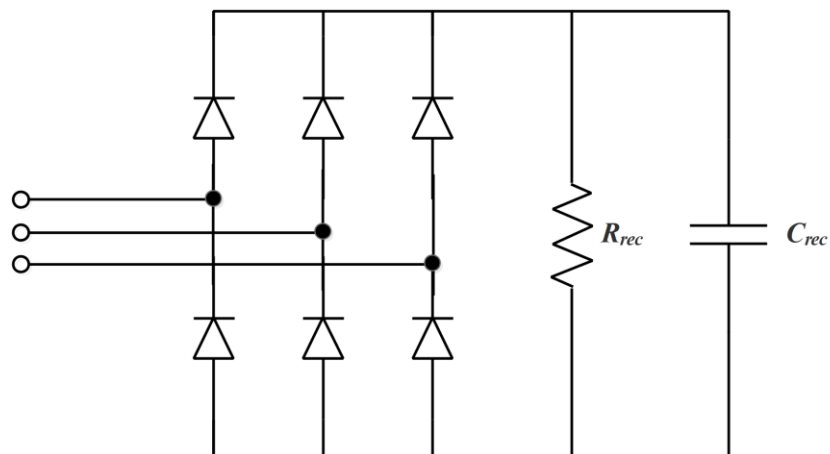
*Figure 4.12* Diode rectifier used as a non-linear load (R_{rec}=100Ω, C_{rec}=4.7μF)

(a)

(b)
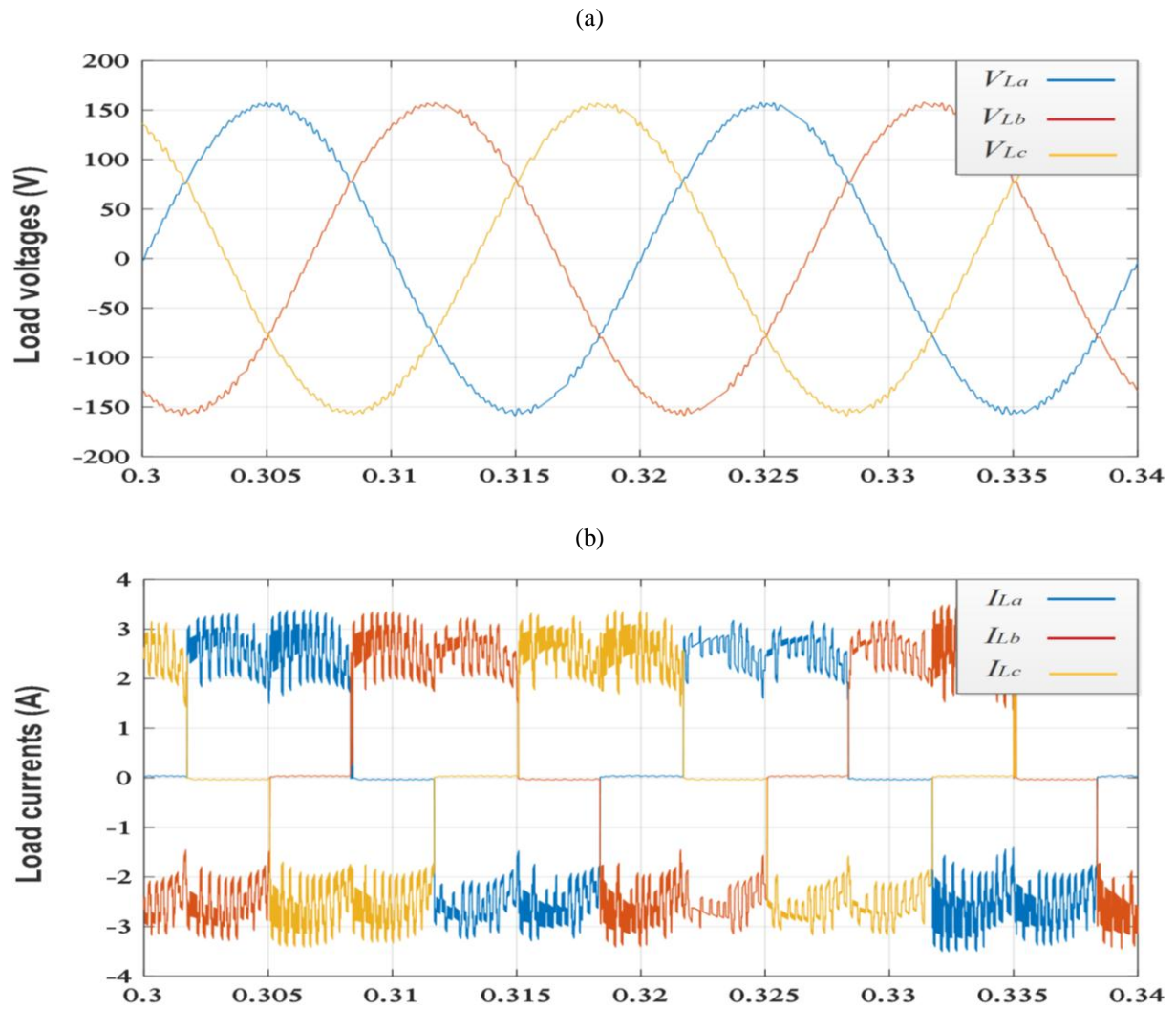
Figure 4.13 FS-MPVC responses of: (a) load voltages, (b) load current for non-linear load

(a)

(b)
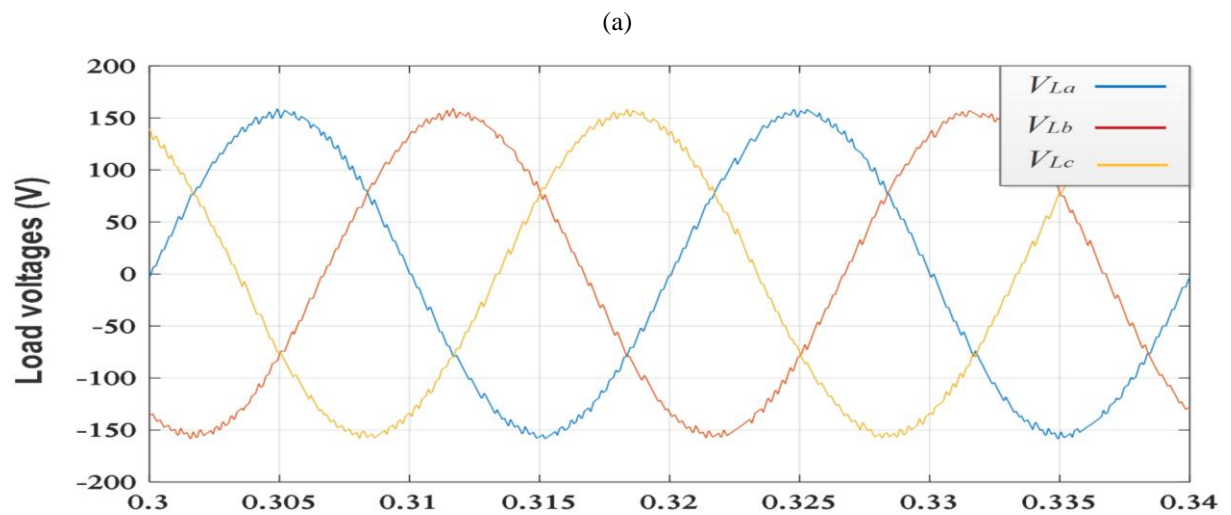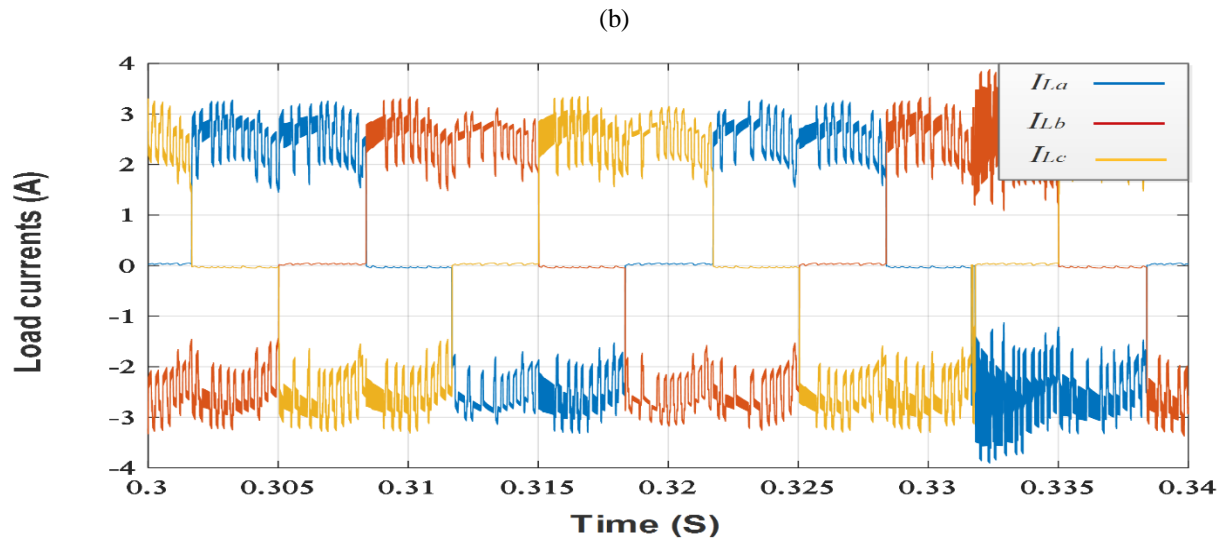
Figure 4.14 Proposed switching algorithm responses of: (a) load voltages, (b) load currents for non-linear load

Figure 4.13 and 4.14 show the load voltages and currents for non-linear load using the proposed FS-MPVC and switching algorithm, respectively. During this test, the controllers have succeeded in providing the same performances as for a linear loads, where sinusoidal and lowly distorted load voltage waveforms are obtained using both techniques even though the high distortion of the load currents.

4.4.4 Robustness tests

To evaluate the robustness of the proposed voltage controllers, two test has been carried out. The first one is a sudden change in the load, whereas the second one is a change in voltage reference.

4.4.4.1 Sudden load variation

In the first test, the load resistance varies from 44Ω to 22Ω in 0.3s, then, in 0.7s it takes back its original value.

Figures 4.15 and 4.16 show the responses of load voltages, and load currents using FS-MPVC and the proposed switching algorithm, respectively. The obtained results demonstrate the robustness of the controller against sudden load change. The load currents vary rapidly at the instant of load variation to keep the voltages at their references, where no variation can be observed at that instant.

(a)

(b)
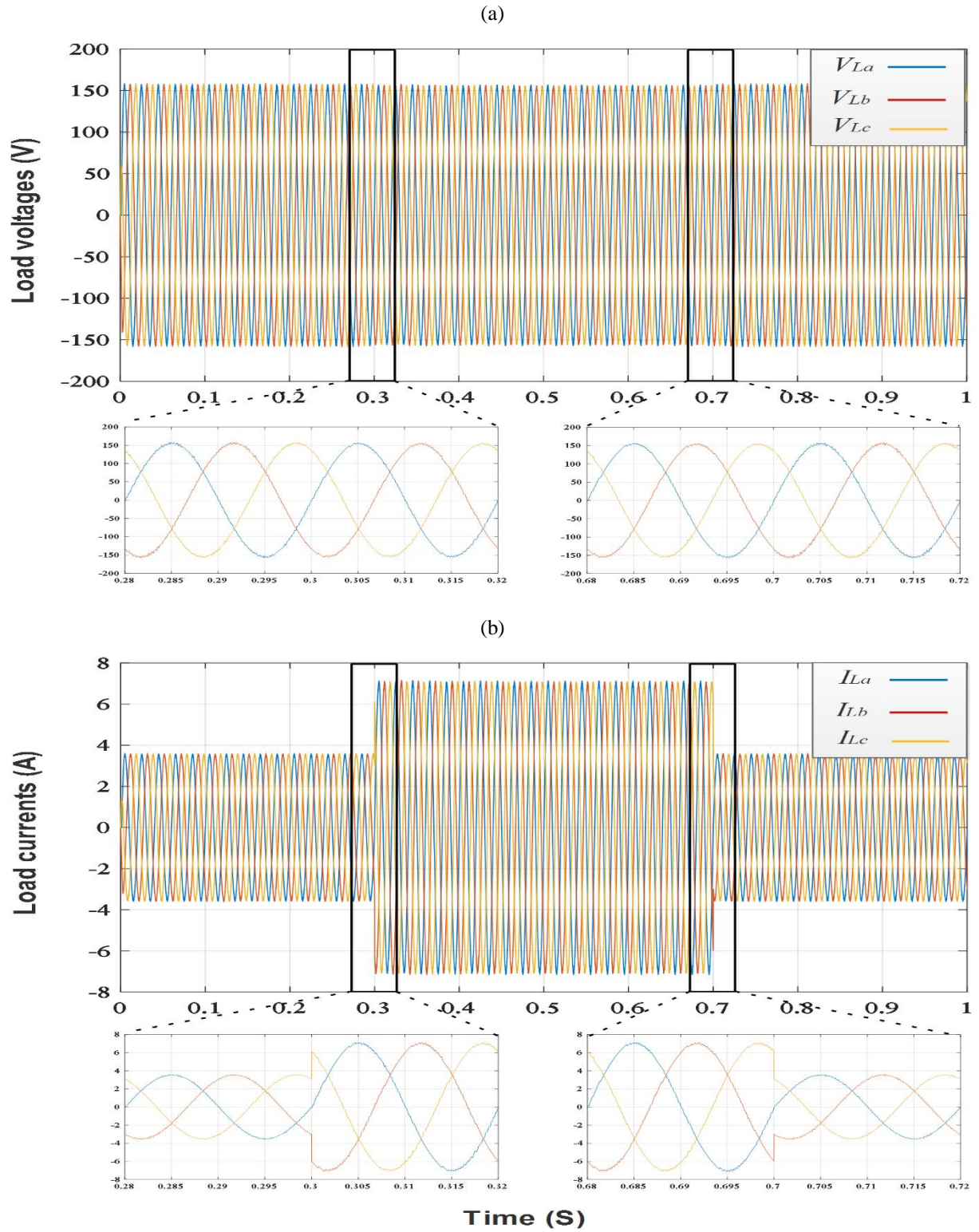
Figure 4.15 FS-MPVC responses of: (a) load voltages, (b) load currents for sudden load change

(a)

(b)
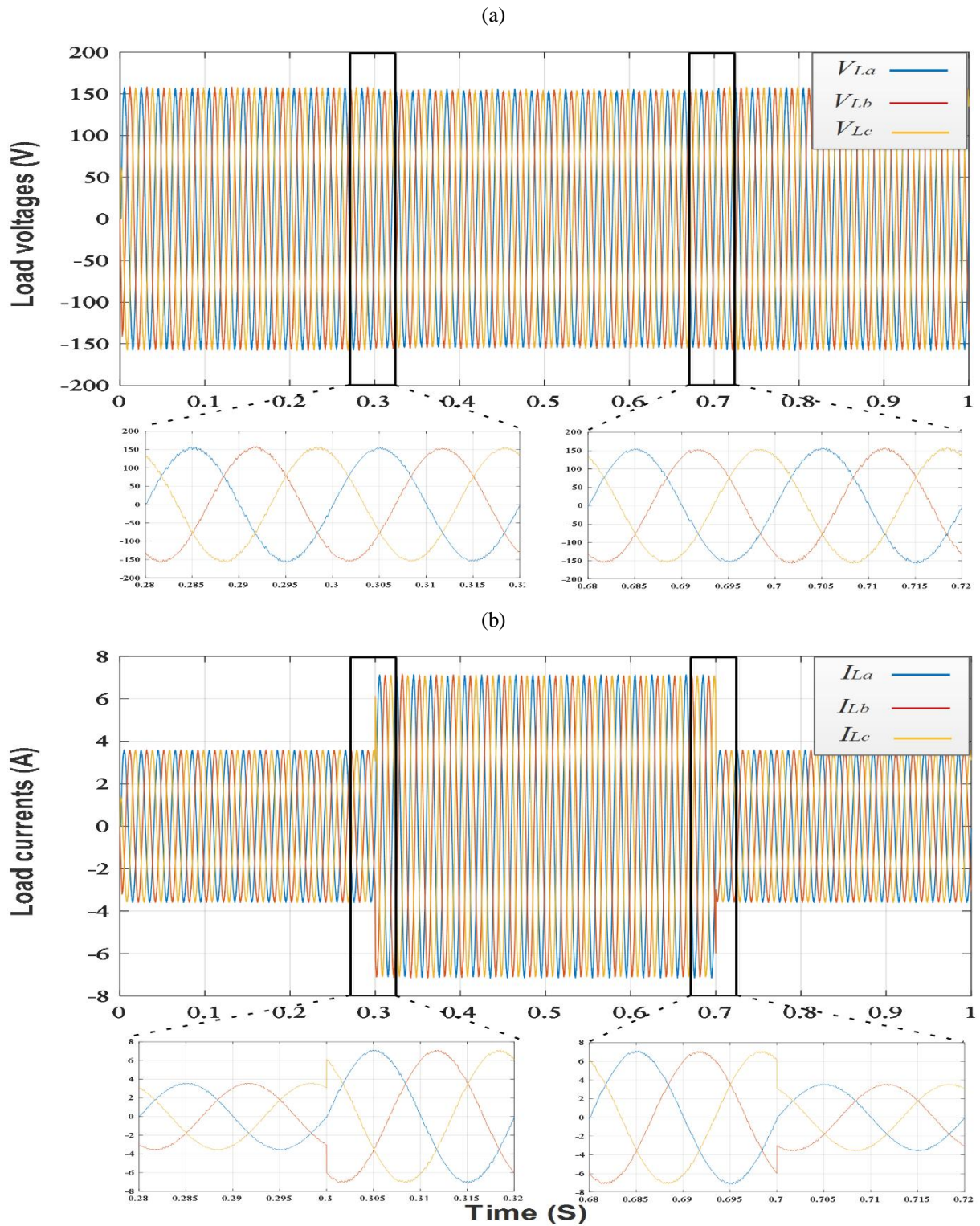
Figure 4.16 Proposed switching algorithm responses of: (a) load voltages, (b) load currents for sudden load change

4.4.4.2 Sudden reference voltage variation

In this second test, a voltage reference variation is carried out. The reference varies from 110 V_{RMS} to 60 V_{RMS} in 0.3s and from 60 V_{RMS} to 110 V_{RMS} in 0.7s.

(a)

(b)
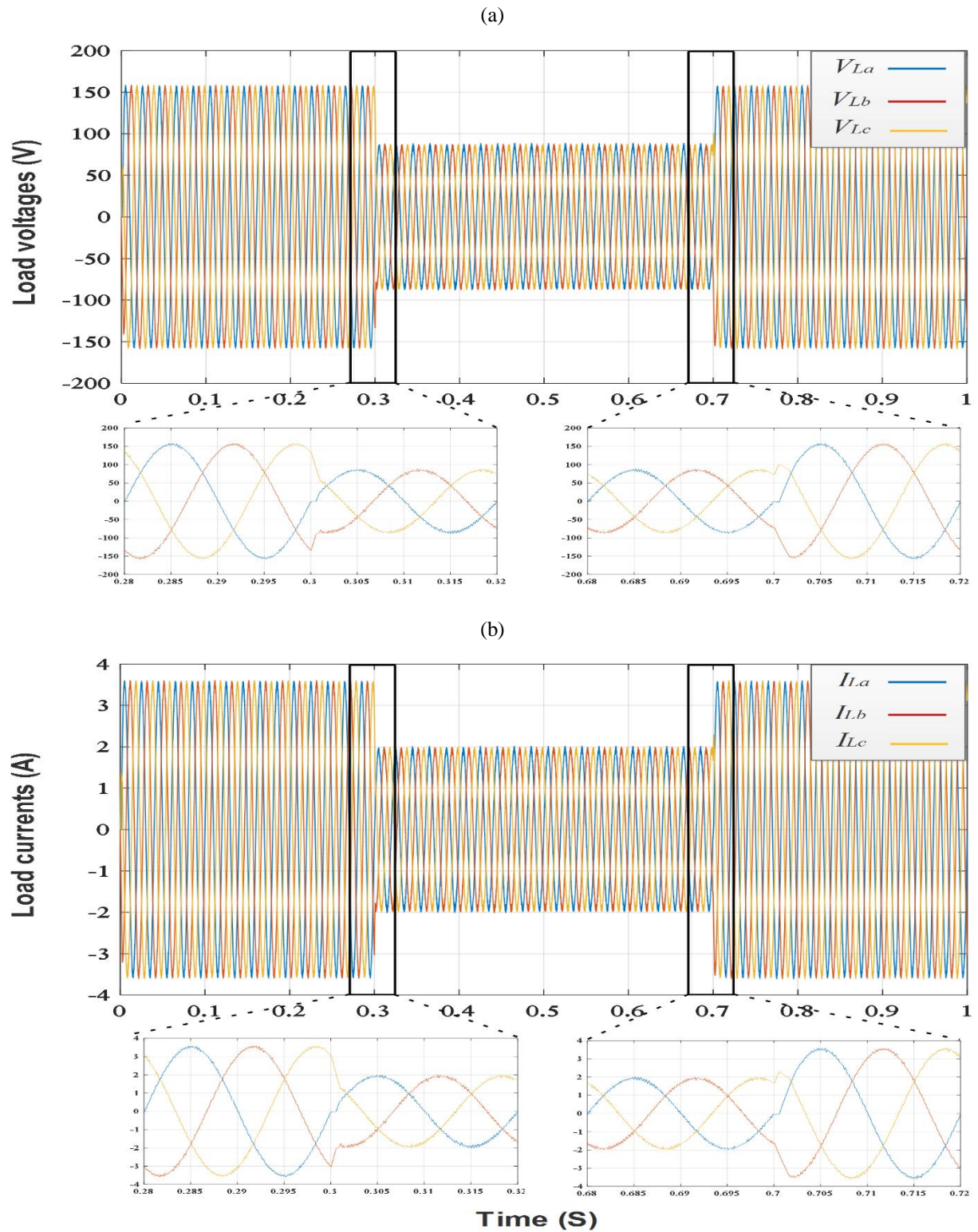
Figure 4.17 FS-MPVC responses of: (a) load voltages, (b) load currents for sudden load change

(a)

(b)
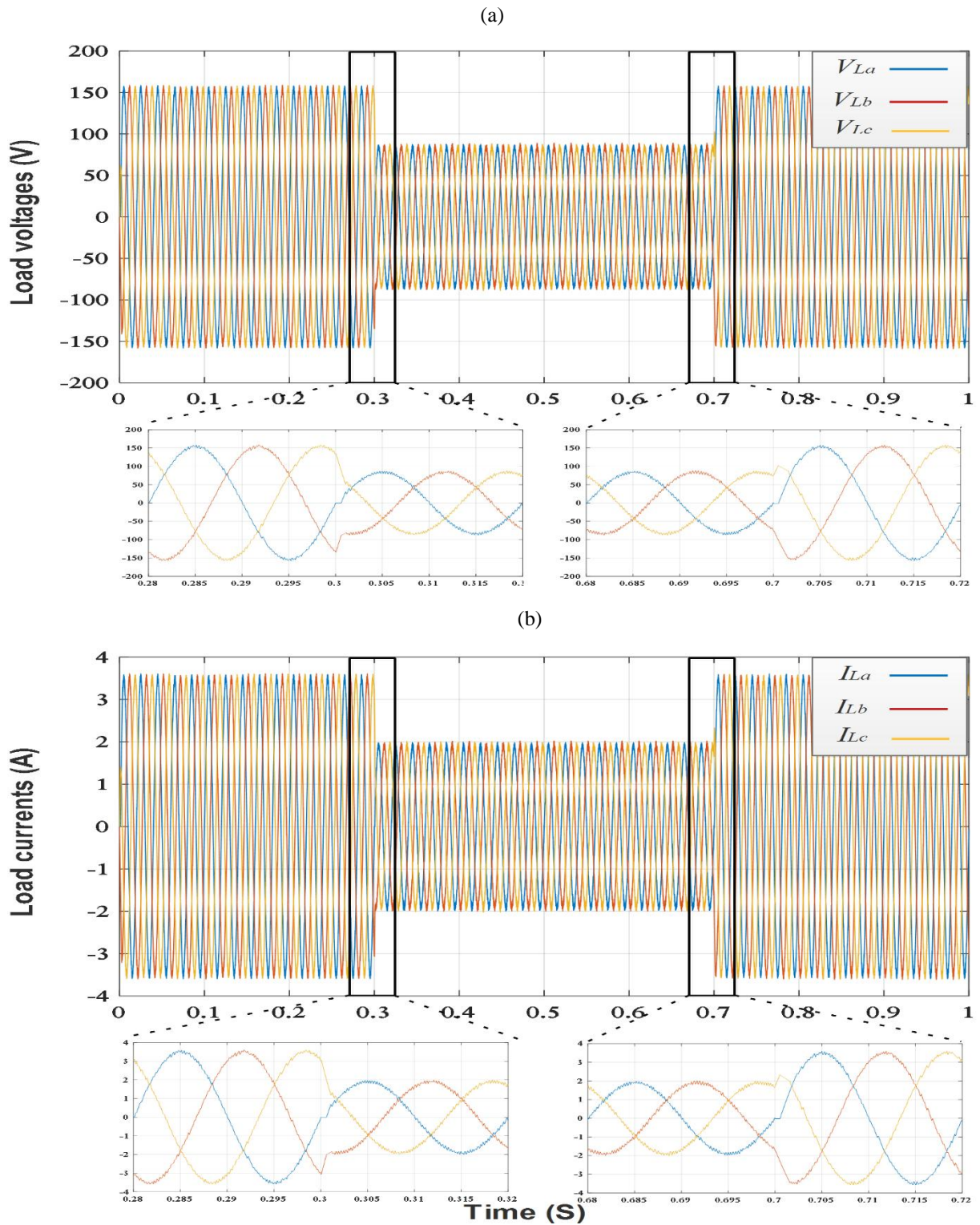
Figure 4.18 Proposed switching algorithm responses of: (a) load voltages, (b) load currents for sudden load change

The obtained results demonstrate the fast dynamics of the proposed voltage control strategies. It is obvious that the load voltages track their references rapidly while keeping the same quality of waveforms.

4.4.5 Comparative study

Table 4.1 gives a comparative evaluation of available and proposed voltage controlled stand-alone CSIs. The comparison involves complexity of the controllers, type of used regulators, type of modulator, and quality of voltage waveform and computed THD if available.

Table 4.1 Comparison between available and proposed voltage controlled stand-alone CSIs

	Complexity	**Regulation loops**	**Modulators**	**Waveform quality**
Strategy of [4.6]	High	PI/PR controllers	VSI to CSI state map	Moderate
Strategy of [4.7]	High	Bang-bang controllers	No	Bad (4.7%)
Strategy of [4.8]	Very high	PI regulator	PWM (bi-logic/tri-logic)	Moderate
Strategy of [4.8]	High	PR controllers	SVM	Good (1.9%)
Strategy of [4.9]	Very high	PI regulator	VSI to CSI state map	Moderate
Proposed FS-MPVC	Moderate	No	No	Best (1.42%)
Proposed switching algorithm	Low	No	No	Very good (1.66%)

From the table, it is clear that the proposed techniques provide the best waveform quality without the use of regulation loops and modulators, which results in low complexity of the control techniques as compared with those in literature.

4.5 Experimental results

The performance of the proposed controllers have been verified experimentally using a CSI prototype (Appendix B) controlled with a DSP of Texas instruments (TI-F28M36) for resistive and resistive-inductive loads using the same parameters as those used for numerical simulations. The controllers have been implemented with sampling time of 40μs.

4.5.1 Resistive load

(a)   (b)
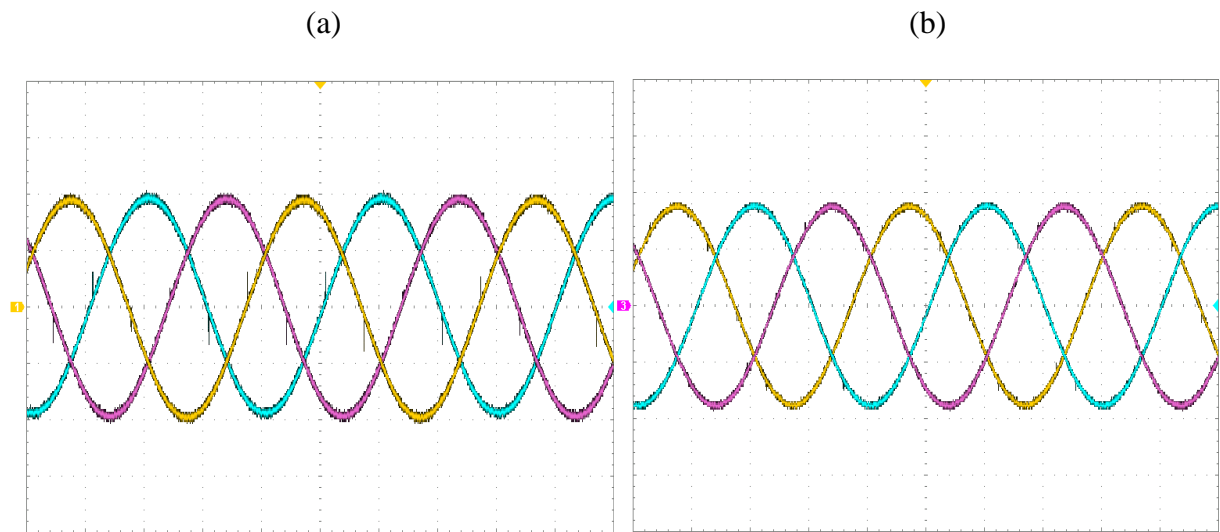
Figure 4.19 Obtained FS-MPVC experimental results for resistive load: (a) Load voltages (80V/div), (b) Load currents (2A/div)

(a)   (b)
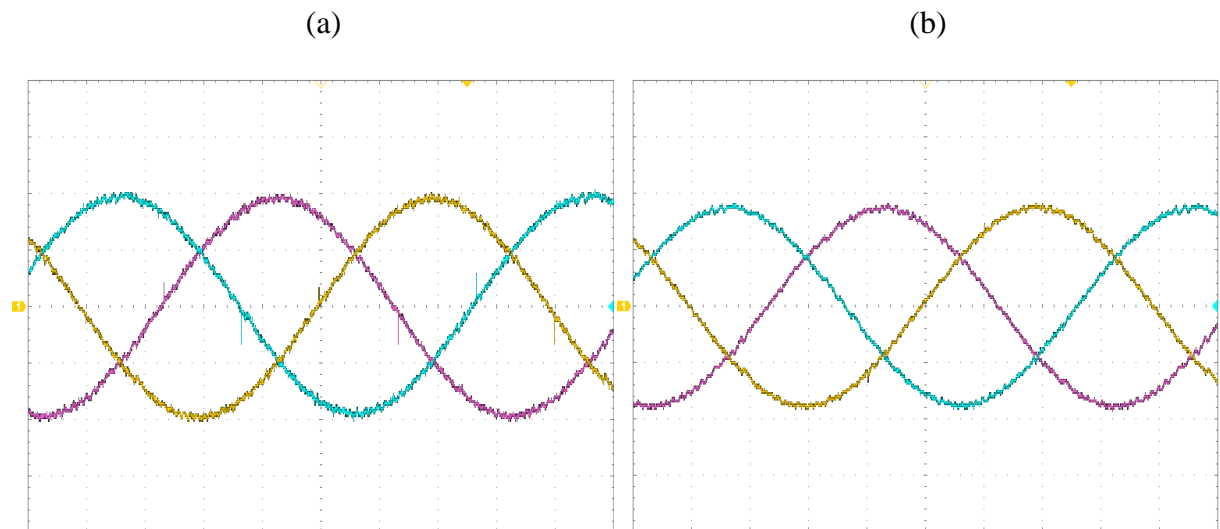
Figure 4.20 Obtained switching algorithm experimental results for resistive load: (a) Load voltages (80V/div), (b) Load currents (2A/div)

4.4.1 Resistive-inductive load

(a)   (b)
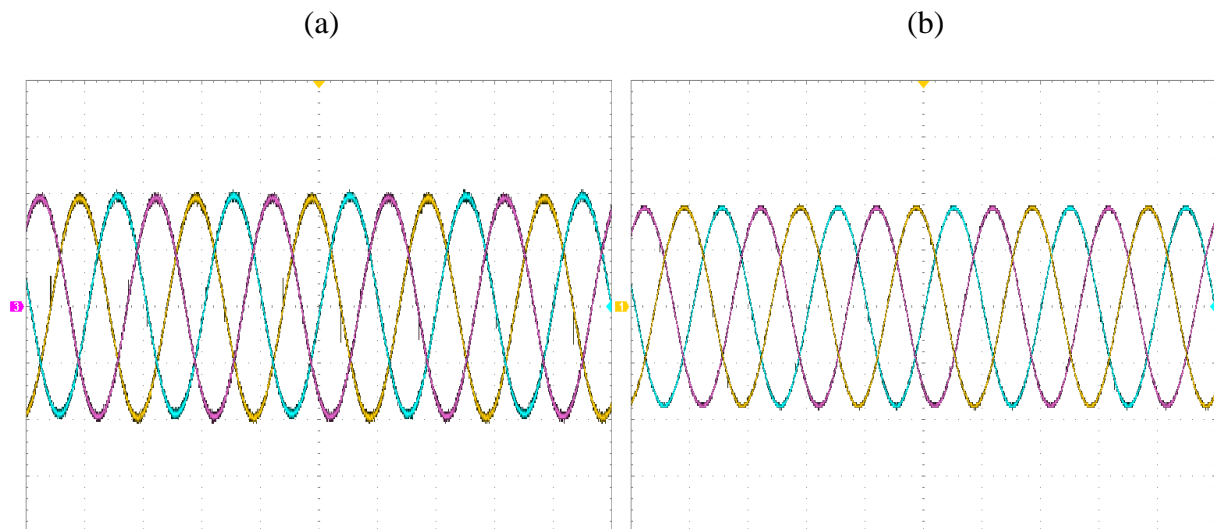

Figure 4.21 Obtained FS-MPVC experimental results for resistive-inductive load: (a) Load voltages (80V/div), (b) Load currents (2A/div)

(a)   (b)
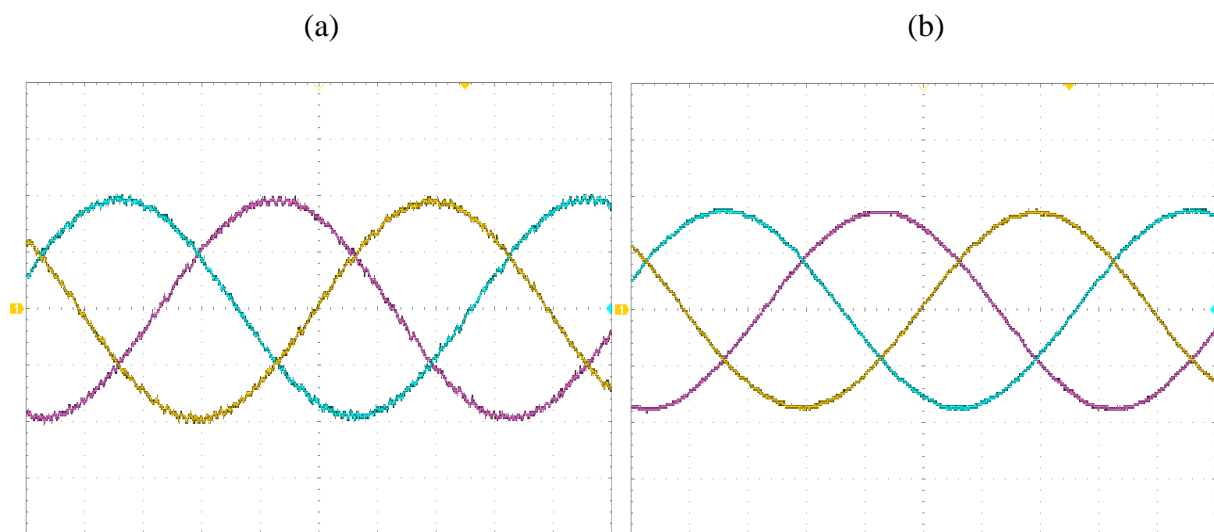
Figure 4.22 Obtained switching algorithm experimental results for resistive-inductive load: (a) Load voltages (80V/div), (b) Load currents (2A/div)

The obtained experimental voltage, and current waveforms are sinusoidal, and lowly distorted for both load types. However, load currents for *RL* type load are smoother than those obtained with a resistive load, this is due to the presence of the inductor. In the other hand. It can be noticed also that FS-MPVC performance is slightly better than this of the switching algorithm. Moreover, the obtained experimental results are in agreement with the previously obtained simulation results, which demonstrates the effectiveness and the feasibility of the proposed controllers for the stand-alone CSI system.

4.6 Conclusion

Stand-alone CSI systems require voltage control, since the majority of loads need a defined voltage for their operation. This chapter has proposed new voltage control strategies for stand-alone CSIs. The developed techniques ensure a fast and accurate voltage control independently of the connected loads. Moreover, they are able to perform without neither regulations loops, nor modulators. These features allow the system to be robust, stable, and accurate. The first technique is based on the theory of FS-MPC, where the prediction model is derived for CSI including its capacitor filter, whereas a cost function is designed in order to minimize the error of the output load voltages. The second proposed technique is a switching algorithm that have as inputs the three phase voltage errors. The proposed technique correct at each sampling instant two out of three voltage errors, whereas the third one is corrected only when it will be dominating against other phase errors. It has been described how the algorithm selects the phases to be corrected and how to the correction is achieved. Numerical simulations using Matlab/Simulink® for the proposed techniques have been carried out for different loads and during different robustness tests. In the last part of this chapter, experimental results of a stand-alone CSI for the two proposed techniques using a low power CSI prototype controlled by a DSP were exposed. The obtained simulation and experimental results are in agreement, and demonstrate the effectiveness, robustness, and feasibility of the proposed techniques.

References

[4.1]   J. Rodriguez, F. Cortes, Predictive Control of Power Converters and AC Drives, John Wiley & Sons, Ltd, 2012.

[4.2]   V. Yaramasu, B. Wu, *Model Predictive Control of Wind energy Conversion Systems and AC Drives*, John Wiley & Sons, Ltd, 2017.

[4.3]   V. Yaramasu, et al., "Model Predictive Approach for a Simple and Effective Load Voltage Control of Four-leg Inverter with an Output LC Filter," *IEEE Trans. on Industrial electronics*, Vol. 61, No. 10, Oct. 2014, pp. 5259–5270

[4.4]   M. Rivera, et al. , "Predictive Current Control in a Current Source Inverter Operating with Low Switching Frequency," *in proc. Inter. Conf. Power eng.*, Turkey, 2013, pp. 1–6

[4.5]   P. Cortes, et al., "Model Predictive Control of an Inverter With Output LC Filter for UPS Applications," *IEEE Trans. Indus. Elec.*, Vol 56, No 6, 2009, pp. 1875–1883.

[4.6]   D. N. Zmood, D. G. Holmes, "Improved Voltage Regulation for Current-Source Inverters," *IEEE Trans. Indus. App.*, Vol 37, No 4, 2001, pp. 1028–1036.

[4.7]   D. V. D. Colli, P. Cancelliere, F. Marignetti, R. Di Stefano, "Voltage Control of Current Source Inverters," *IEEE Trans. on Energy Conversion*, Vol. 21, No. 2, Jun. 2006, pp. 451–458

[4.8]   H. Kömürcügil, O. Kükrer, "Control Strategy for Three-Phase Current-Source Inverters Based on Lyapunov's Direct Method," *in Proc. IEEE Symposium on Industrial Electronics*, UK, 2008.

[4.9]   L. Tan, Y. Li, C. Liu, P. Wang, Z. Li, "Advanced Voltage Control Methods for Current Source Inverters with Linear and Nonlinear Loads," *in Proc. IEEE Symposium on Industrial Electronics*, Korea, 2009.

[4.10]   S. A. S. Grogan, D. G. Holmes, B. P. McGrath, "High Performance Voltage Regulation of Current Source Inverters," *IEEE Trans. on Power Electronics*, Vol. 26, No. 9, Sep. 2011, pp. 2439–2448

Chapter 5

Single-stage grid connected photovoltaic current source inverter

5.1 Introduction

This chapter develops two control techniques for single-stage configuration of grid-connected PV system based on CSI. The proposed strategies are both based on FS-MPC theory. The first technique named finite-set model predictive voltage oriented control (FS-MPVOC) is achieved by combining voltage oriented control (VOC) technique along with FS-MPVC reported in the previous chapter. FS-MPVOC controls the grid injected powers indirectly via the control of the currents in the synchronously reference dq-frame through two regulation loops, where a grid synchronization angle is required for the frame transformations. The second proposed method is called finite-set model predictive direct power control (FS-MPDPC). It is a combination of FS-MPC and DPC strategies. FS-MPDPC contrarily to FS-MPVOC ensures a direct, natural decoupled control of the powers exchanged with the grid without a need to grid synchronization method. In order to harvest the maximum power from the PV array, a P&O based MPPT algorithm is chosen due to its simplicity and good performance. The P&O algorithm is responsible for generating the reference of the PV current, which is then adjusted using a PI regulator that provides the reference of the d-axis current or the active power for the FS-MPVOC or FS-MPDPC, respectively. A SMO is proposed for the grid-side variables estimation in order to reduce system's cost and complexity and avoid sensors noise. Furthermore, due to presence of a CL filter at the output of CSI, resonance may occur. Therefore, an active damping method for each of the proposed control strategies is introduced instead of passive damping method. Active damping as compared with the conventional passive damping improves the system performance and efficiency, and enhances the quality of the injected power. Simulation results and real-time implementation results are presented and discussed in the last part of this chapter.

5.2 Maximum power point tracker (MPPT)

The characteristics curves of PV arrays are highly non-linear and are affected by irradiance and temperature variations [5.1],[5.2]. Therefore, a MPPT is required to cater these issues and ensure that the PV system operates all the time at the MPP. Many MPPT techniques have been proposed in the literature, such as P&O, incremental conductance, parasitic capacitance, constant voltage, ripple correlation control, constant current, fuzzy logic controller, and artificial intelligence techniques. These techniques vary in simplicity, accuracy, time response, popularity, cost, and other technical aspects [5.2]. Among the aforementioned techniques, the most widely-used MPPT is P&O due to its good performance, low cost, and simplicity of implementation [5.1],[5.2]. For this reason it has been chosen to be the MPPT in this work.
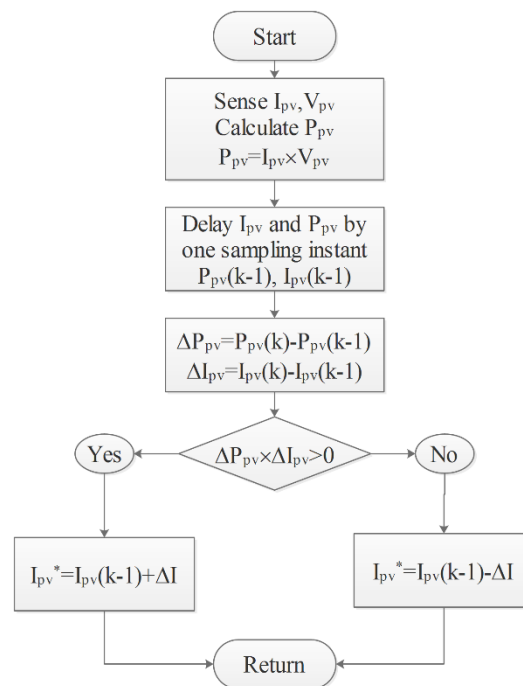
Figure 5.1 Flowchart of P&O algorithm

P&O algorithm requires only measurements of PV voltage V_{pv}, and PV current I_{pv}. As its name indicates, the P&O method works by perturbing V_{pv} or I_{pv} and observing the impact of this change on the output power of the PV array P_{pv}. At each cycle V_{pv} and I_{pv} are measured to calculate $P_{pv}(k)$. The value of $P_{pv}(k)$ is compared to the value $P_{pv}(k-1)$ calculated at the previous cycle. If the output power has increased, I_{pv} is adjusted further in the same direction as in the previous cycle. If the output power has decreased, I_{pv} is perturbed in the opposite direction of the previous cycle. Thus, I_{pv} is perturbed at every MPPT cycle. When the maximum power point is reached, I_{pv} oscillates around the optimal value. This causes a power loss that increases with the increase of perturbation step size. If this step width is large, the MPPT algorithm

responds quickly to sudden changes in operating condition but with high oscillations around the MPP. On the other hand, if the step size is small the losses under stable or slowly changing conditions will be lower but the system will not be able to respond quickly to rapid changes in temperature or irradiance [5.1],[5.2]. The flowchart of P&O algorithm is depicted in Figure 5.1

5.3 Sliding mode observer (SMO)

SMOs are mathematical systems that allow the reconstruction of the real system state variables. SMO observers are used for technical and economic reasons, by avoiding the noise of sensors, and reducing the system's cost and complexity [5.3]. In this work, a SMO is proposed in order to estimate the grid-side variables. Using the system's model in the stationary reference frame previously reported in Chapter 3, and adding two extra state variables which are the grid voltages yields to this new model

$$\frac{dI_{g\alpha}}{dt} = -\frac{R_f}{L_f} I_{g\alpha} + \frac{1}{L_f} V_{c\alpha} - \frac{1}{L_f} V_{g\alpha} \tag{1}$$

$$\frac{dI_{g\beta}}{dt} = -\frac{R_f}{L_f} I_{g\beta} + \frac{1}{L_f} V_{c\beta} - \frac{1}{L_f} V_{g\beta} \tag{2}$$

$$\frac{dV_{c\alpha}}{dt} = \frac{1}{C_f} I_{o\alpha} - \frac{1}{C_f} I_{g\alpha} \tag{3}$$

$$\frac{dV_{c\beta}}{dt} = \frac{1}{C_f} I_{o\beta} - \frac{1}{C_f} I_{g\beta} \tag{4}$$

$$\frac{dV_{g\alpha}}{dt} = -\omega V_{g\beta} \tag{5}$$

$$\frac{dV_{g\beta}}{dt} = \omega V_{g\alpha} \tag{6}$$

Which can be represented by the following state-space model

$$\begin{cases} \dfrac{dX}{dt} = AX + BU \\ Y = CX \end{cases} \tag{7}$$

Where

$$X = \begin{bmatrix} I_{g\alpha} & I_{g\beta} & V_{c\alpha} & V_{c\beta} & V_{g\alpha} & V_{g\beta} \end{bmatrix}^T \tag{8}$$

$$U = \begin{bmatrix} I_{o\alpha} & I_{o\beta} \end{bmatrix} \tag{9}$$

$$A = \begin{bmatrix} -\dfrac{R_f}{L_f} & 0 & \dfrac{1}{L_f} & 0 & -\dfrac{1}{L_f} & 0 \\ 0 & -\dfrac{R_f}{L_f} & 0 & \dfrac{1}{L_f} & 0 & -\dfrac{1}{L_f} \\ -\dfrac{1}{C_f} & 0 & 0 & 0 & 0 & 0 \\ 0 & -\dfrac{1}{C_f} & 0 & 0 & 0 & 0 \\ 0 & 0 & 0 & 0 & 0 & -\omega \\ 0 & 0 & 0 & 0 & \omega & 0 \end{bmatrix} \tag{10}$$

$$B = \begin{bmatrix} 0 & 0 \\ 0 & 0 \\ \dfrac{1}{C_f} & 0 \\ 0 & \dfrac{1}{C_f} \\ 0 & 0 \\ 0 & 0 \end{bmatrix} \tag{11}$$

$$C = \begin{bmatrix} 1 & 0 & 0 & 0 & 0 & 0 \\ 0 & 1 & 0 & 0 & 0 & 0 \end{bmatrix} \tag{12}$$

Which leads to the following observability matrix

$$O = \begin{bmatrix} C & CA & CA^2 & CA^3 & CA^4 & CA^5 \end{bmatrix} \tag{13}$$

Moreover the controllability matrix is given by

$$\Gamma = \begin{bmatrix} B & AB & A^2B & A^3B & A^4B & A^5B \end{bmatrix} \tag{14}$$

Matrice O is of full-rank, (i.e. *rank{O}= 6*), so that the system is observable and can be observed only using the measured current I_g.

Unlike other state observers, in SMOs, instead of feeding back the output error between the observer and the system linearly, the output error is fed back via a discontinuous switched signal [5.3].

Thus, the proposed grid-side SMO can be defined as follows

$$\frac{dI_{g\alpha}}{dt} = -\frac{R_f}{L_f}I_{g\alpha} + \frac{1}{L_f}V_{c\alpha} - \frac{1}{L_f}V_{g\alpha} + K_1.Sign(\widehat{I}_{g\alpha} - I_{g\alpha}) \tag{15}$$

$$\frac{dI_{g\beta}}{dt} = -\frac{R_f}{L_f}I_{g\beta} + \frac{1}{L_f}V_{c\beta} - \frac{1}{L_f}V_{g\beta} + K_1^{'}.Sign(\widehat{I}_{g\beta} - I_{g\beta}) \tag{16}$$

$$\frac{dV_{c\alpha}}{dt} = \frac{1}{C_f}I_{o\alpha} - \frac{1}{C_f}I_{g\alpha} + K_2.Sign(\widehat{I}_{g\alpha} - I_{g\alpha}) \tag{17}$$

$$\frac{dV_{c\alpha}}{dt} = \frac{1}{C_f}I_{o\beta} - \frac{1}{C_f}I_{g\beta} + K_2.Sign(\widehat{I}_{g\beta} - I_{g\beta}) \tag{18}$$

$$\frac{dV_{g\alpha}}{dt} = -\omega V_{g\beta} + K_3.Sign(\widehat{I}_{g\alpha} - I_{g\alpha}) \tag{19}$$

$$\frac{dV_{g\beta}}{dt} = \omega V_{g\alpha} + K_3^{'}.Sign(\widehat{I}_{g\beta} - I_{g\beta}) \tag{20}$$

Where K_1, $K_1^{'}$, K_2, $K_2^{'}$, K_3, $K_3^{'}$, are the SMO gains.

In this SMO, it is obvious that sliding surface S is constructed using the error between the actual and observed grid currents in $\alpha\beta$ reference frame.

Furthermore, in order to reduce the undesirable problem of chattering, a saturation function is used instead of the *Sign* function [5.3]. The saturation function is defined by

$$Sat(S) = \begin{cases} 1 & if & S > \Delta \\ S/\Delta & if & -\Delta < S < \Delta \\ -1 & if & S < \Delta \end{cases} \tag{21}$$

Where Δ is a tuning parameter.
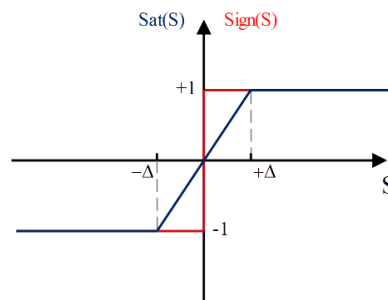
Figure 5.2 SMO sign and saturation functions

5.4 Finite-set model predictive control

FS-MPC is one the most appropriate techniques for the control of converters, due to its good performance, and simplicity of implementation [5.4],[5.5]. In this work two controllers based on FS-MPC theory are proposed for the control of photovoltaic grid connected CSI. The first employs VOC strategy, whereas the second one employs DPC technique.

5.4.1 FS-MPVC based voltage oriented control (FS-MPVOC)

Figure 5.3 shows the block diagram of the proposed FS-MPVOC. The PV voltage and current are measured and inputted to the MPPT block that generates PV current reference. The PV current is then adjusted using a PI regulator which generates in turn the *d*-axis reference for VOC, whereas the *q*-axis current reference is set according to the demand of reactive power. Afterward, the *dq* currents are controlled using two PI regulation loops, and decoupled via feed-forward method. The resulting *dq* voltage references are modified using the active damping block and fed directly to FS-MPVC controller (FS-MPVC explained in details in chapter 4).
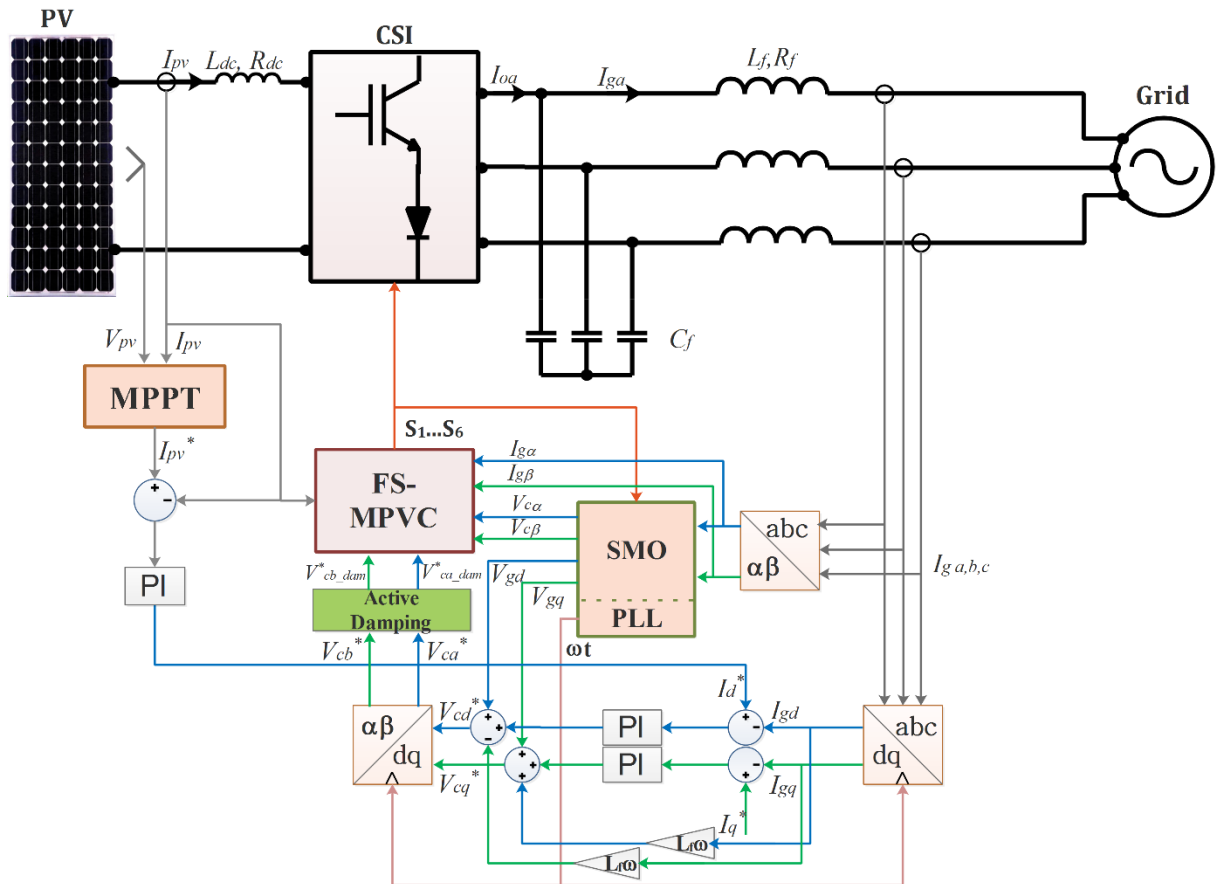
Figure 5.3 Block diagram of proposed FS-MPVC control scheme

5.4.1.1 DC-link current control

Assuming that the switching losses of the inverter are negligible, the DC-side power of the inverter, P_{dc}, is equal to the active power delivered on the AC-side, P_{ac}. Since the d-axis current is an image of the active power, the DC link current can be controlled by acting on this current reference which is generated using a simple PI regulator. The following figure show the DC link regulation loop, where, $G(s)$ is the system's AC d-axis current to DC current transfer function that can be derived using small-signal modeling as in [5.6].
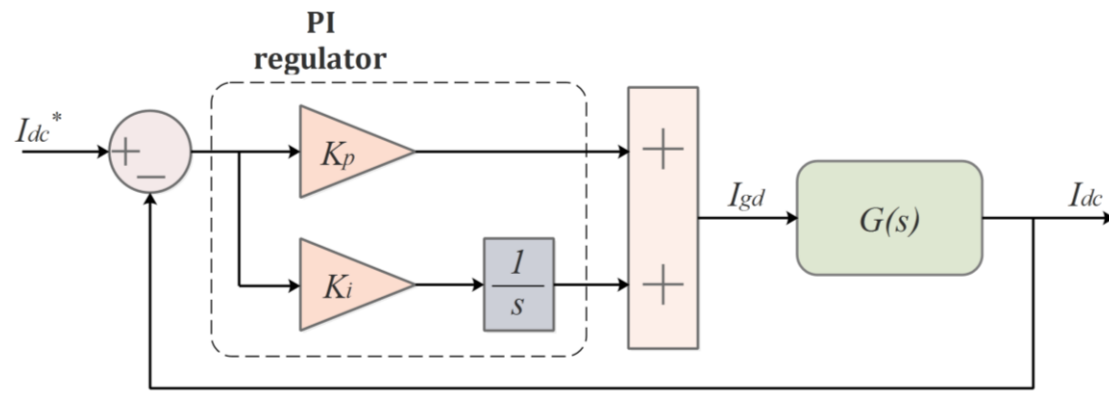
Figure 5.4 DC link PI regulation loop.

5.4.1.2 Voltage oriented control (VOC)

Typically the VOC is based on a dq-frame rotating at ω speed and oriented such that the d-axis is aligned on the grid voltage vector [5.7],[5.8] (Figure 5.5)
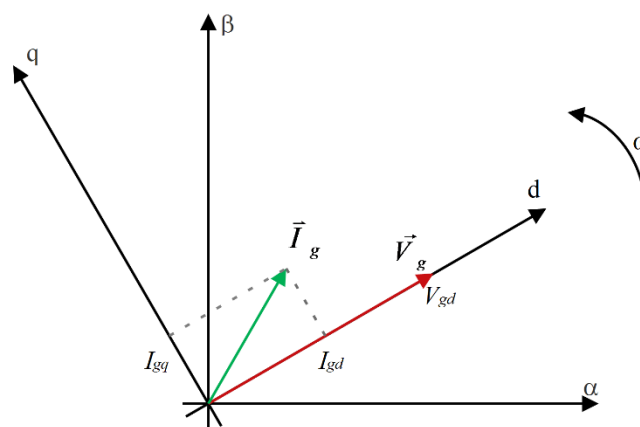
Figure 5.5 Orientation of voltage vector on the d-axis.

The dynamics of the dq-frame grid currents are given by the following equations

$$\frac{dI_{gd}}{dt} = -\frac{R_f}{L_f} I_{gd} + \omega I_{gq} + \frac{1}{L_f} V_{cd} - \frac{1}{L_f} V_{gd} \tag{22}$$

$$\frac{dI_{gq}}{dt} = -\frac{R_f}{L_f} I_{gq} - \omega I_{gd} + \frac{1}{L_f} V_{cq} - \frac{1}{L_f} V_{gq} \tag{23}$$

It can be noted from (22) and (23) that there exists a cross-coupling between the d and q components, this can affect the dynamic performance of the regulators. Therefore, it is very important to decouple the two axis for better performances. This can be accomplished with feed-forward decoupling method [5.7],[5.8]. Assuming that

$$V_{rd} = V_{cd} - V_{gd} + \omega I_{gd} \tag{24}$$

$$V_{rq} = V_{cq} - V_{gq} - \omega I_{gq} \tag{25}$$

Then, the equations (22) and (23) are transformed to

$$\frac{dI_{gd}}{dt} = -\frac{R_f}{L_f} I_{gd} + \frac{1}{L_f} V_{rd} \tag{26}$$

$$\frac{dI_{gq}}{dt} = -\frac{R_f}{L_f} I_{gq} + \frac{1}{L_f} V_{rq} \tag{27}$$

The cross-coupling variables are eliminated in the aforementioned equations. Hence, the currents I_d and I_q can be controlled independently by acting upon the capacitor voltages V_{cd} and V_{cq}, respectively.

Furthermore, by using PI type regulators, a fast dynamic response and zero steady-state errors can be achieved. The diagram of the current regulator –which is suitable for both I_d and I_q loops– is shown in Figure 5.6.
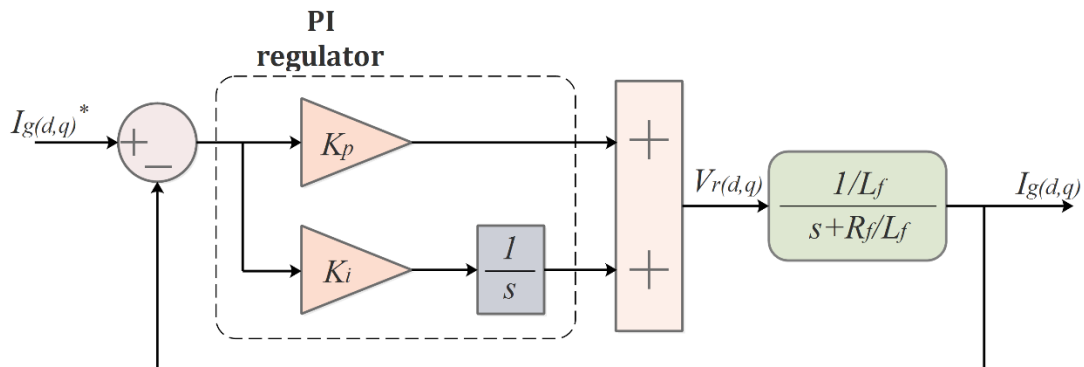
Figure 5.6 Diagram of PI current regulation loops

Moreover, the reactive power in SRF is given by [5.4]-[5.6]

$$Q = \frac{3}{2}\left[I_{gd}V_{gq} - I_{gq}V_{gd}\right] \tag{28}$$

Knowing that $V_{gq}=0$, since the grid voltage vector is aligned on the d-axis of SRF. The reactive power can be written as

$$Q = -\frac{3}{2}V_{gd}I_{gq} \tag{29}$$

Consequently, the reactive power can be controlled by acting upon the q-axis grid current reference, because V_{gd} is constant.

5.4.1.3 Proposed active damping method

The proposed active damping method for FS-MPVOC is achieved by considering a virtual resistor R_{vd1} in series with the capacitor as shown in figure 5.7. Therefore the reference of the capacitor voltage is changed by adding the voltage of this resistor such as
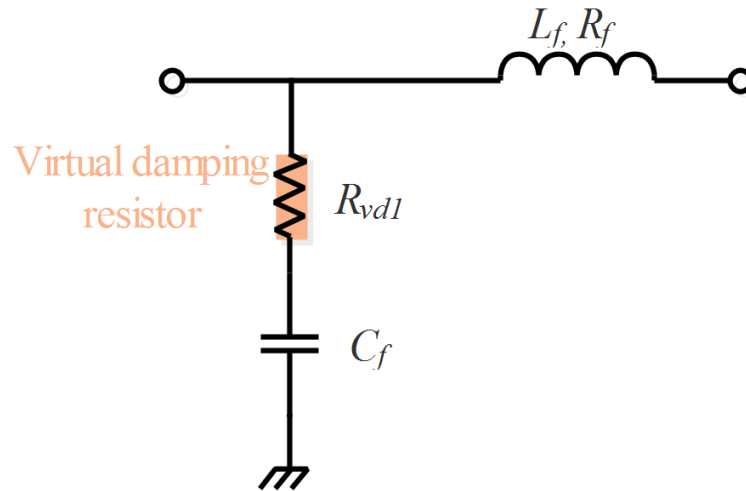
Figure 5.7 Active damping virtual resistor placement.

$$V^*_{c(\alpha,\beta)\_dam} = V^*_{c(\alpha,\beta)} + R_{vd1}I_{c(\alpha,\beta)} \tag{30}$$

Which yields to the new voltage references

$$V^*_{c(\alpha,\beta)\_dam} = V^*_{c(\alpha,\beta)} + R_{vd1}C_f\frac{dV^*_{c(\alpha,\beta)}}{dt} \tag{31}$$
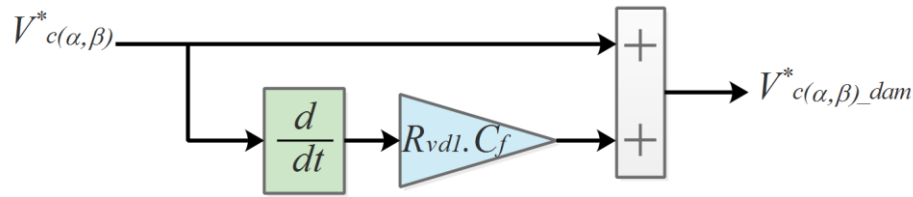
Figure 5.8 Reference modification using active damping for FS-MPVOC

5.4.1.4 Grid synchronization phase locked loop (PLL)

There are two categories of methods for the purpose of synchronization: open-loop methods and close-loop methods. Typical open-loop methods include detecting the zero crossing of the grid voltage and directly filtering the grid voltage. Closed-loop methods introduce a mechanism to make sure that the information obtained is accurate. Typical examples of closed-loop methods include the conventional PLL, which is widely used in single-phase applications, and the synchronously rotating reference frame PLL (SRF-PLL), which is widely used in three-phase applications. PLLs have been adopted as part of the controllers for most of the grid-connected applications nowadays [5.8]. For FS-MPVOC the most common synchronization technique for three phase systems (SRF-PLL) is utilized (Figure 5.9)
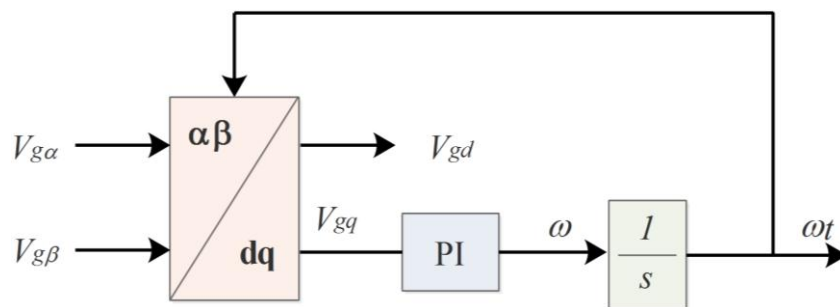
Figure 5.9 Three-phase PLL in the synchronously rotating reference frame (SRF-PLL)

5.4.2 Finite-set model predictive direct power control (FS-MPDPC)

The proposed FS-MPDPC is based on the combination of DPC with MPC techniques. It ensures a decoupled control of active and reactive powers rapidly and accurately. Similarly to the first technique, the MPPT generates the PV current reference, which is controlled by a PI regulator that provides the active power reference for FS-MPDPC controller. However, the active power reference must be modified to actively damp possible resonance. In the other hand, the reactive power reference is adjusted to have unity power factor or according the grid operator demand.
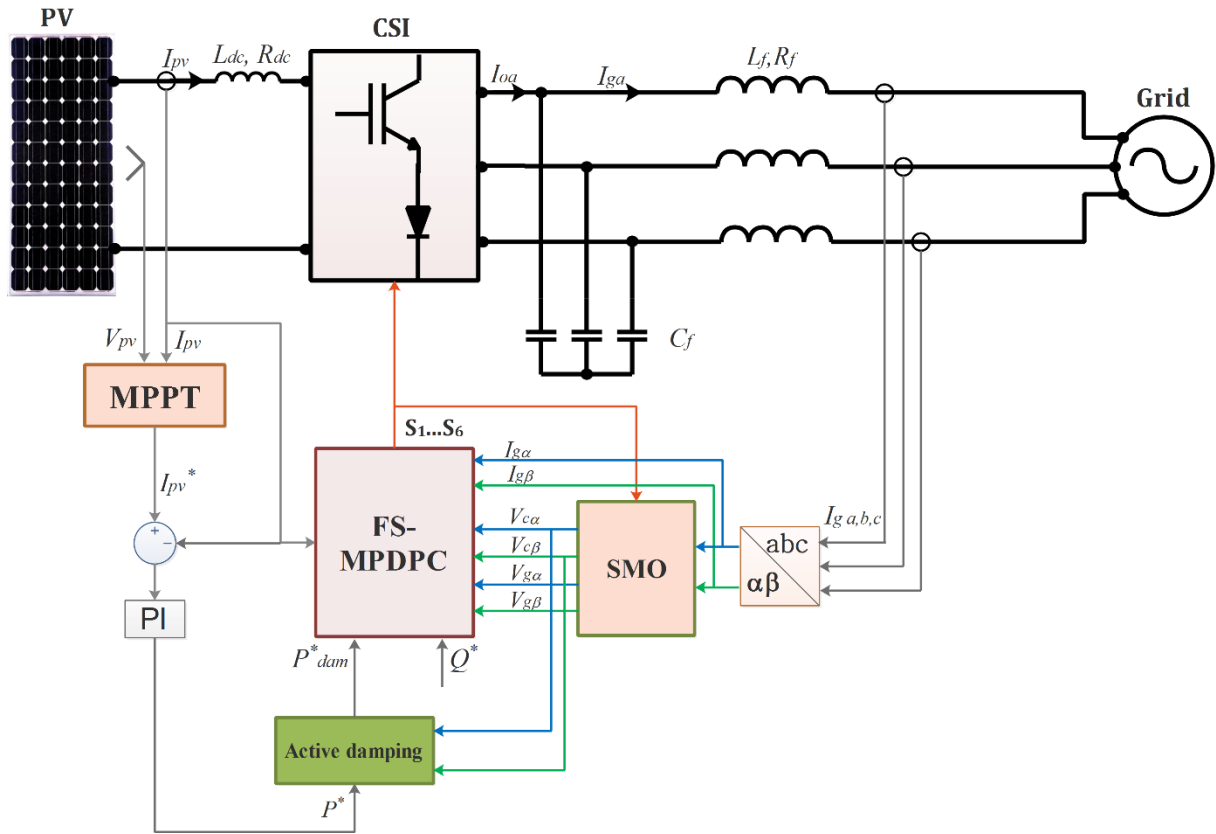
Figure 5.10 Block diagram of the proposed FS-MPDPC control scheme

5.4.2.1 DC-link current control

Assuming the switching losses of the inverter negligible, the DC-side power of the inverter, P_{dc}, is equal to the power delivered on the AC-side, P_{ac}. Therefore, the DC link current can be controlled by acting upon the active power reference which is generated using a simple PI regulator. The diagram of regulation loop is depicted in the following figure. Where $G'(s)$ is system's AC power to DC current transfer function that can be derived using the system's small-signal model [5.6].
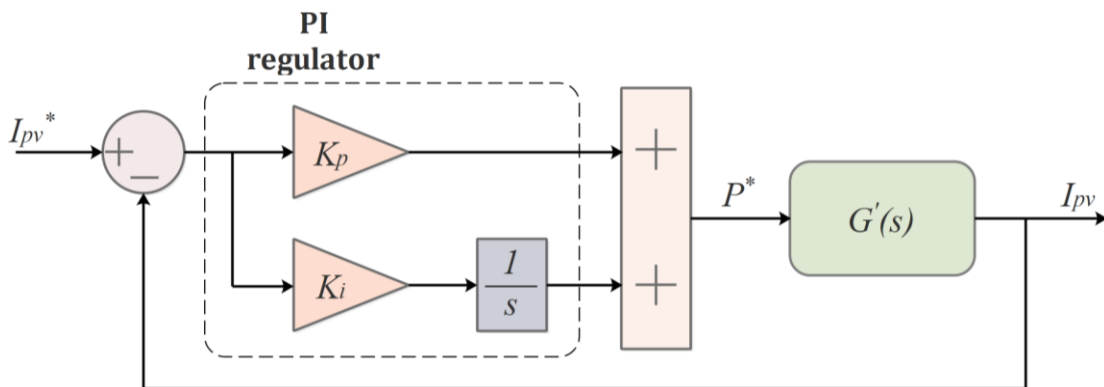
Figure 5.11 Diagram of DC link regulation loop

5.4.2.2 Predictive power controller

A. Prediction model

The instantaneous active and reactive powers of the grid are expressed in terms of the grid currents and voltages, in the stationary reference frame $\alpha\beta$ in the actual sampling instant (k) by

$$P(k) = \frac{3}{2}\left[I_{g\alpha}(k).V_{g\alpha}(k) + I_{g\beta}(k).V_{g\beta}(k)\right] \tag{32}$$

$$Q(k) = \frac{3}{2}\left[I_{g\alpha}(k).V_{g\beta}(k) - I_{g\beta}(k).V_{g\alpha}(k)\right] \tag{33}$$

Thus, the predicted powers in the next sampling instant ($k+1$) can be written as follows

$$P(k+1) = \frac{3}{2}\left[I_{g\alpha}(k+1).V_{g\alpha}(k+1) + I_{g\beta}(k+1).V_{g\beta}(k+1)\right] \tag{34}$$

$$Q(k+1) = \frac{3}{2}\left[I_{g\alpha}(k+1).V_{g\beta}(k+1) - I_{g\beta}(k+1).V_{g\alpha}(k+1)\right] \tag{35}$$

Therefore, to predict the grid exchanged active and reactive powers, it is necessary to predict the grid voltage and current.

For a small sampling time, with respect to the grid fundamental frequency, it can be assumed that $V_g(k+1) \approx V_g(k)$. However, if the sampling time is not small enough to consider the grid voltage as constant between two sampling intervals, the future grid voltage $V_g(k+1)$ can be calculated by compensating the angle of the voltage vector for one sampling time [5.4]

$$V_g(k+1) = V_g e^{j\Delta\theta} \tag{36}$$

Where $\Delta\theta = \omega.T_s$ is the angle advance of the grid voltage vector in one sampling interval.

For the grid currents prediction, the grid-side inverter model in stationary reference frame $\alpha\beta$ - presented previously- is considered

$$\frac{dI_{g(\alpha,\beta)}}{dt} = -\frac{R_f}{L_f}I_{g(\alpha,\beta)} + \frac{1}{L_f}V_{c(\alpha,\beta)} - \frac{1}{L_f}V_{g(\alpha,\beta)} \tag{37}$$

$$\frac{dV_{c(\alpha,\beta)}}{dt} = \frac{1}{C}I_{o(\alpha,\beta)} - \frac{1}{C}I_{g(\alpha,\beta)} \tag{38}$$

The application of the aforementioned forward Euler formula on equation (37) and (38), gives after a mathematical analysis the nine possible predictions for the grid currents in stationary reference frame as

$$I_{g(\alpha,\beta)}[k+1] = \frac{T_s}{R_f T_s + L_f}\left(\frac{T_s}{C_f}I_{o(\alpha,\beta)}[k] + V_{c(\alpha,\beta)}[k] - V_{g(\alpha,\beta)}[k] + \frac{L_f C_f - T_s^2}{CT_s}I_{g(\alpha,\beta)}[k]\right) \qquad (39)$$

B. Cost function optimization

The nine predicted active and reactive powers are compared with their references using a cost function g given by

$$g_j = \left\|P^*[k+1] - P[k+1]\right\| + \left\|Q^*[k+1] - Q[k+1]\right\| \qquad (40)$$

Where j denotes the index of the inverter current vector used in the predictions.

In (40), the future active and reactive power references can be gotten by linear extrapolation as follows [5.4],[5.5]

$$P^*[k+1] = 2P^*[k] - P^*[k-1] \qquad (41)$$

$$Q^*[k+1] = 2Q^*[k] - Q^*[k-1] \qquad (42)$$

However, no extrapolation is needed for small enough sampling time. [5.4],[5.5]

The purpose of the controller is to achieve the smallest error between actual and reference powers. Therefore, the current vector that minimizes the cost function is chosen and applied to the inverter in the whole next sampling period. The predictive controller scheme and algorithm flowchart of proposed FS-MPDPC are shown in Figure 5.12, and Figure 5.13, respectively.
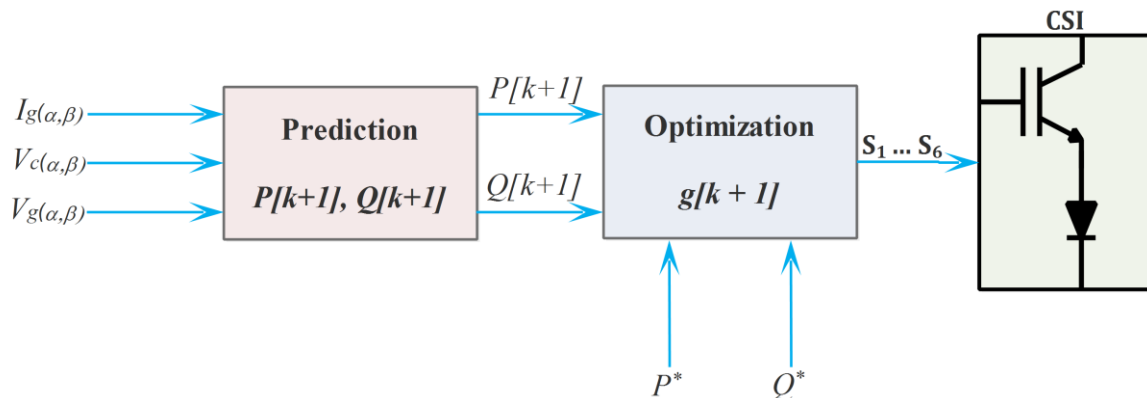
Figure 5.12 FS-MPDPC controller scheme
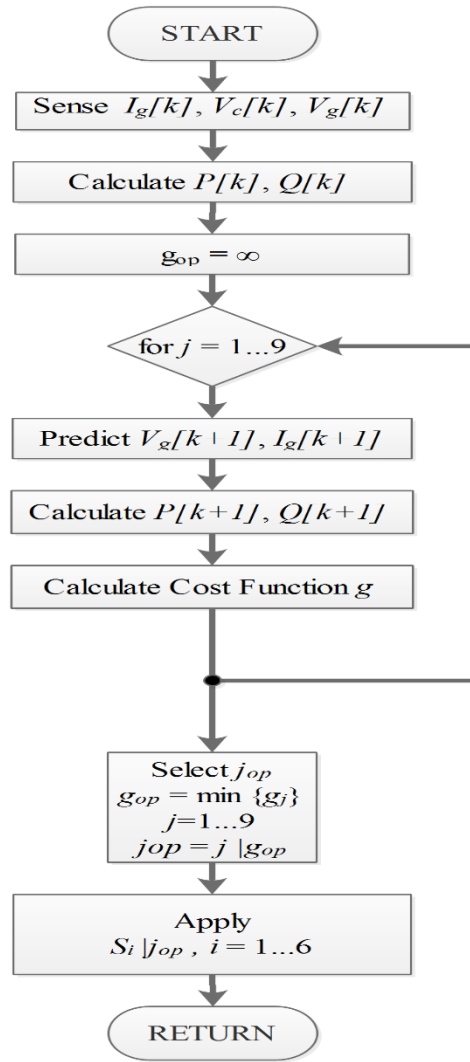
Figure 5.13 FS-MPDPC control algorithm

In Figure 5.13 g_{op} denotes the optimal value of cost function g, and j_{op} is its index.

5.4.2.3 Proposed active damping method

In order to eliminate the resonance phenomena of the *CL* filter of the grid connected CSI, a virtual resistor damping method is proposed for FS-MPDPC. The star-connected resistors R_{vd2} are virtually installed in parallel with the capacitor filter (Figure 5.14). Thus, the power reference is changed by adding the power consumed by the virtual resistors which can be written as follows

$$P_{R_{vd2}} = \frac{3}{2}\left(\frac{V_{c\alpha}^2}{R_{vd2}} + \frac{V_{c\beta}^2}{R_{vd2}} \right) \tag{43}$$

Which yields to the new active power reference

$$P^*_{dam} = P^* + \frac{3}{2}\left(\frac{V^2_{c\alpha}}{R_{vd2}} + \frac{V^2_{c\beta}}{R_{vd2}}\right) \qquad (44)$$
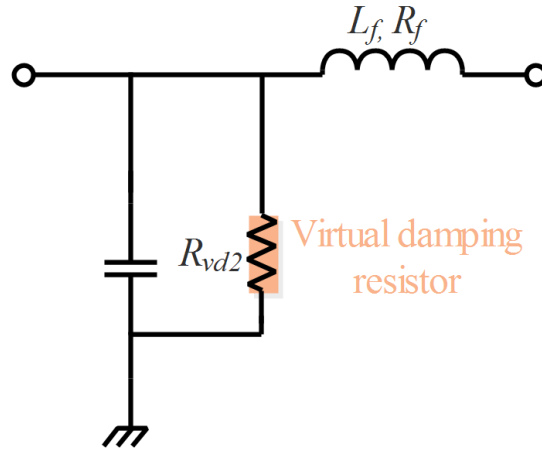
Figure 5.14 Active damping resistor location
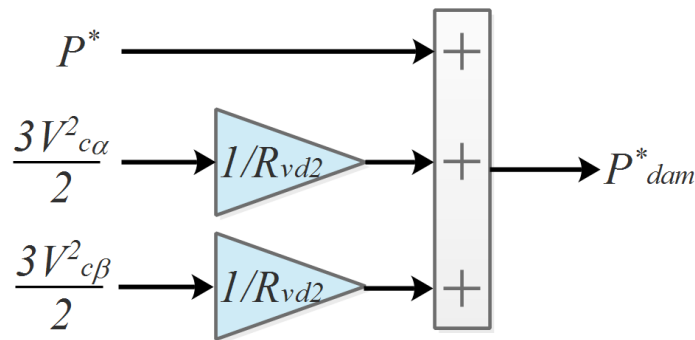
Figure 5.15 FS-MPDPC proposed active damping method

5.5 Simulation results

In order to evaluate the preceding theoretical analysis and validate the performance and the effectiveness of the proposed techniques, the system under study has been built using SimPowerSystems of Matlab/Simulink® software. To reach the desired power level, twelve PV strings are connected in parallel, while each PV string is a combination of three series connected PV modules (which parameters are listed in Table A.2 of Appendix A) operating at the nominal temperature of 25°C. The system's electrical circuit parameters are listed in Table A.3 (Appendix A). The simulation type is discrete with a sample time of 40 µs.

5.5.1 SMO performance assessment

The proposed SMO has been tested with both FS-MPVOC and FS-MPDPC. It is obvious from Figure 5.16 that SMO have succeeded in providing accurately the observed variables, where it

can be noticed that there exist negligible observation error for the three state variables. This proves the good performance of the proposed SMO that uses only measurements of grid currents.
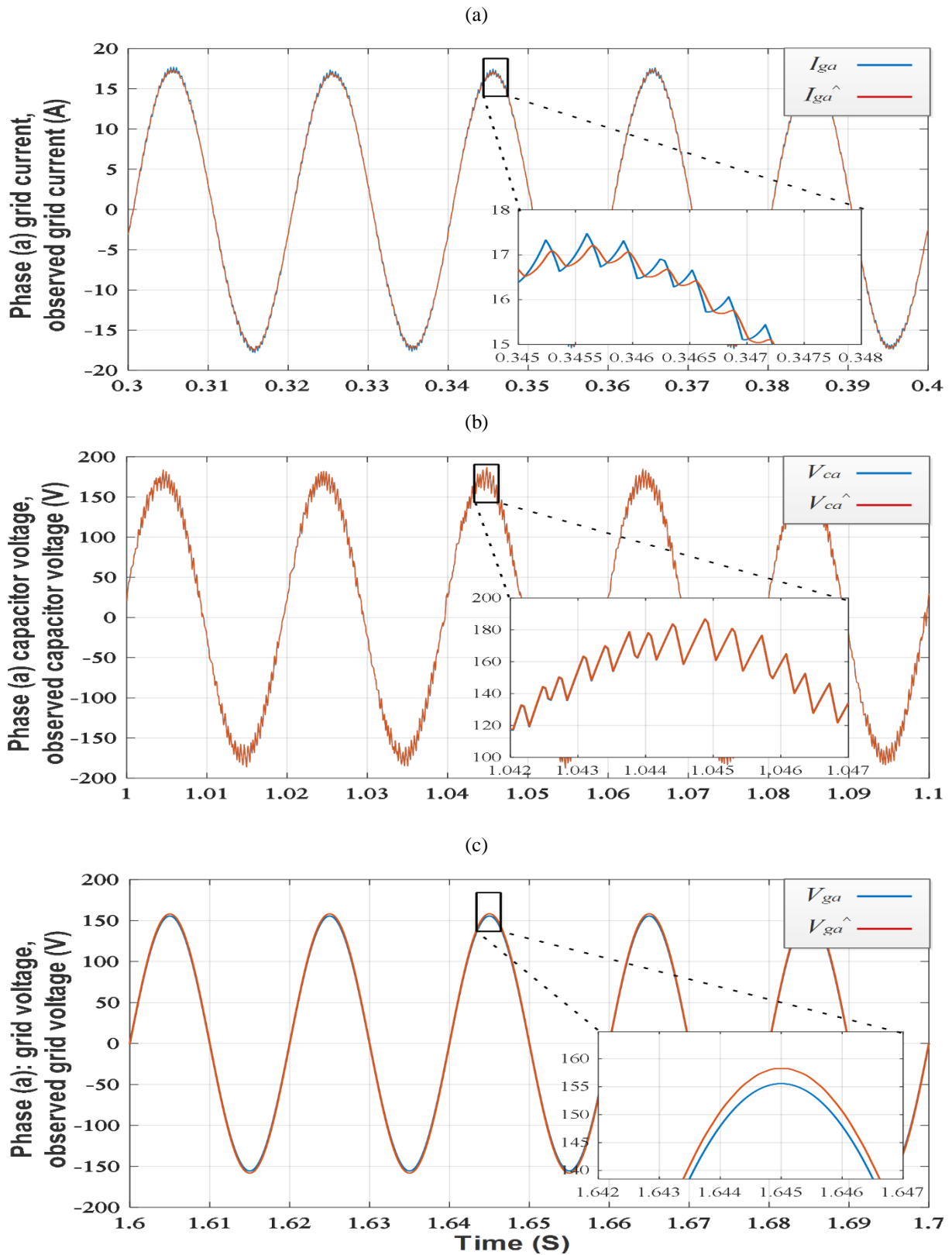
Figure 5.16 Performance of SMO: (a) grid current, (b) capacitor voltage, (c) grid voltage

5.5.2 Unity power factor operation

This section shows the system responses using the two proposed techniques for unity power factor operation i.e. no reactive power injected to the grid. To challenge the proposed FS-MPVOC and FS-MPDPC the time varying sun irradiance profile shown below is considered.
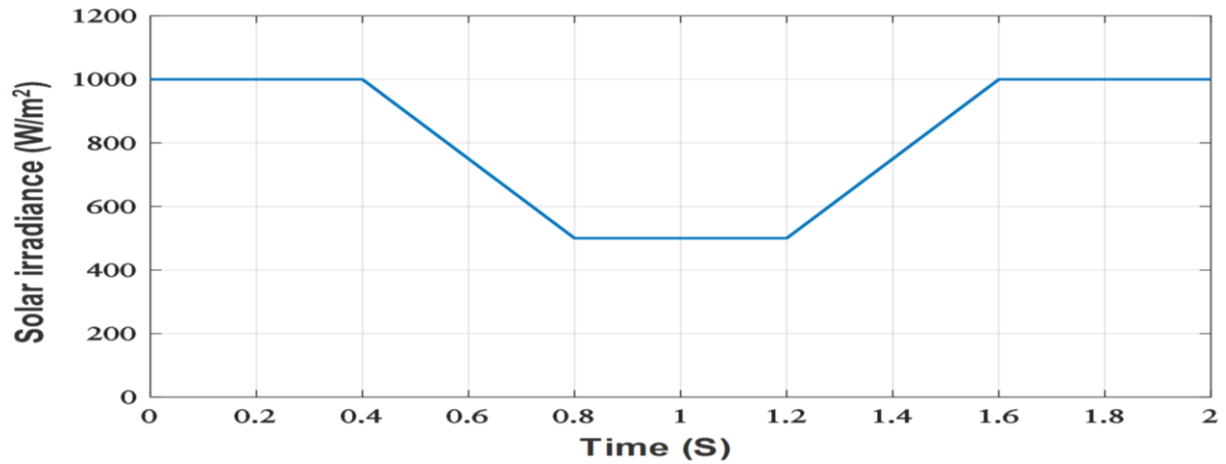
Figure 5.17 Solar irradiance level

(a)

(b)

(c)
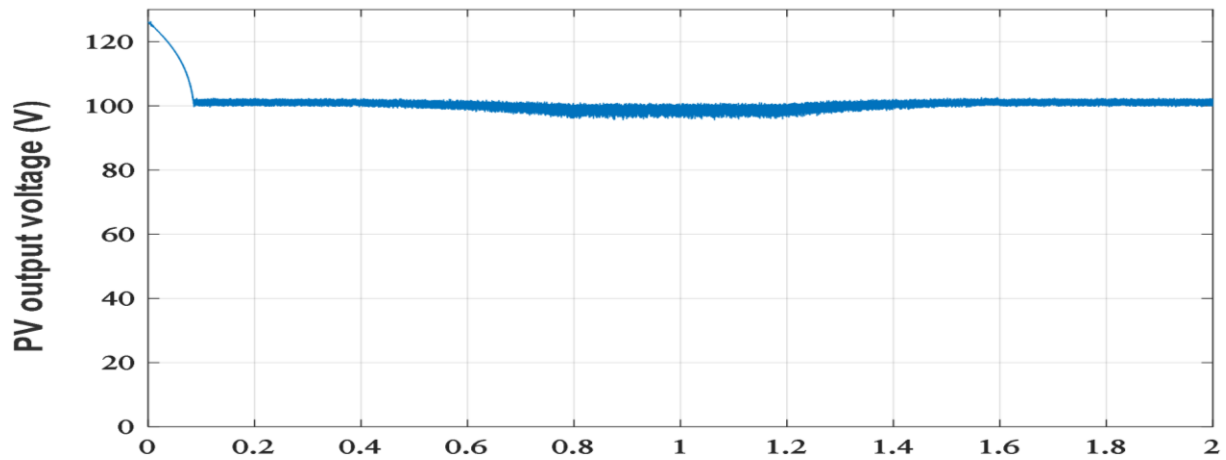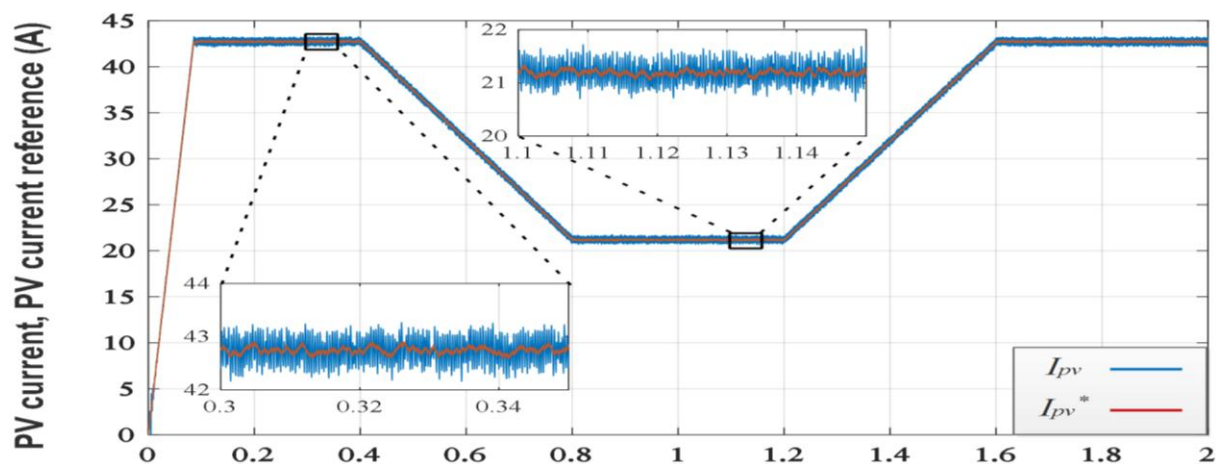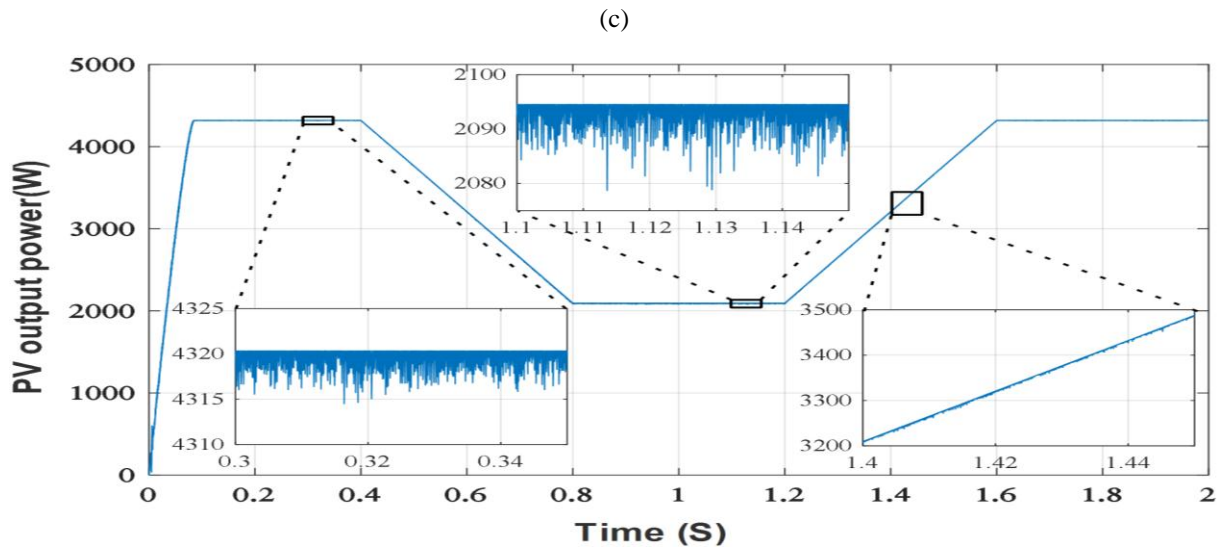
Figure 5.18 FS-MPVOC responses of: (a) PV output voltage, (b) PV output current, (c) PV output power

(a)

(b)

(c)
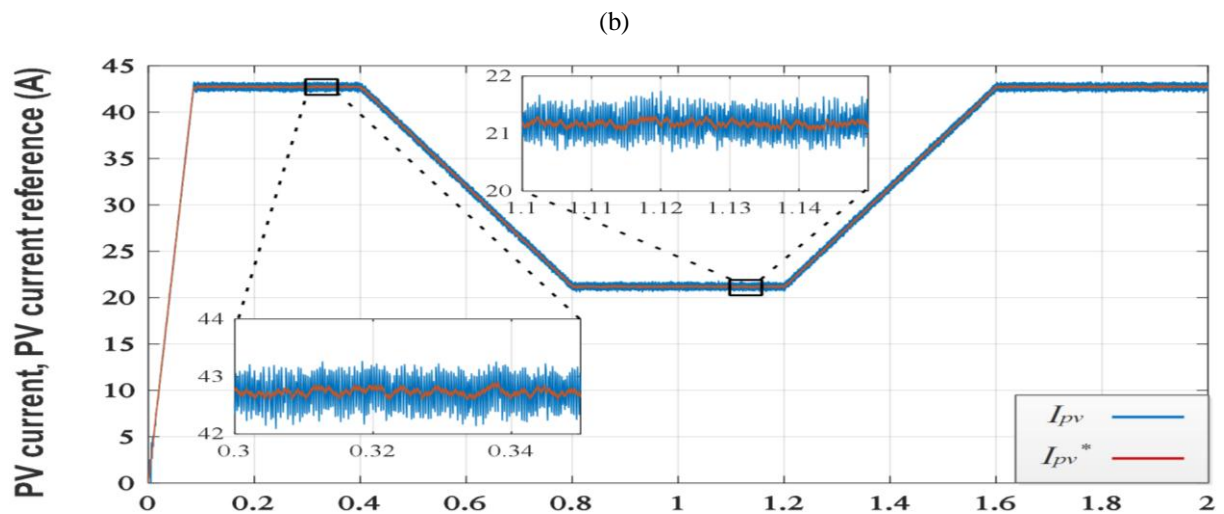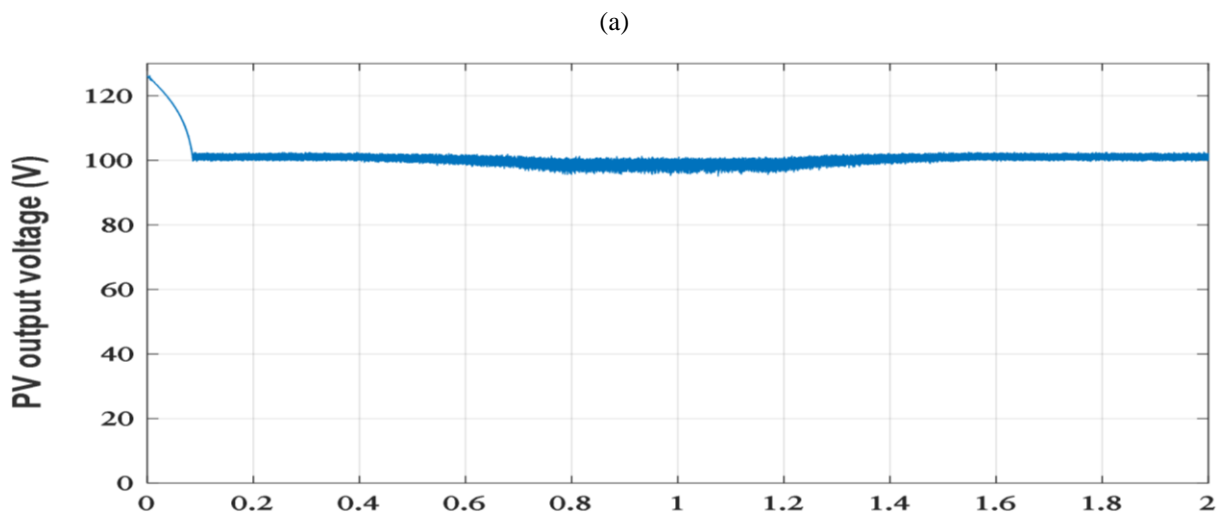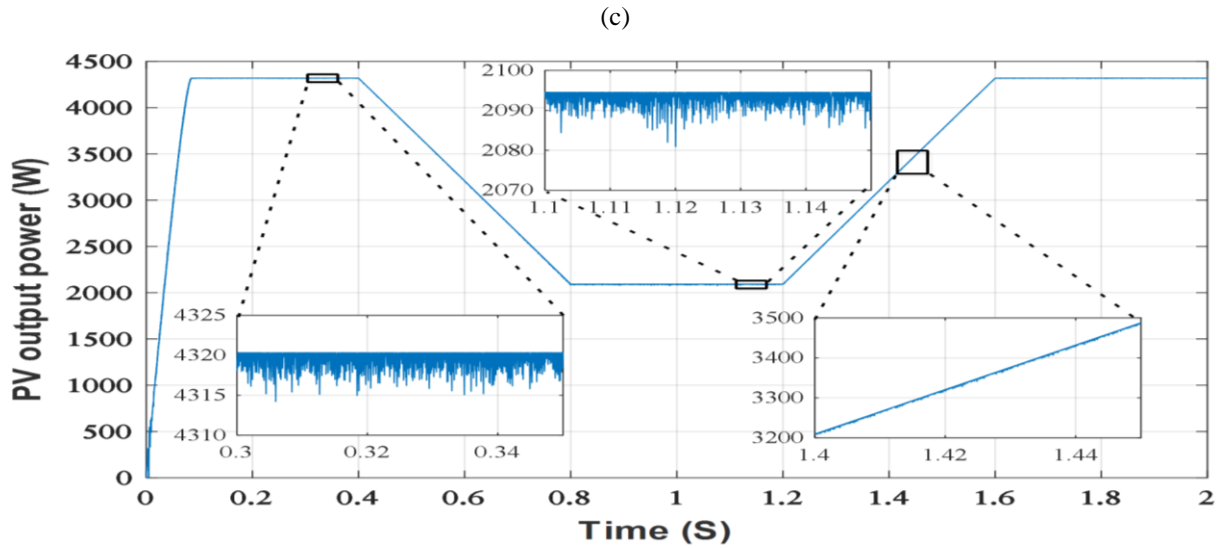
Figure 5.19 FS-MPDPC responses of: (a) PV output voltage, (b) PV output current, (c) PV output power

Figures 5.18 and 5.19 show the responses of the output PV voltage, current, and power for FS-MPVOC and FS-MPDPC, respectively. From Figures 5.18(a) and 5.19(b), the PV voltage at the MPP is around 100 V which is lower than the grid voltage. This confirms the boosting ability of CSI using a single-stage configuration. In Figures 5.18(b) and 5.19(b), it is obvious that PV current tracks perfectly the reference generated by the P&O algorithm which proves the rapidity and good performance of the DC link regulation loops and the fast dynamics of both proposed techniques. This has allowed the PV power to be maximized during all irradiance level as shown in Figure 5.18(c) and 5.19(c), where the MPP is reached within the order of milliseconds.

(a)

(b)
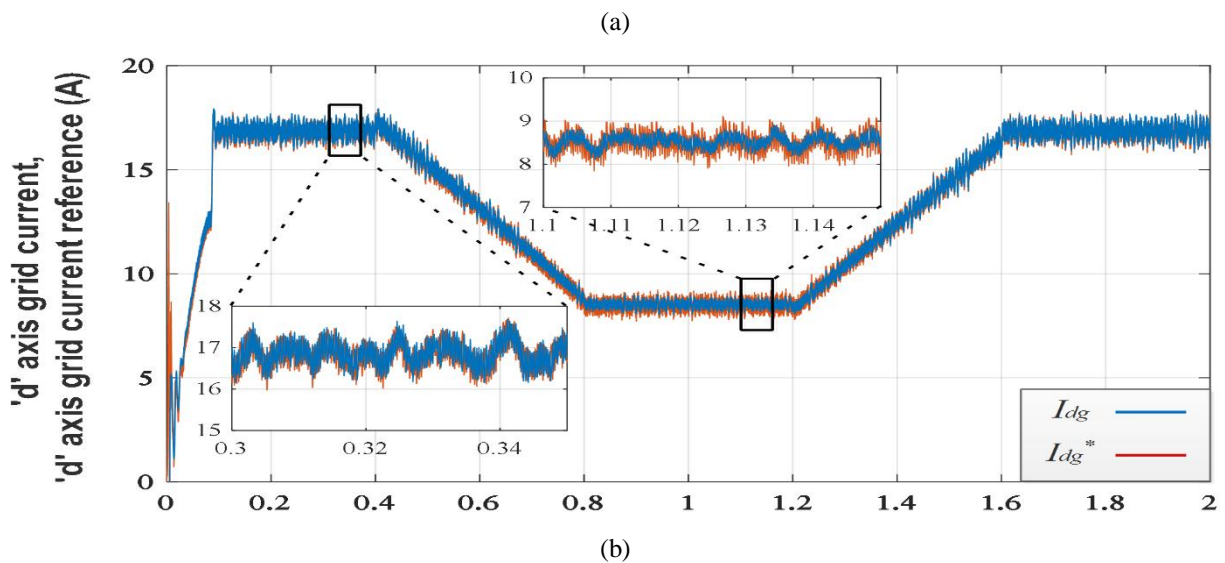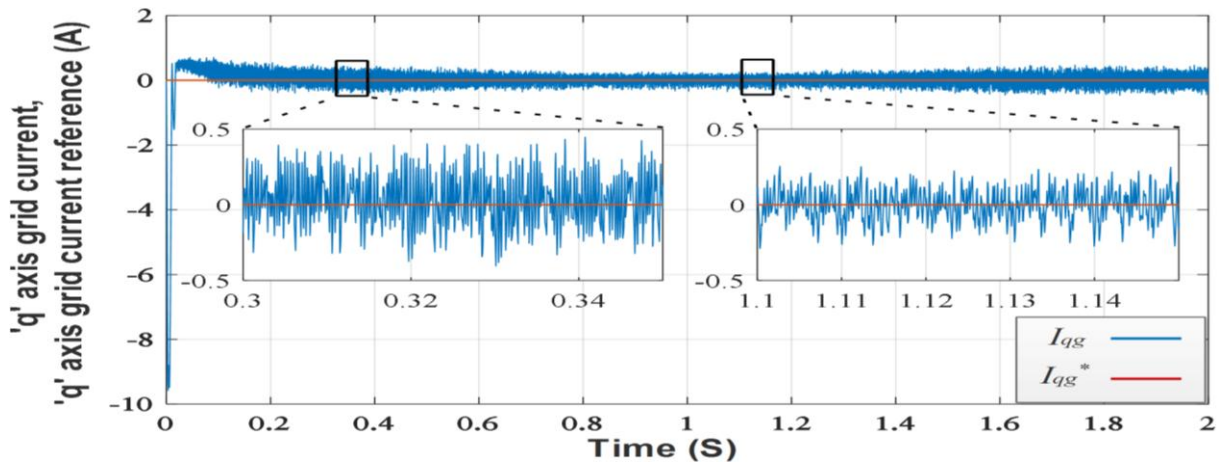
Figure 5.20 FS-MPVOC responses of: (a) grid *d*-axis current, (b) grid *q*-axis current

Figure 5.20 show the *d*-axis and *q*-axis grid currents, where it can be noted that they pursue their references rapidly and accurately. The *q*-axis current is practically null with small oscillations because its reference is set to 0 to attain unity power factor operation.

(a)

(b)
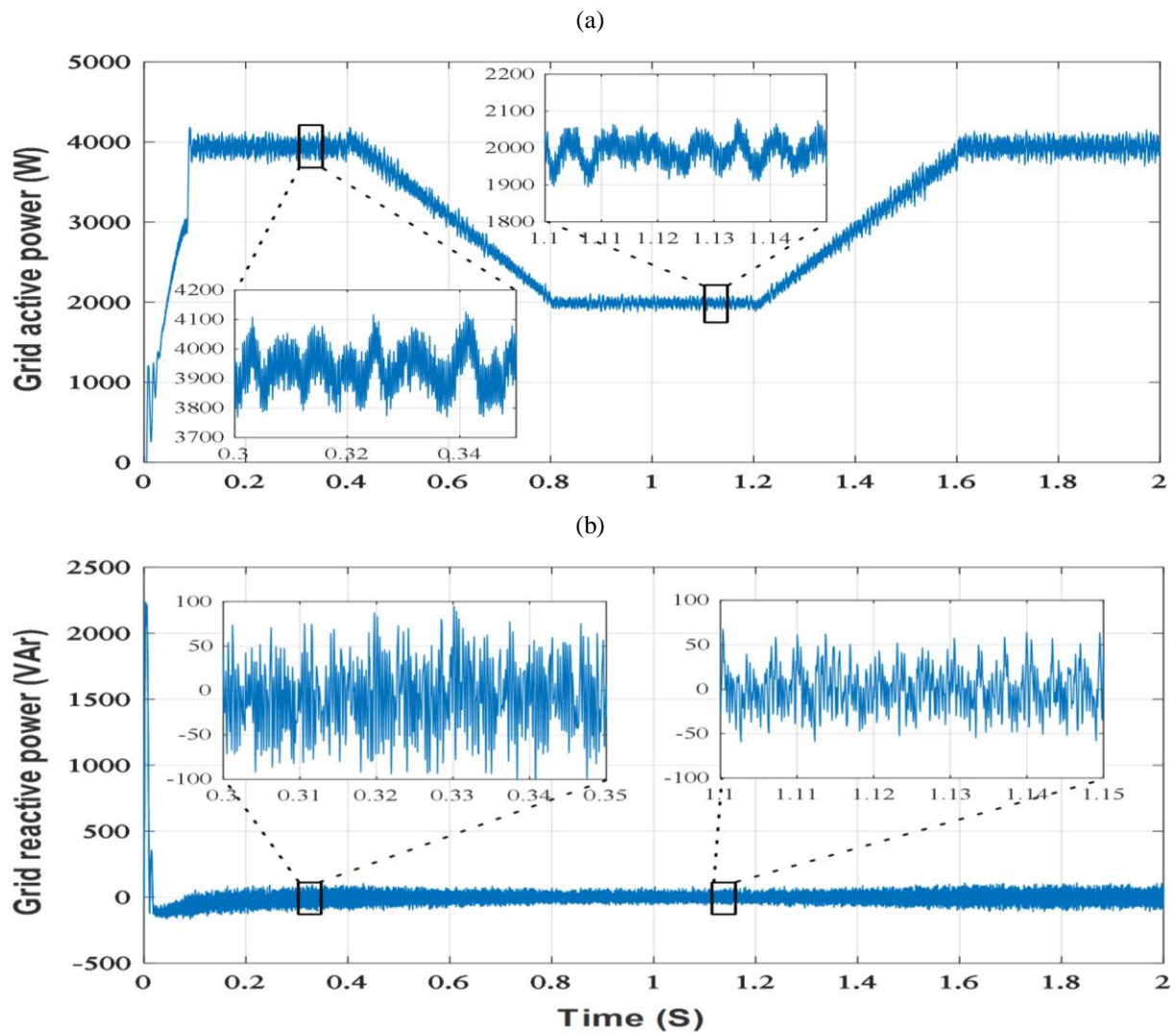
Figure 5.21 FS-MPVOC responses of: (a) grid active power, (b) grid reactive power

This is reflected in the responses of active and reactive powers (Figure 5.21), since the d-axis and q-axis currents represent the images of active power and reactive power, respectively.

From Figure 5.22, it can be seen that the grid current and voltage are in phase practically, consequently unity power factor is achieved.
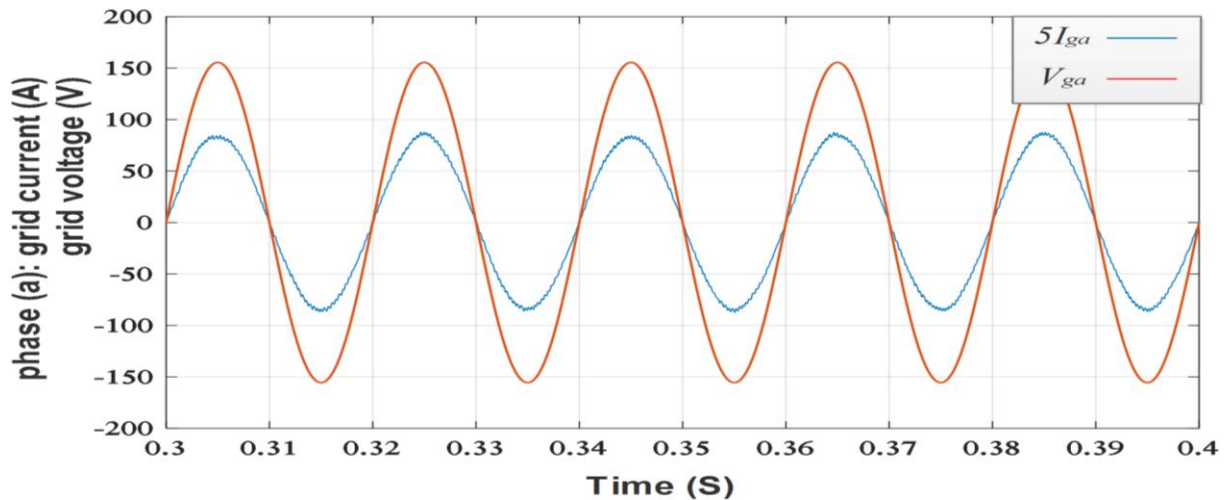
Figure 5.22 FS-MPVOC responses of phase (*a*) grid current and voltage

Figure 5.23 shows the responses of active and reactive powers using FS-MPDPC. It is obvious that the powers track their references swiftly, with small oscillations, and negligible over- and undershoots. This proves the good performance of the proposed power control technique. It can be noticed also that the reactive power reference is practically null. Thus, unity power factor is attained, as it can be seen in Figure 5.24, where it is clear that the grid current and voltage are practically in phase.

(a)

(b)
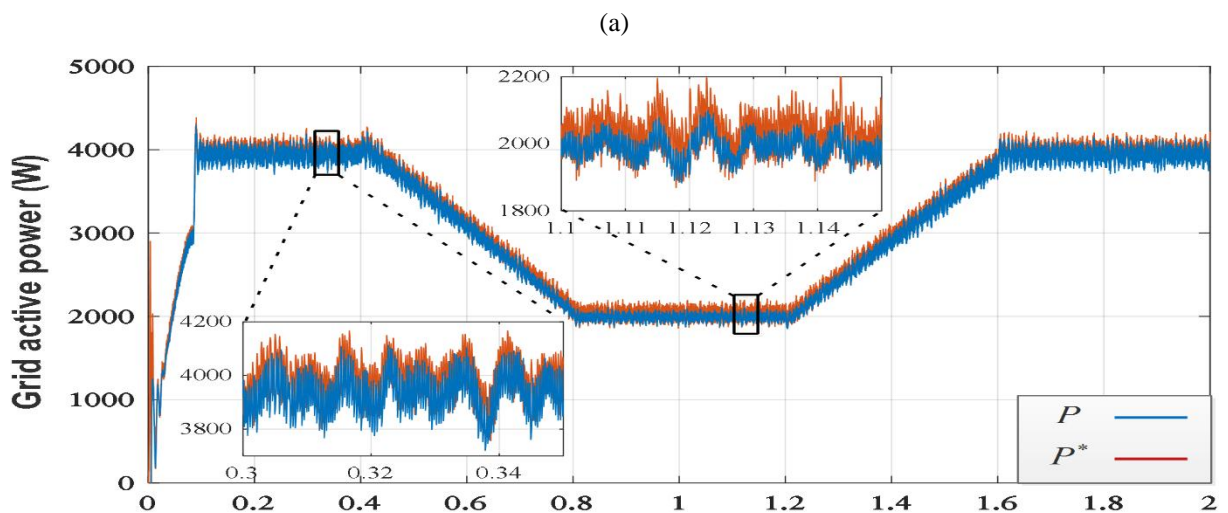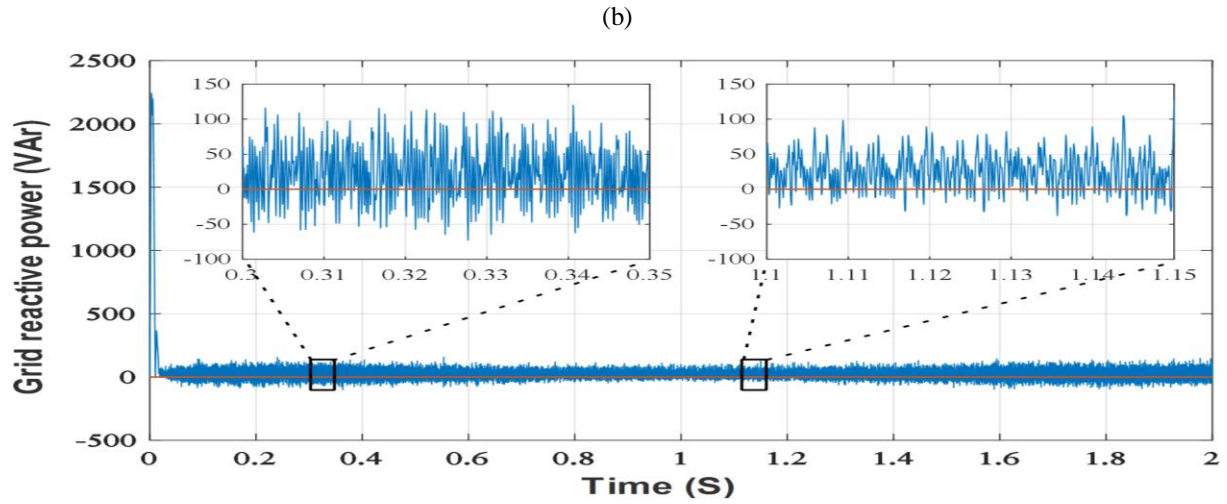
Figure 5.23 FS-MPDPC responses of: (a) grid active power, (b) grid reactive power
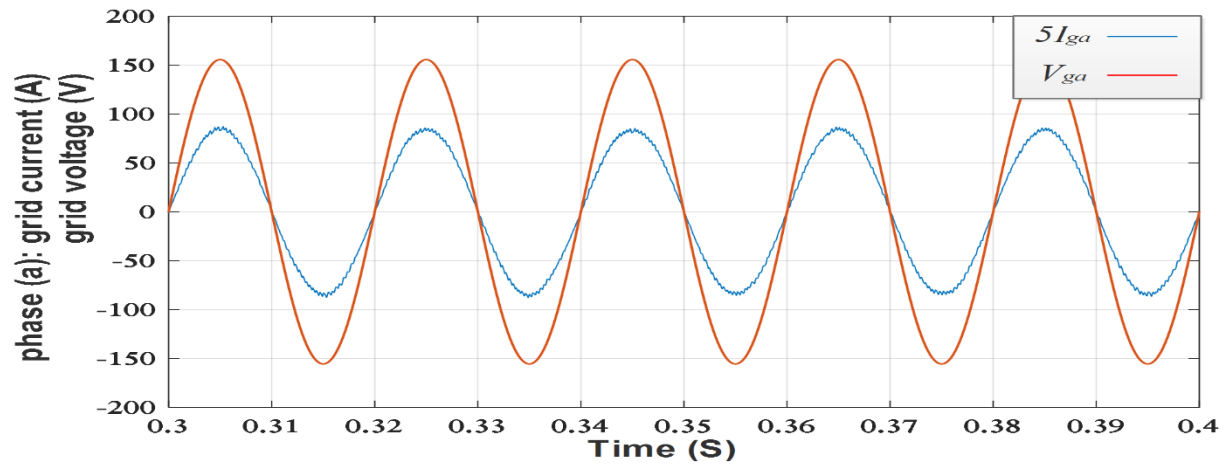

*Figure 5.24* FS-MPDPC Response of phase (*a*) grid current and voltage
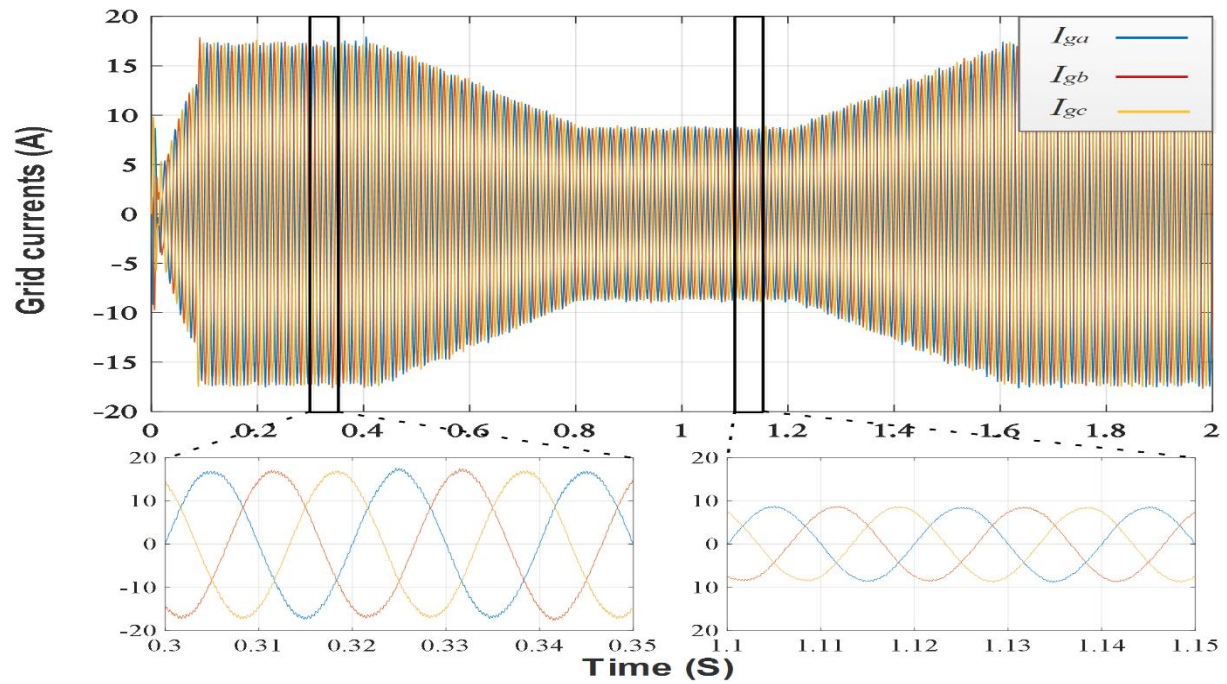
Figure 5.25 FS-MPVOC responses of three phase grid currents

The three phase grid currents exhibited in Figures 5.20(c) and 5.21 for FS-MPVOC, and FS-MPDPC, respectively, are practically sinusoidal and lowly distorted, and in agreement with grid standards. The computed THD values during different irradiance levels for the proposed techniques are listed in Table 5.1.
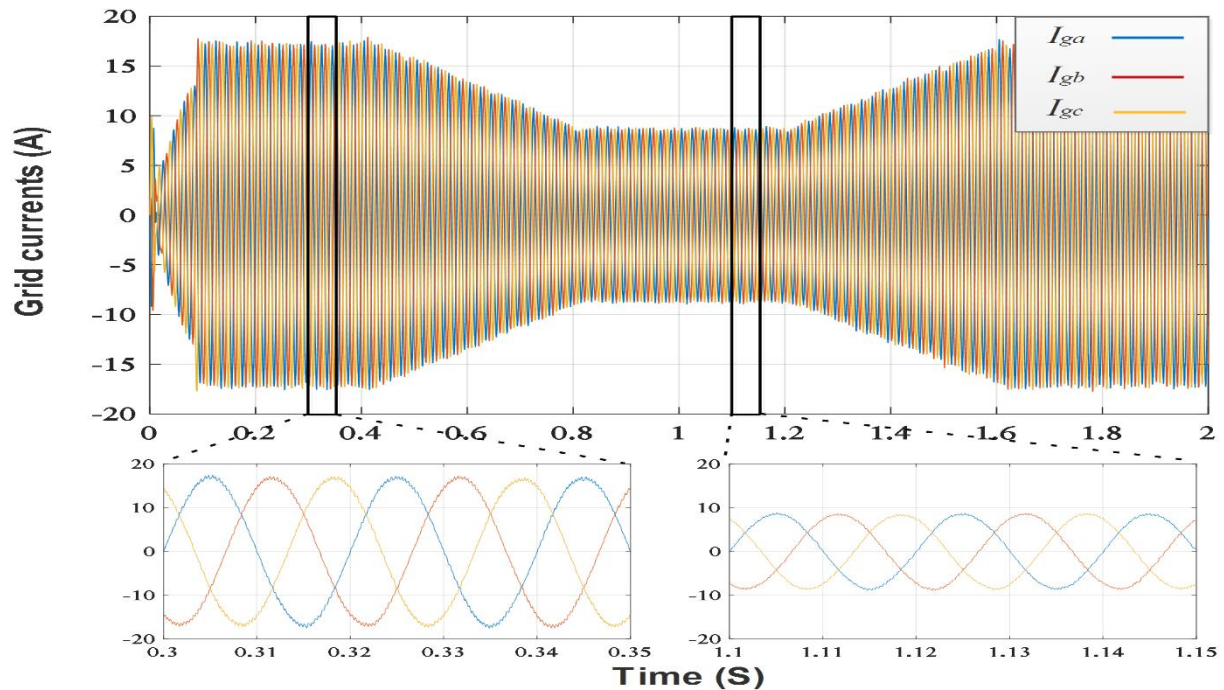
Figure 5.26 FS-MPDPC responses of three phase grid currents.

Table 5.1 Grid currents THD for unity power factor operation during different irradiance levels

Time		0-0.4s	0.4-0.8s	0.8-1.2s	1.2-1.6s
Grid currents THD (%)	FS-MPVOC	1.73	1.97	2.14	2.25
	FS-MPDPC	2.08	1.84	1.82	2.61

Figures 5.27 and 5.28 show the efficiency of the single-stage conversion chain for FS-MPVOC and FS-MPDPC, respectively. The obtained efficiency is relatively high, where the mean efficiency for both technique is about 92%.
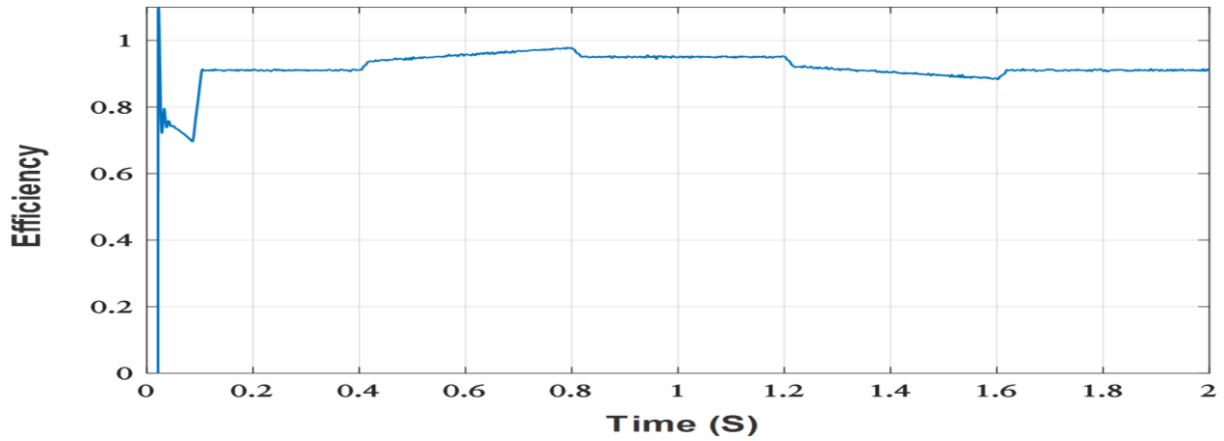
*Figure 5.27* System's efficiency using FS-MPVOC
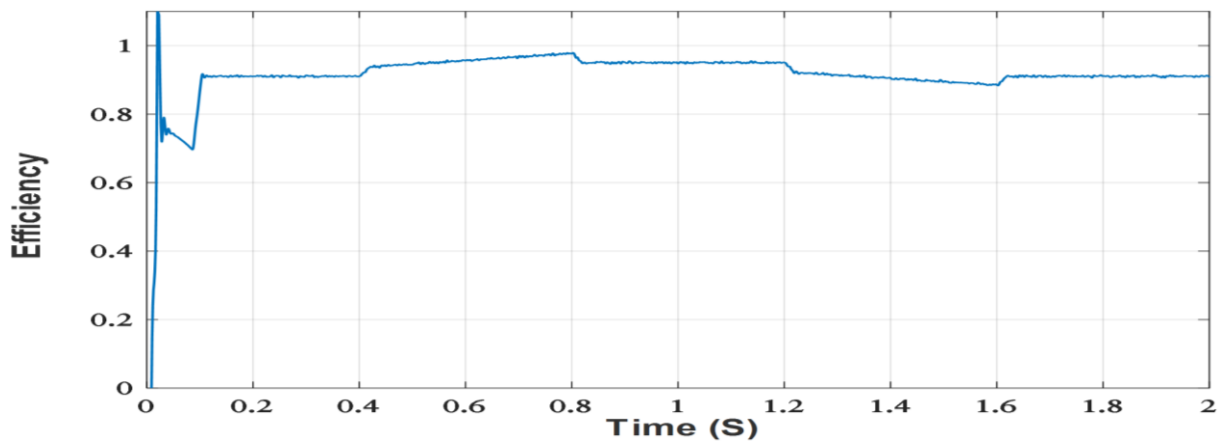
Figure 5.28 System's efficiency using FS-MPDPC

5.5.3 Reactive power injection

To assess the ability of the controllers to provide reactive power to the utility grid, a time changing reactive power reference is considered. The irradiance profile remains the same used for unity power factor operation (Figure 5.17).

(a)

(b)

(c)
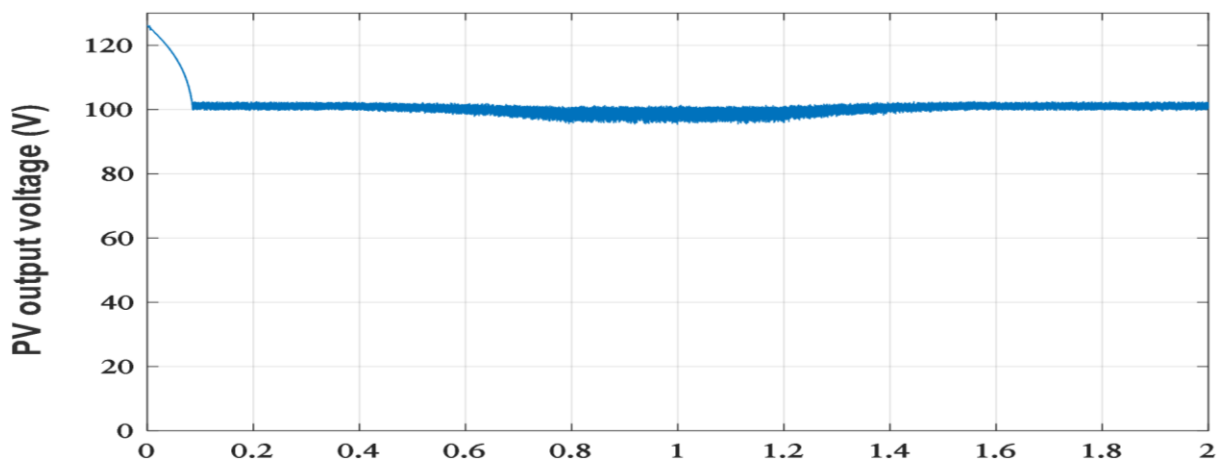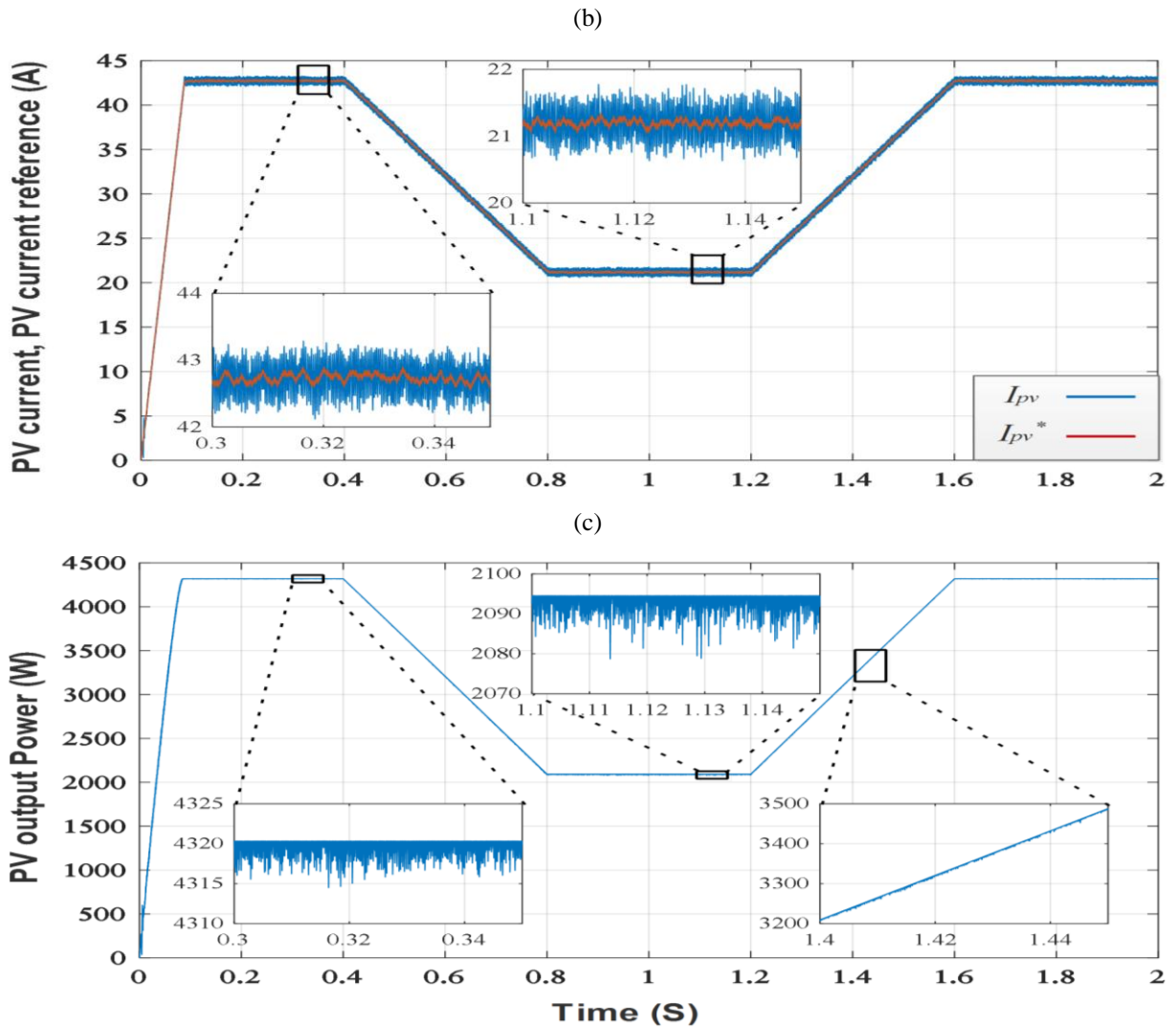
Figure 5.29 FS-MPVOC responses of: (a) PV output voltage, (b) PV output current, (c) PV output power

(a)

(b)

(c)
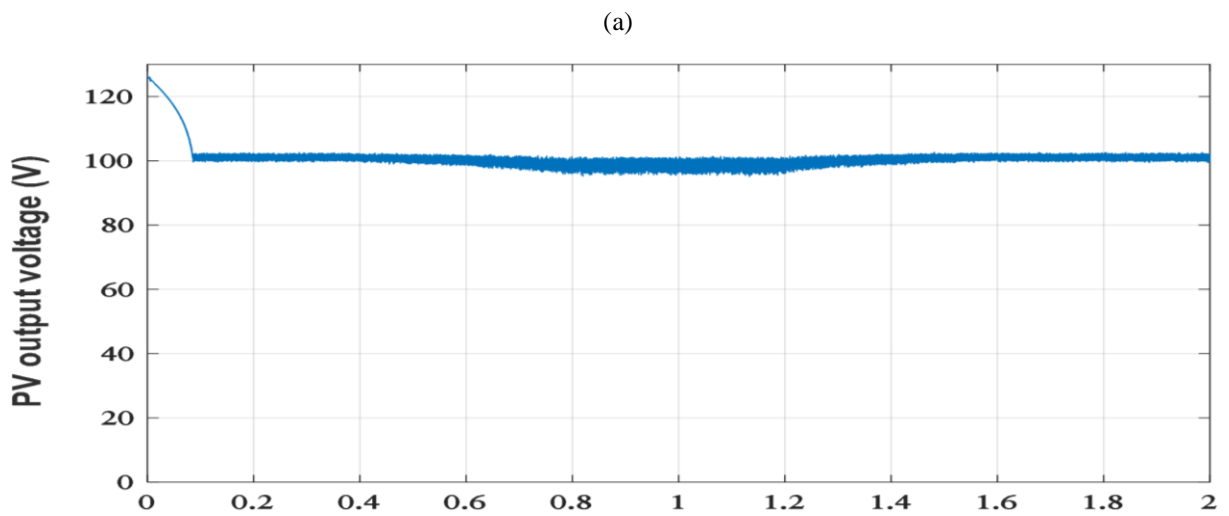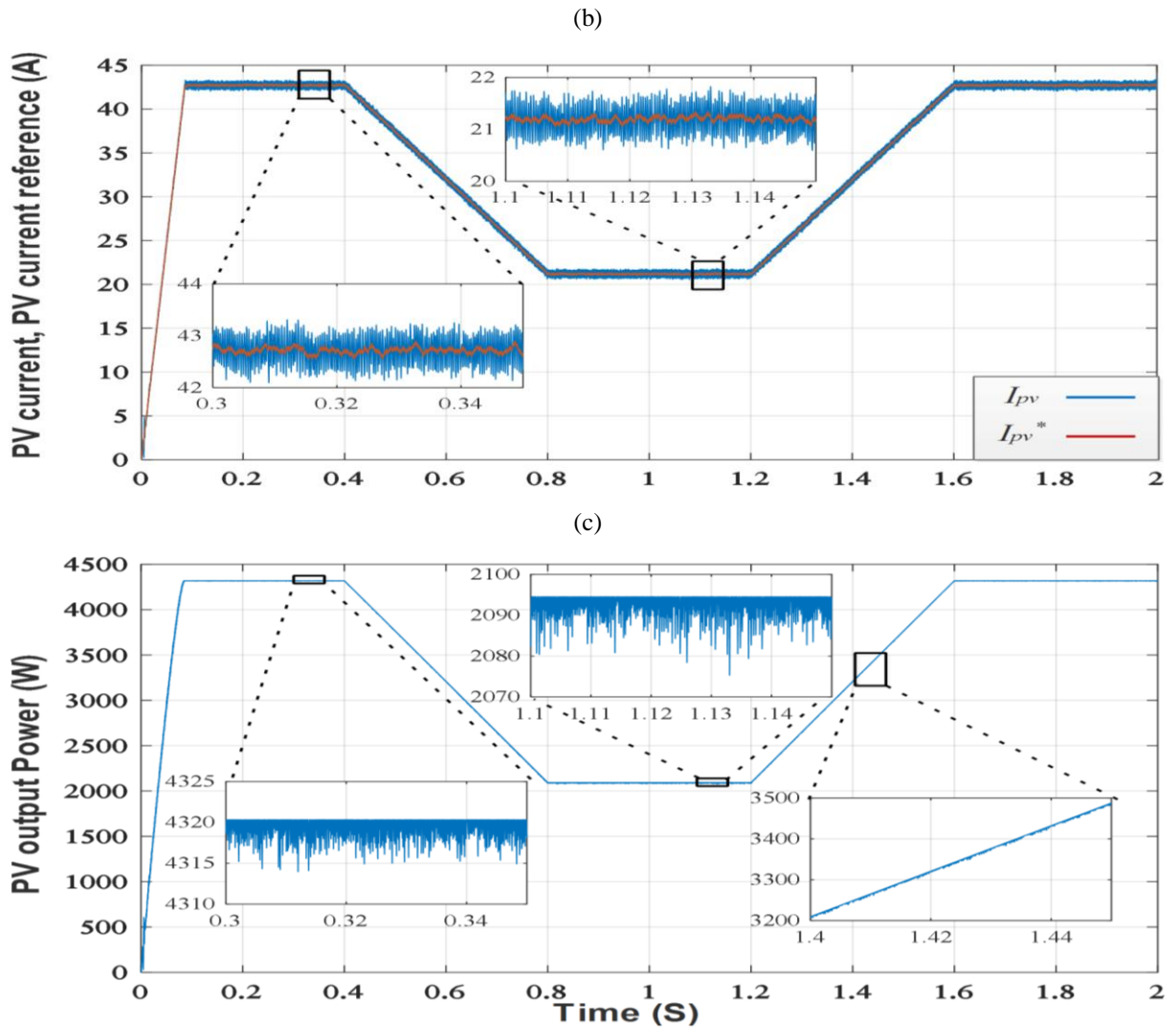
Figure 5.30 FS-MPDPC responses: (a) PV output voltage, (b) PV output current, (c) PV output power

Similarly to the first case, the PV output power track its reference rapidly for both techniques, this is due to the MPPT algorithm that provided PV current reference accurately, and the DC link regulators that have permitted a fast tracking of this reference.

(a)

(b)
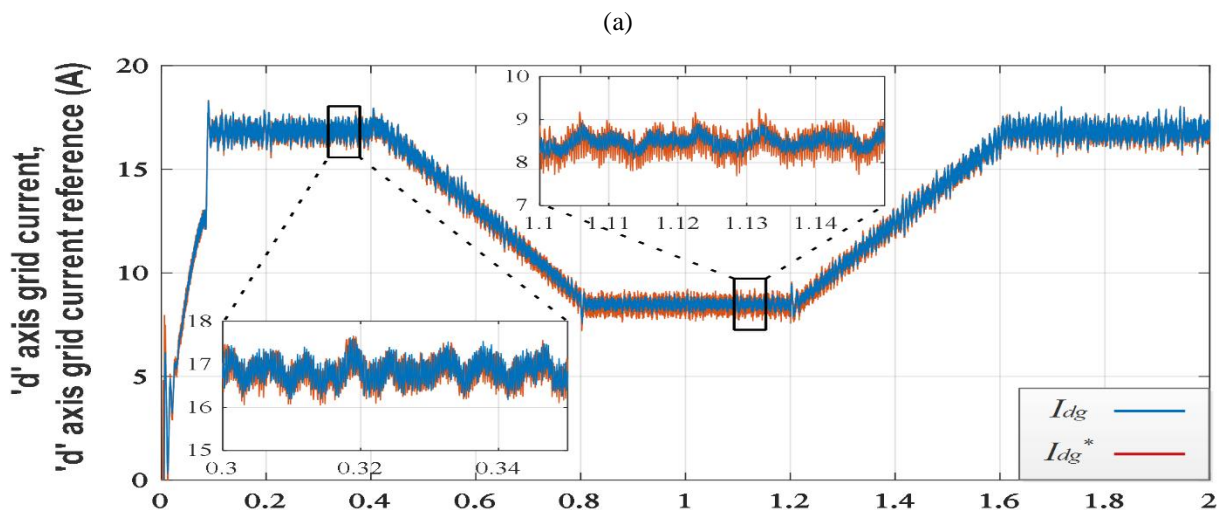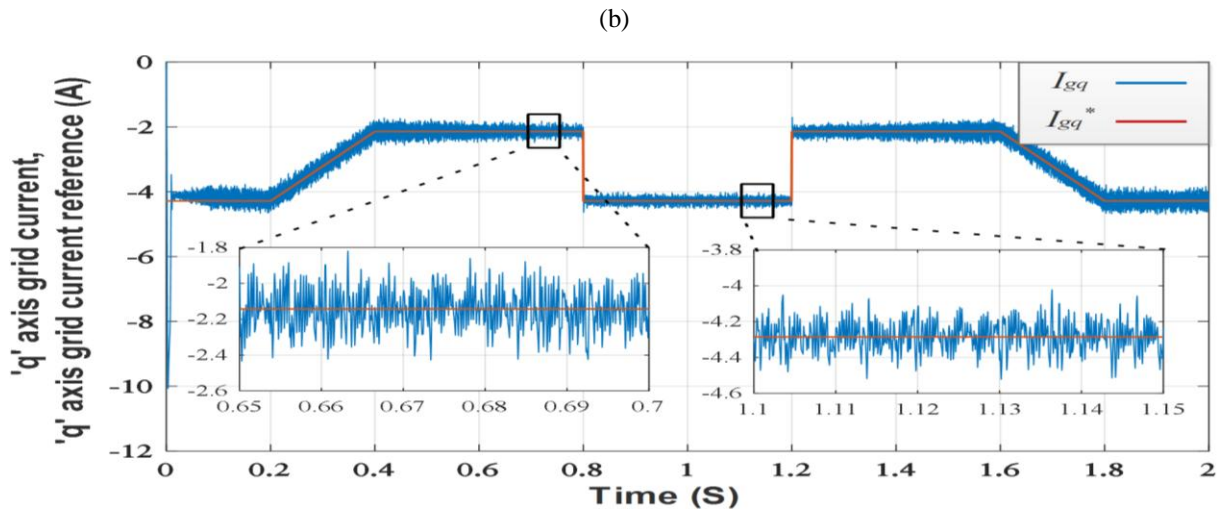
Figure 5.31 FS-MPVOC responses of: (a) *d*-axis grid current, (b) *q*-axis grid current

(a)

(b)
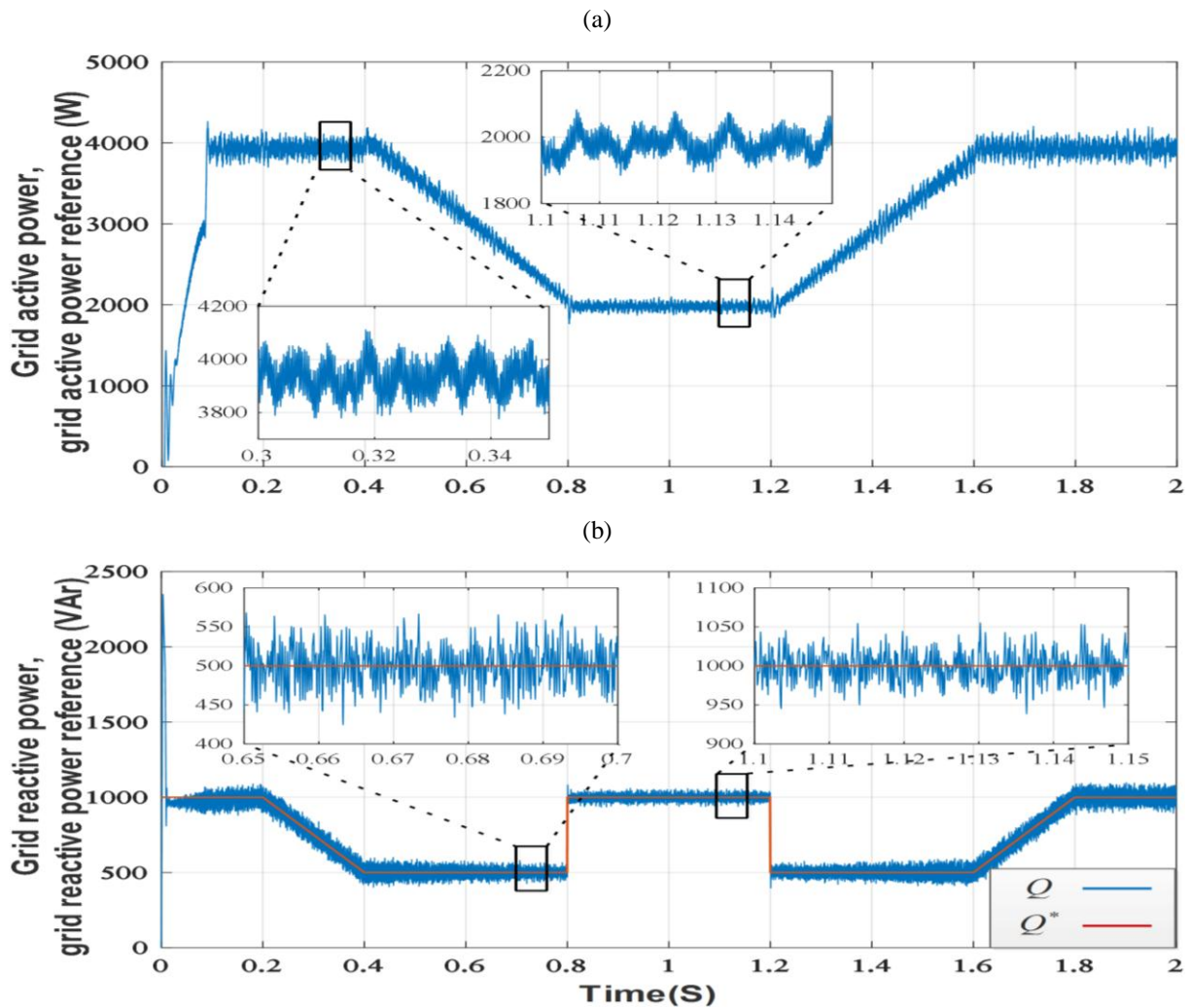
Figure 5.32 FS-MPVOC response of: (a) grid active power, (b) grid reactive power

Figure 5.31 and 5.32 show the *dq* grid currents, and grid powers, respectively. It can be seen that the currents pursue their references rapidly and accurately. The same remark can be made

about the grid powers. Moreover, reactive power is injected into the grid in this case without perturbing the PV power, or the grid active power. This demonstrates the decoupled control ensured by the proposed FS-MPVOC. Furthermore, in Figure 5.33, it is shown that the currents respond rapidly by changing their phases at the instant of sudden change in the reactive power reference.
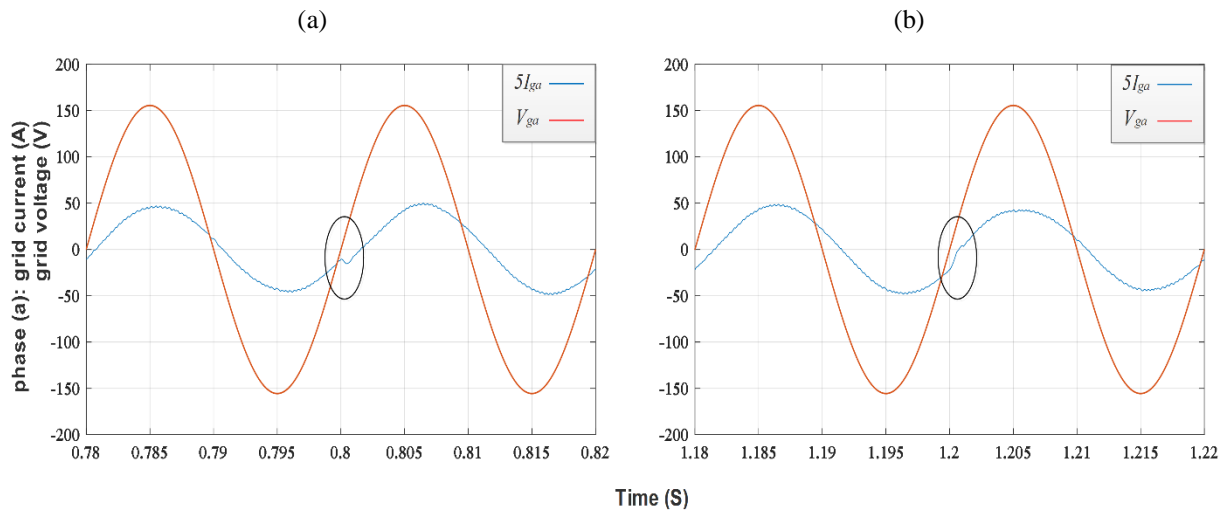

Figure 5.33 FS-MPVOC responses of phase (*a*) grid current and voltage during step change in reactive power reference: (a) zoom on first step change, (b) zoom on second step change.

Figure 5.34 shows the responses of active and reactive powers using FS-MPDPC. It can be seen that reactive power tracks its reference even during step change without affecting the performance of the system. This can be noted in the response of the grid current and voltage exhibited in Figure 5.35, where it is obvious that the grid currents respond rapidly to sudden changes in reactive power reference by shifting their phases.

(b)
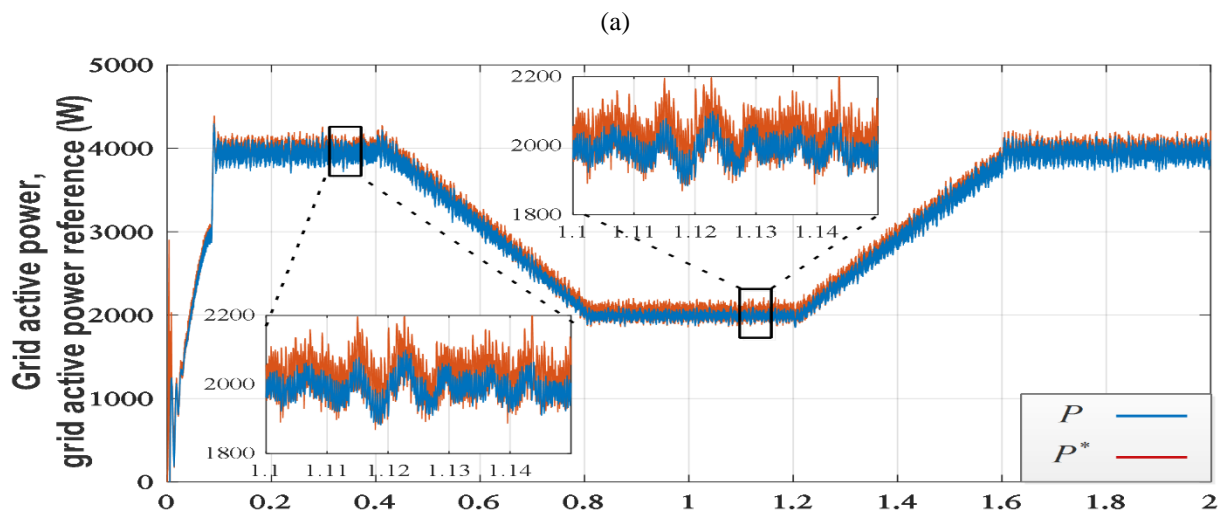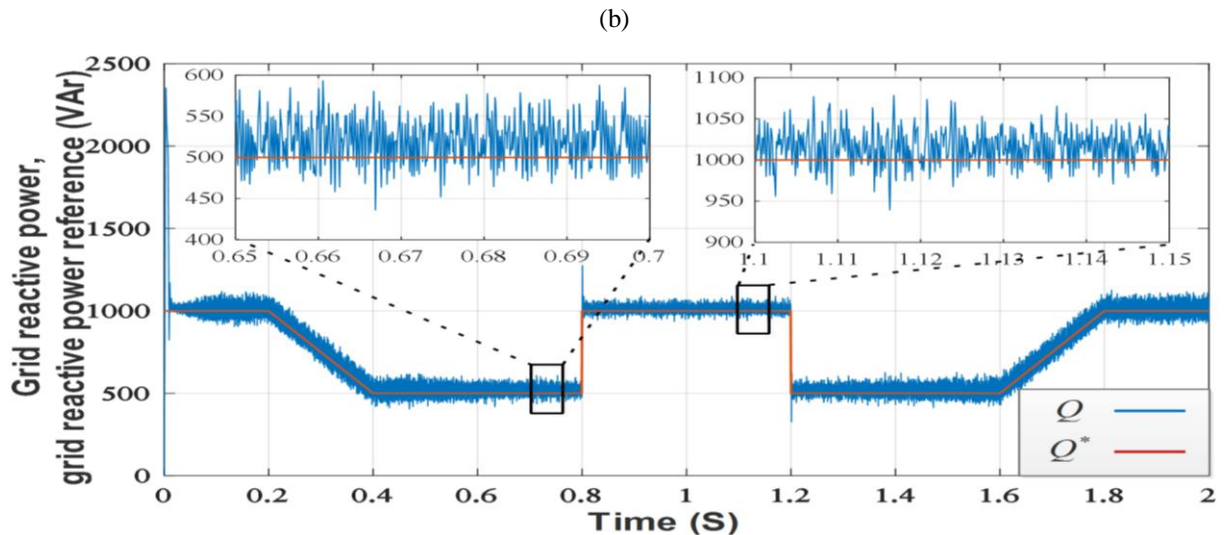
Figure 5.34 FS-MPDPC responses of: (a) grid active power, (b) grid reactive power

(a)   (b)
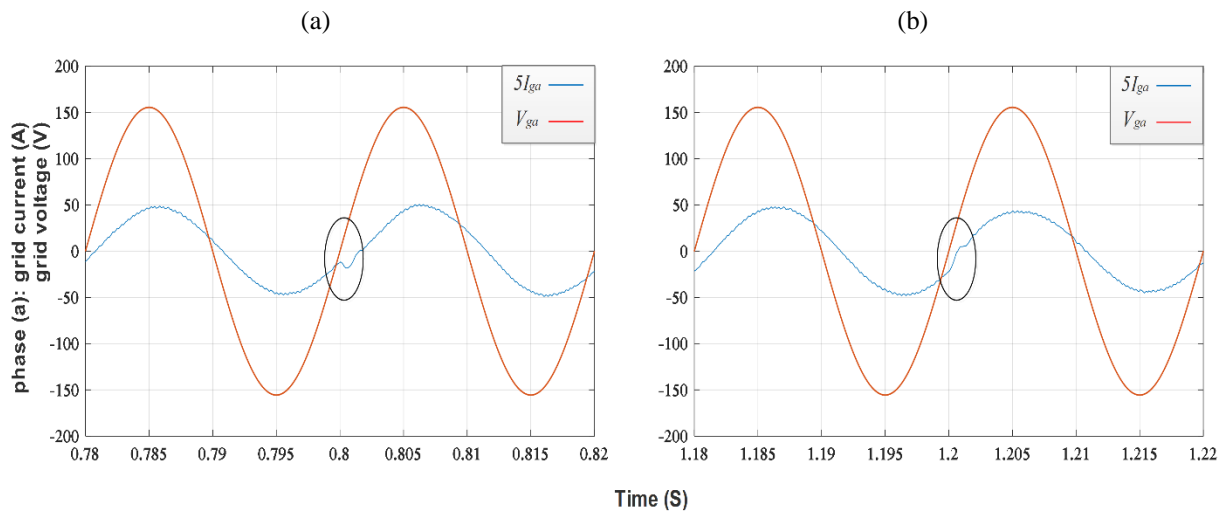
*Figure 5.35* FS-MPDPC Responses of phase (*a*) grid current and voltage during step change in reactive power reference: (a) zoom on first step change, (b) zoom on second step change.

Figure 5.36 and 5.37 depict the responses of grid currents using FS-MPVOC, and FS-MPDPC, respectively. Similarly to the first case, it is clear that the current waveforms are sinusoidal and lowly distorted, and in agreement with grid standards.
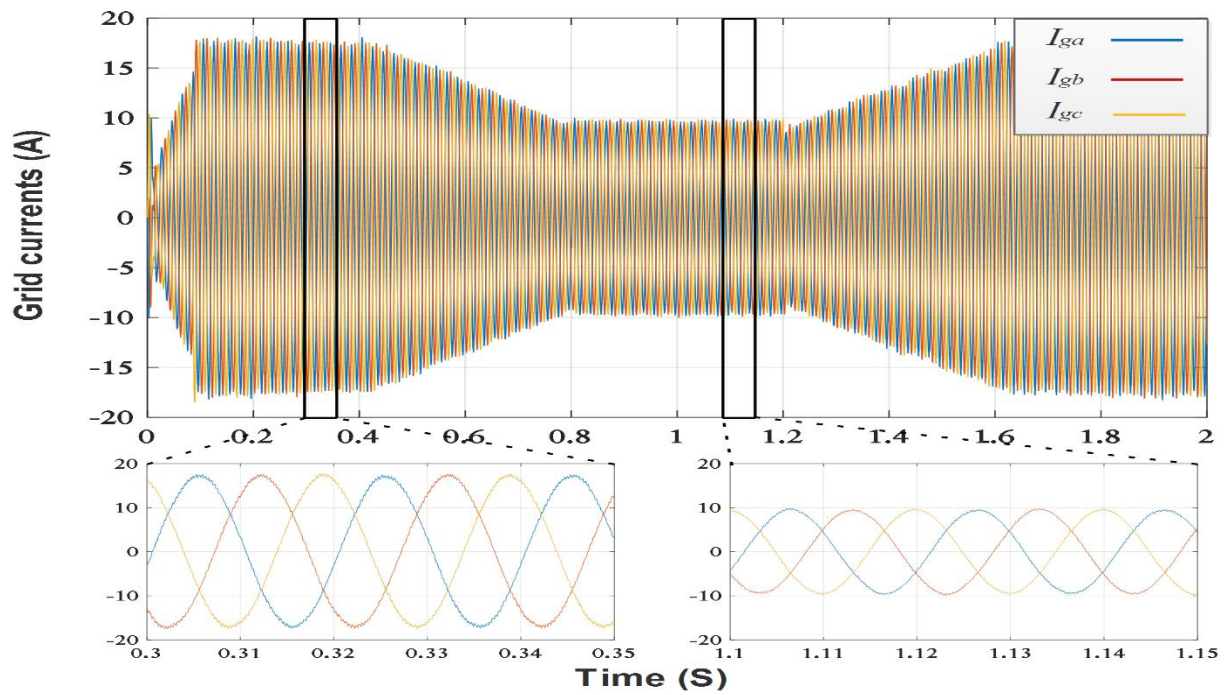
*Figure 5.36* FS-MPVOC responses of three phase grid currents
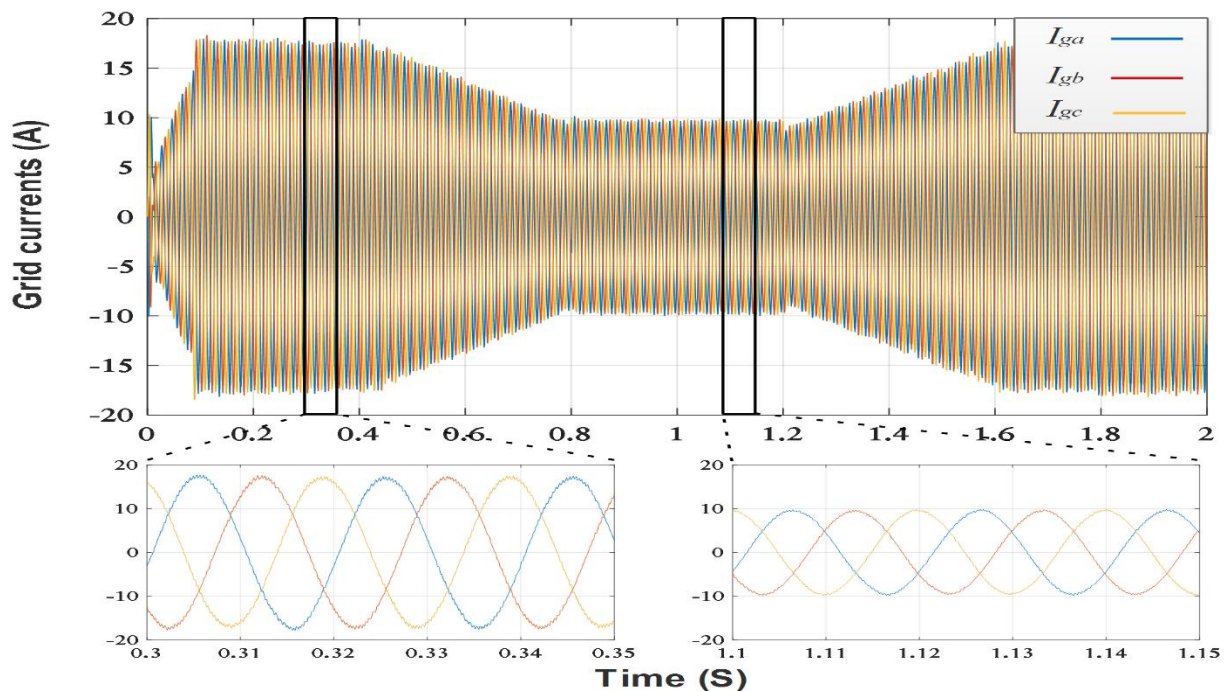
Figure 5.37 FS-MPDPC responses of three phase grid currents

Figures 5.38, and 5.39 depict the conversion chain efficiencies using FS-MPVOC, and FS-MPDPC, respectively. It can be noticed that reactive power injection have not affected the system's efficiency, where the mean efficiency was the same as the case of unity power factor operation (about 92%).
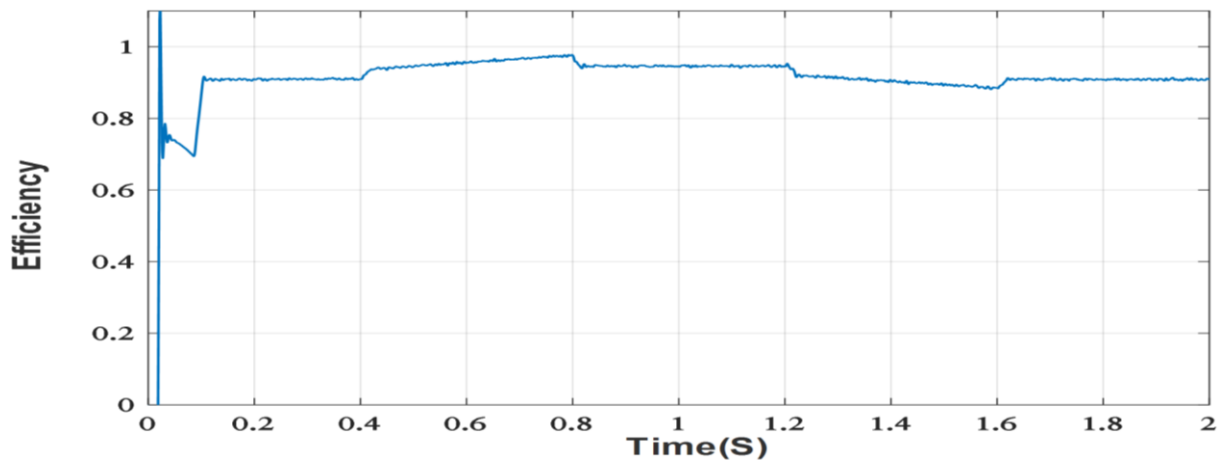
Figure 5.38 System's efficiency using FS-MPVOC
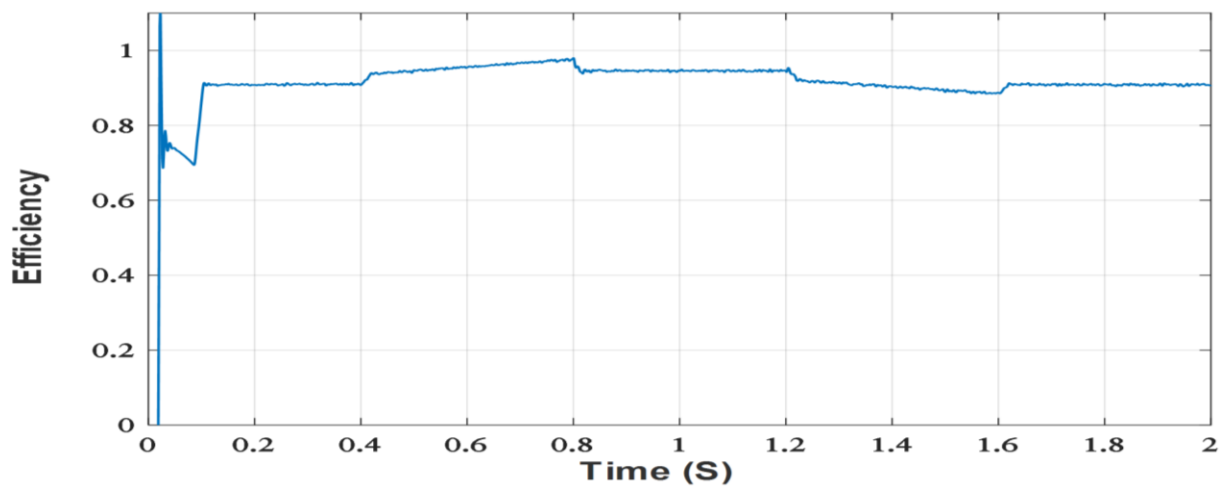
Figure 5.39 System's efficiency using FS-MPDPC

5.5.4 Comparison between proposed active damping methods and passive damping
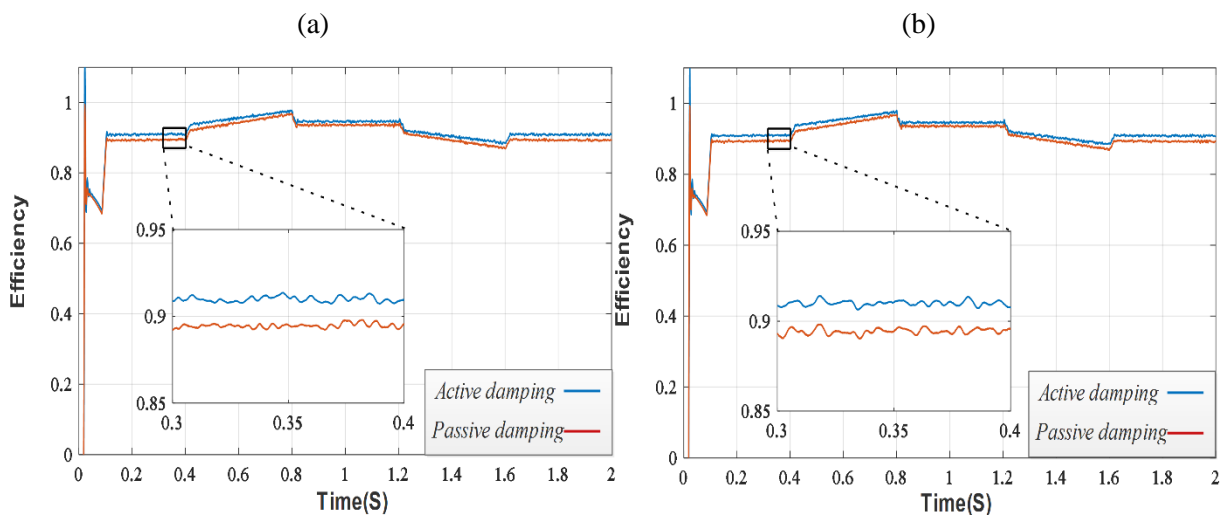
Figure 5.40 efficiency comparison between active and passive damping methods using: (a) FS-MPVOC, (b) FS-MPDPC

Table 5.2 Comparison table of active and passive damping methods

	Active damping method	*Passive damping*
Mean efficiency	92%	91%
Grid currents THD (%)	<2.6	>3
Active power oscillations	±50 W	±70 W
Reactive power oscillations	±70 W	±85 W
PV power oscillations	5 W	9 W

It is obvious from Figure 5.38 that active damping is better in terms of efficiency of the conversion chain, where it can be noted that the efficiency using active damping is superior by 1% as compared with this using passive damping. Furthermore, active damping methods have improved the quality of PV power, grid currents and grid powers (Table 5.2).

5.6 Real-time implementation results

Hardware in the loop (HIL) implementation is a type of real-time (RT) simulation, which is used to test and validate the controller design. The reason the use of a HIL process is becoming more prevalent is driven by three major factors: cost, time, safety. HIL can easily run through thousands of possible scenarios to properly exercise the controller without the cost and time associated with actual physical tests [5.8]. It also takes into account the communication problems and controller computational limitations. Consequently, the obtained results are more practical, and close to reality as compared with numerical simulations. Figure 5.41 shows a typical HIL implementation setup.
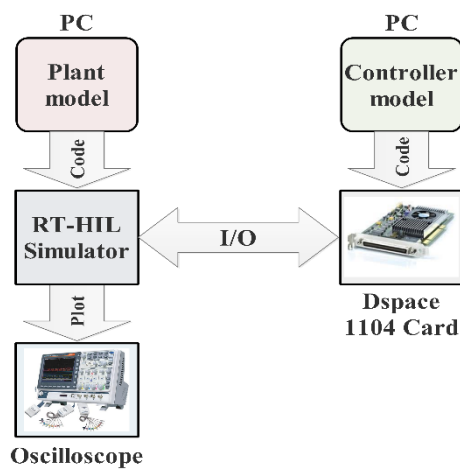
Figure 5.41 Typical HIL implementation setup.

In this study, the proposed techniques for the grid-connected photovoltaic CSI have been verified through RT-HIL implementation. The system parameters are similar to those used in numerical simulations. The actual HIL system uses a dSPACE platform for the implementation of the controller model, whereas, a real-time central processing unit (CPU) contains code for the physical system that is generated from the plant model. The obtained results are plotted and recorded using an oscilloscope. The controllers have been implemented with a sampling time of 40 μs.

5.6.1 Unity power factor operation

5.6.1.1 FS-MPVOC
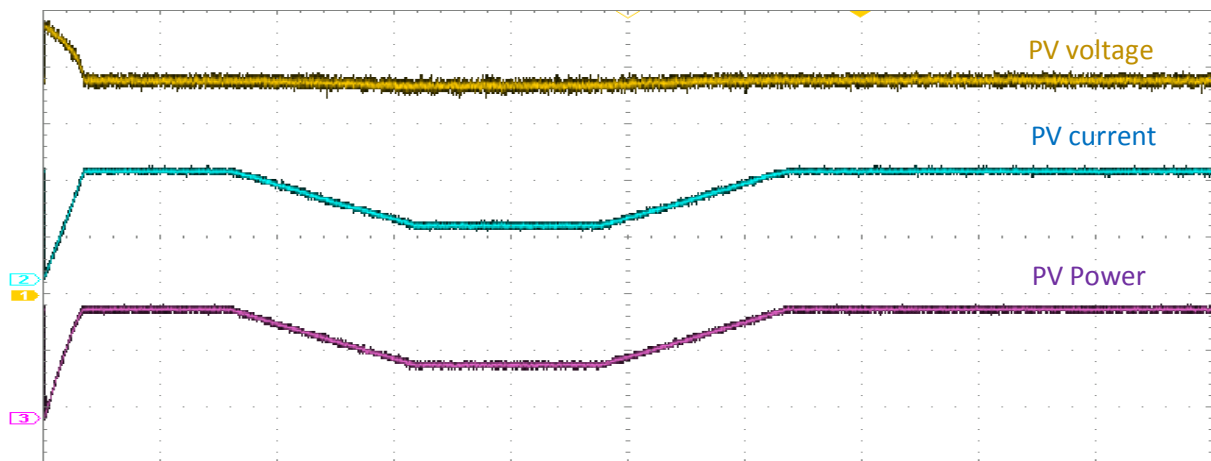
Figure 5.42 FS-MPVOC HIL responses of PV output: voltage (25V/div), current (10A/div), and power (2kW/div)
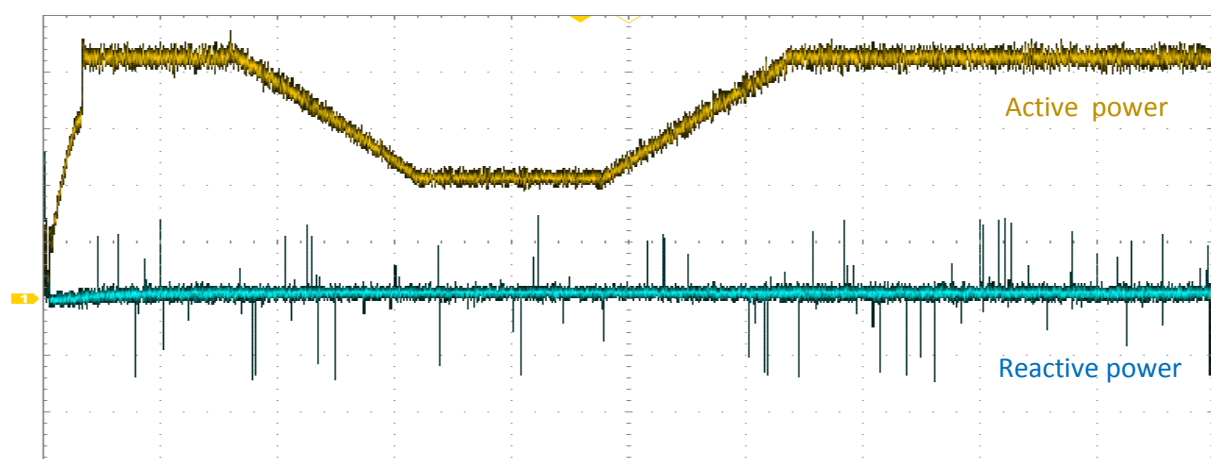
Figure 5.43 FS-MPVOC HIL responses of grid: active power (1kW/div) and reactive power (1kVAr/div)
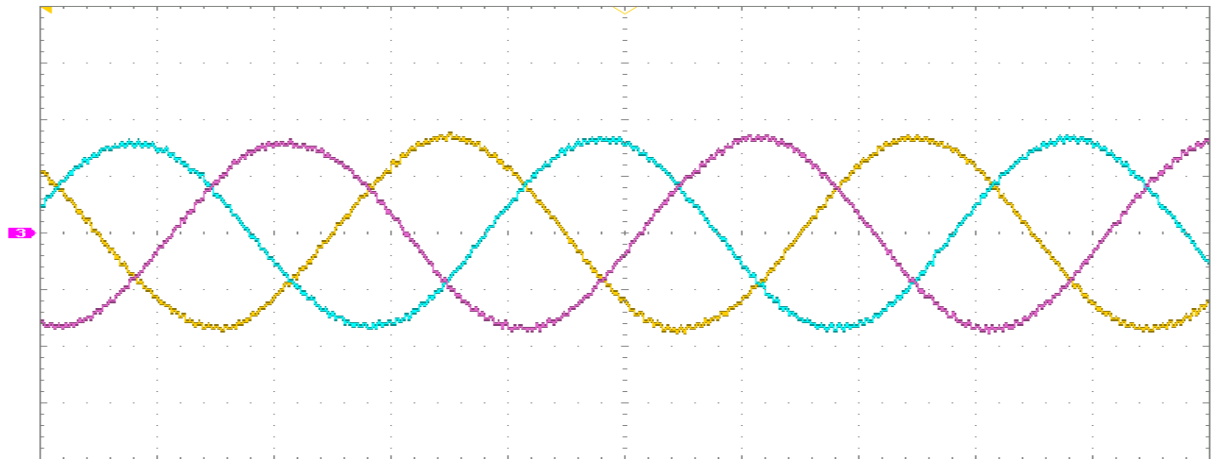
Figure 5.44 FS-MPVOC HIL responses of grid currents (10A/div)
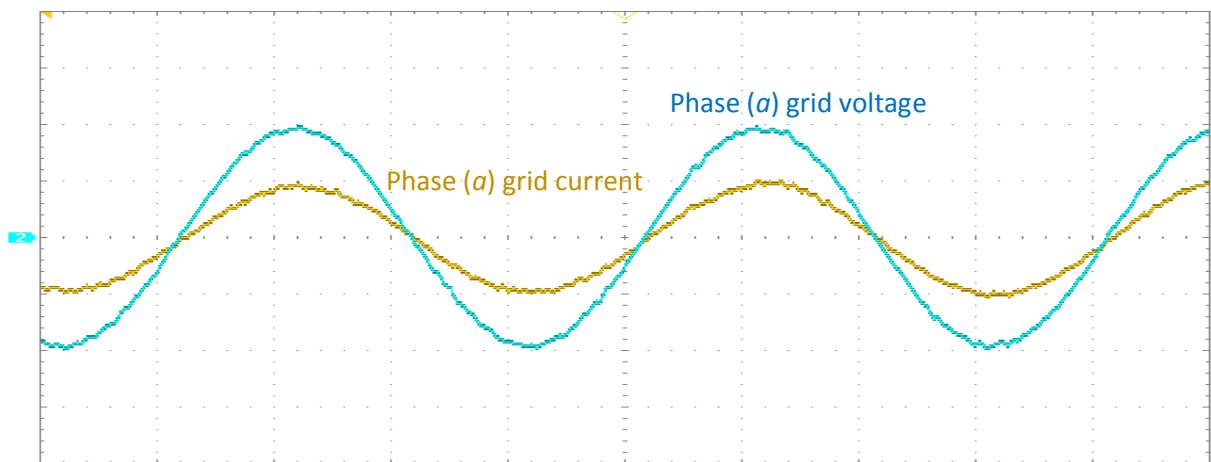
Figure 5.45 FS-MPVOC HIL responses of phase (a): grid current (20A/div) and grid voltage
(80V/div)

5.6.1.2 FS-MPDPC
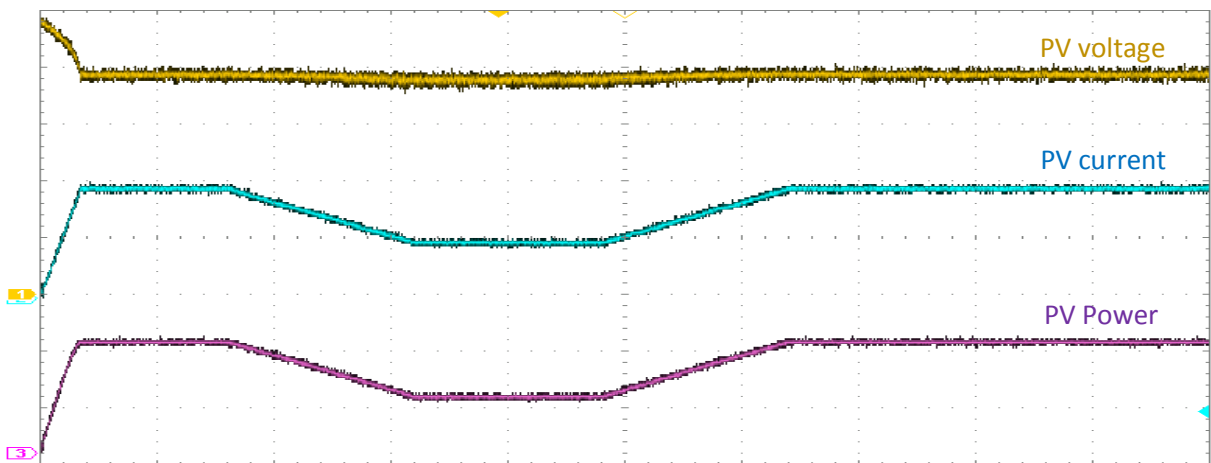
Figure 5.46 FS-MPDPC HIL responses of PV output: voltage (25V/div), current (10A/div), and power
(2kW/div)
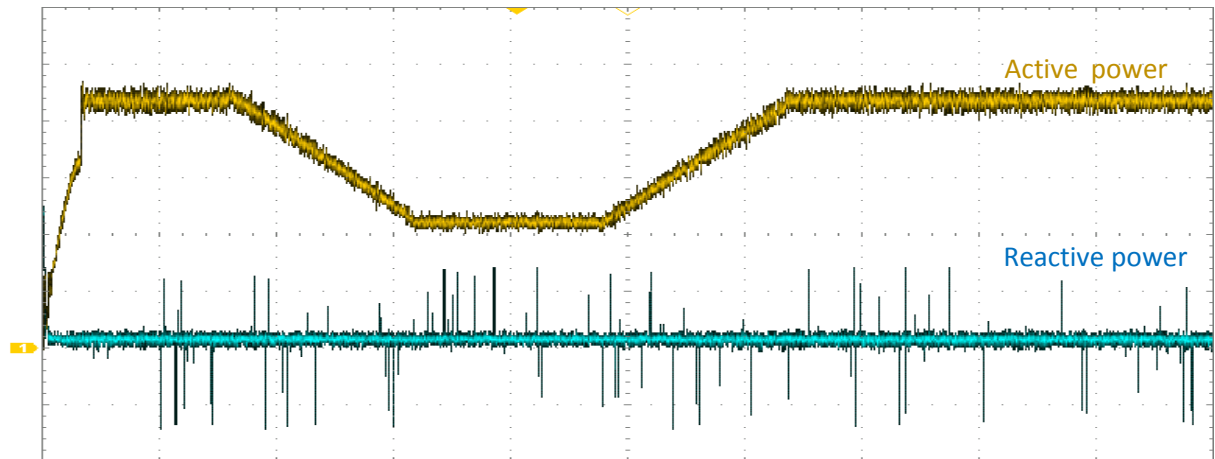
Figure 5.47 FS-MPDPC HIL responses of grid: active power (1kW/div) and reactive power (1kVAr/div)
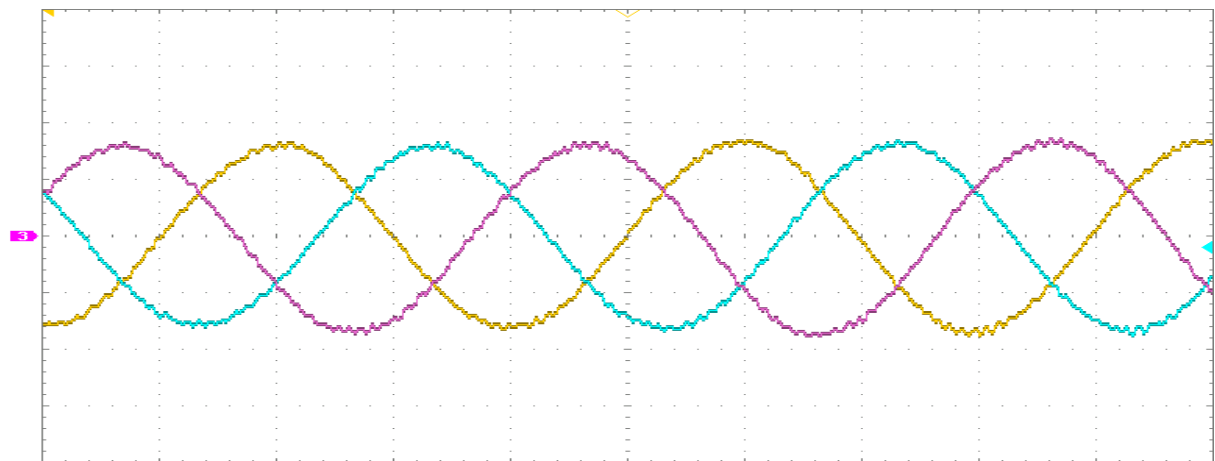
Figure 5.48 FS-MPDPC HIL responses of grid currents (10A/div)
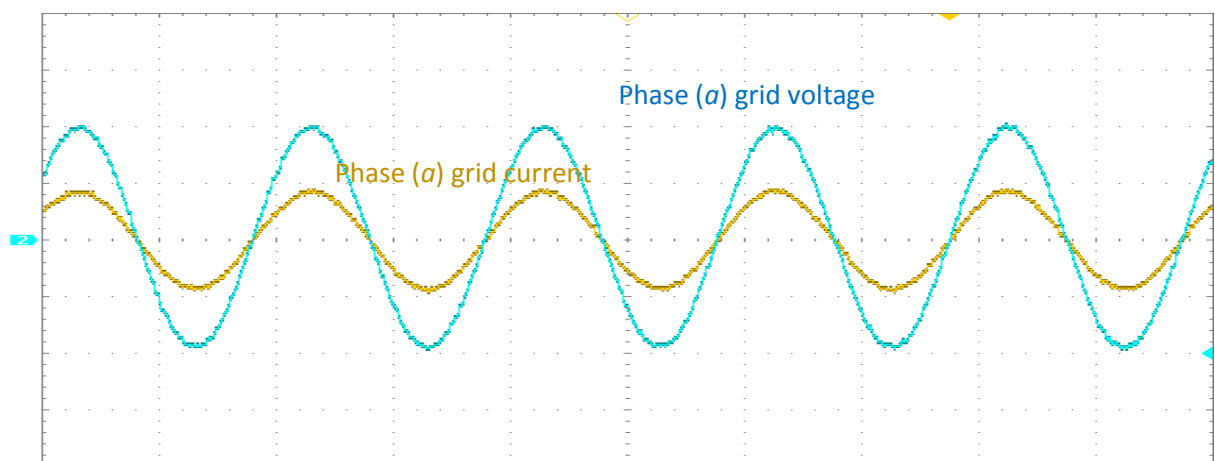
Figure 5.49 FS-MPDPC HIL responses of phase (a): grid current (20A/div) and grid voltage (80V/div)

5.6.2 Reactive power injection

5.6.2.1 FS-MPVOC
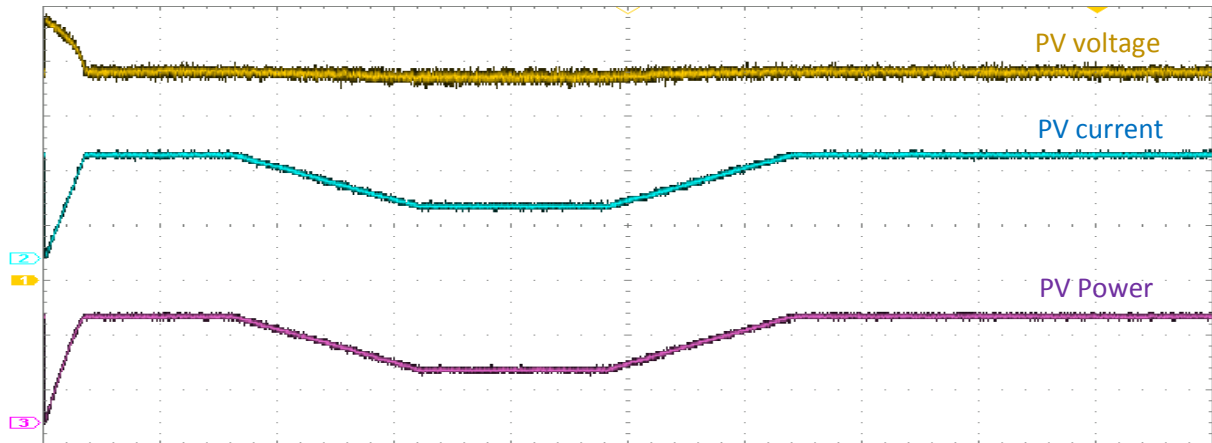
Figure 5.50 FS-MPVOC HIL responses of PV output: voltage (25V/div), current (10A/div), and power (2kW/div)
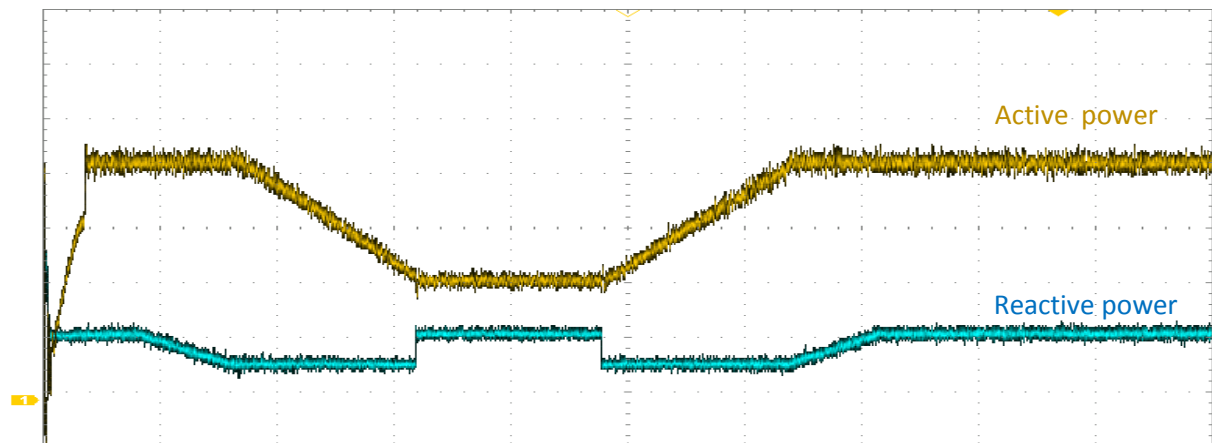
Figure 5.51 FS-MPVOC HIL responses of grid: active power (1kW/div) and reactive power (1kVAr/div)
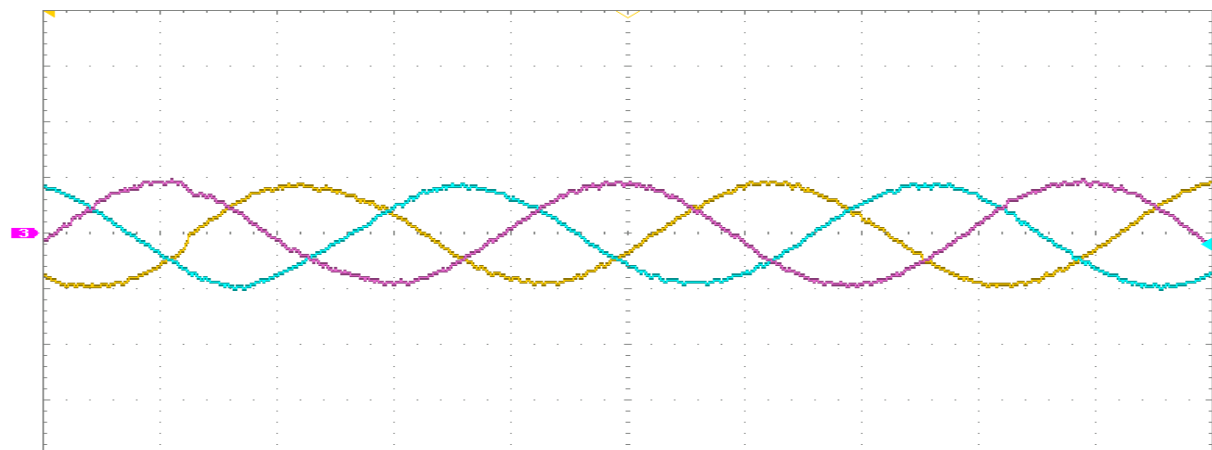
Figure 5.52 FS-MPVOC HIL responses of grid currents (20A/div)
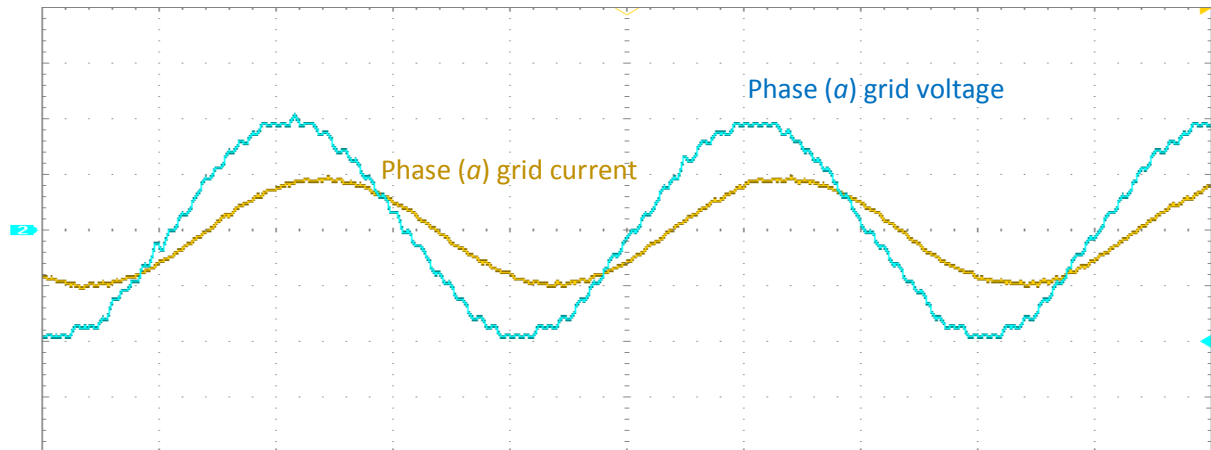
Figure 5.53 FS-MPVOC HIL responses of phase (a): grid current (20A/div) and grid voltage (80V/div)

5.6.2.2 FS-MPDPC
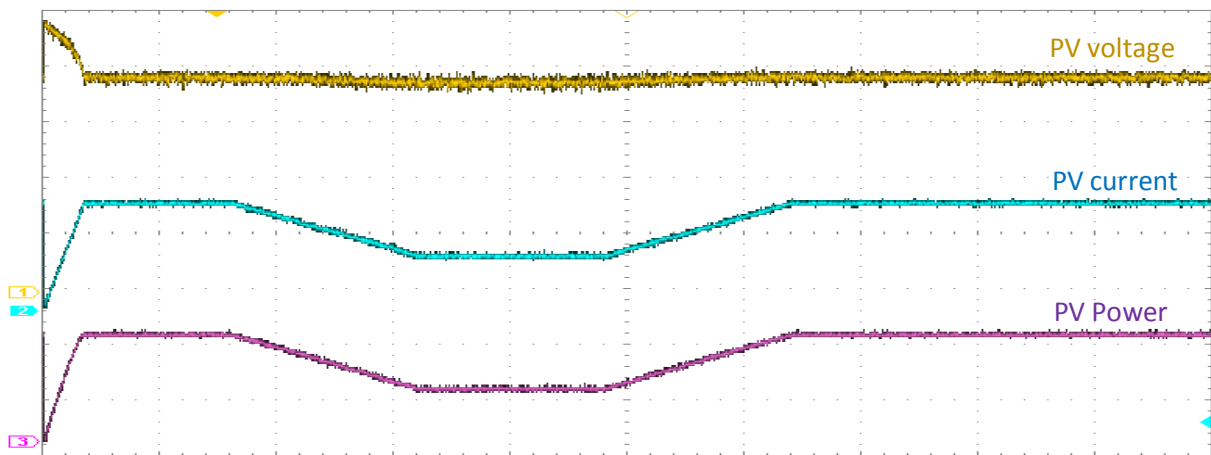
Figure 5.54 FS-MPDPC HIL responses of PV output: voltage (25V/div), current (10A/div), and power (2kW/div)
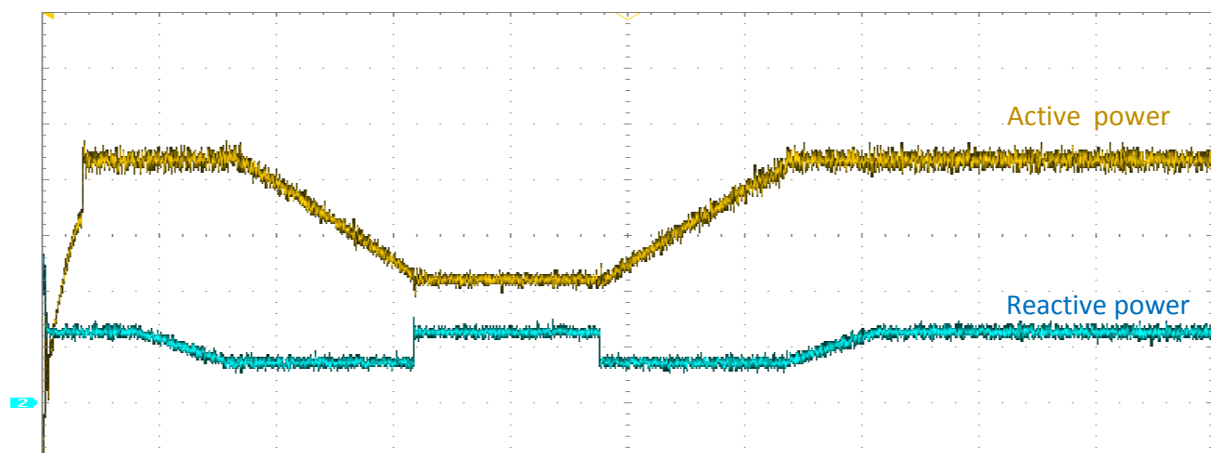

Figure 5.55 FS-MPDPC HIL responses of grid: active power (1kW/div) and reactive power (1kVAr/div)
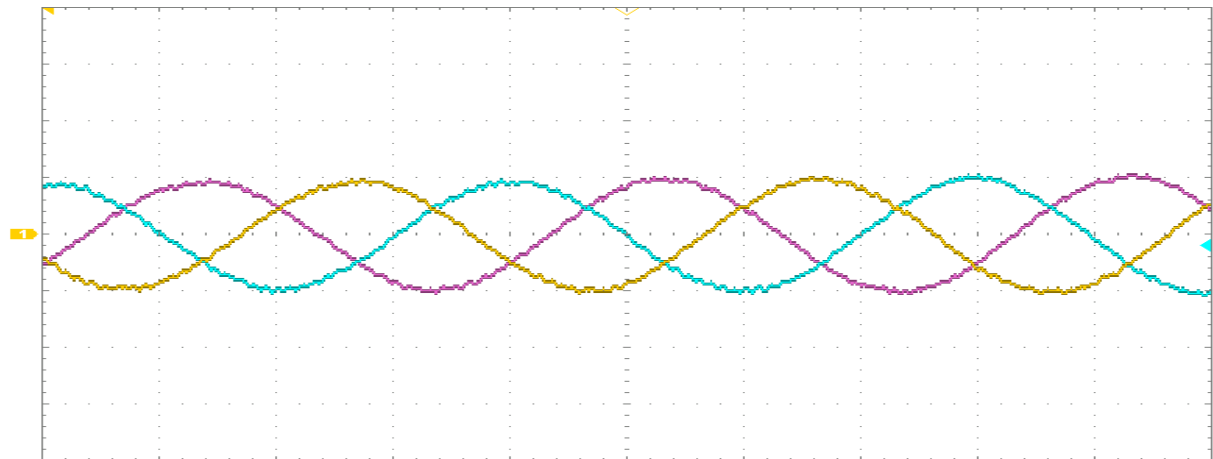
*Figure 5.56* FS-MPDPC HIL responses of grid currents (20A/div)
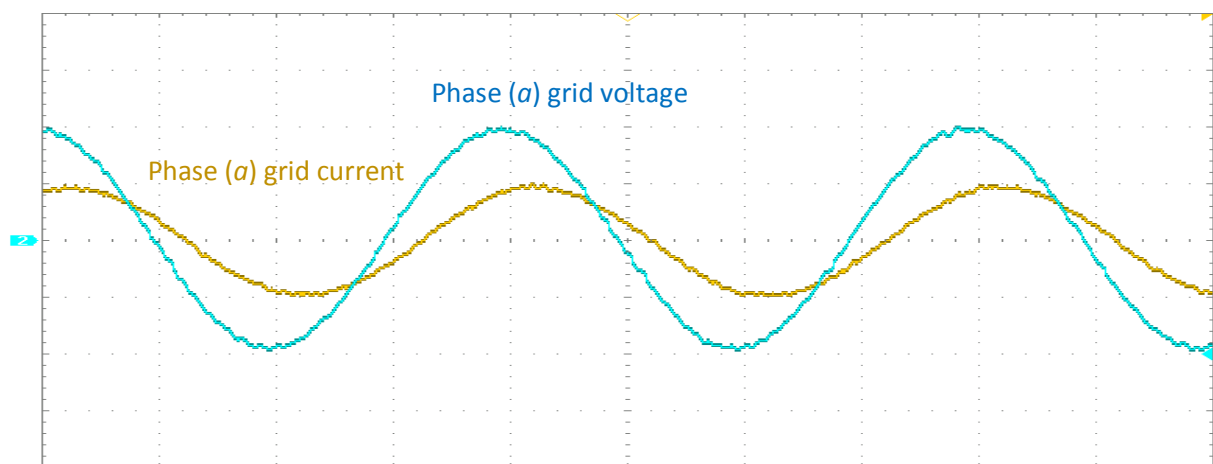
Figure 5.57 FS-MPDPC HIL responses of phase (a): grid current (20A/div) and grid voltage (80V/div)

The obtained RT-HIL implementation results prove the correctness and good performances of the proposed FS-MPVOC and FS-MPDPC techniques. The MPPT is achieved rapidly and accurately with low ripple at the MPP due to the effectiveness and fast dynamics of the controllers and the DC link regulators. Moreover, the PV power and grid active power are not affected by the grid reactive power, this is due to the decoupled control of grid active and reactive powers for both unity power factor operation, and reactive power injection cases. The grid current waveforms are sinusoidal and lowly distorted, and respond swiftly to irradiance variations and reactive power injection. As a conclusion, the obtained RT implementation results are in agreement with the previously exhibited simulation results, which demonstrates the correctness and effectiveness of the proposed control techniques, and proves the feasibility of implementation of the proposed techniques for the control of a real CSI based grid-connected photovoltaic system.

5.7 Conclusion

In this chapter two control strategies have been presented for single-stage configuration of grid-connected PV system based on CSI. The proposed techniques are both based on FS-MPC theory. The first studied technique named FS-MPVOC is achieved by combining VOC technique along with FS-MPVC reported in the previous chapter. It has been explained that FS-MPVOC controls the grid injected powers indirectly through the control of the currents in the synchronously reference *dq*-frame through two regulation loops, where the synchronization is ensured using a SRF-PLL. The second technique called FS-MPDPC is a combination of FS-MPC and DPC strategies. FS-MPDPC ensures a direct, natural decoupled control of the powers exchanged with the grid without the need of a PLL. To keep the PV array operating at the MPP, a P&O based MPPT algorithm is chosen due to the features it offers such like good performance and simplicity of implementation. The P&O algorithm is responsible for generating the reference of the PV current, which is then adjusted using a PI regulator that provides the reference of the *d*-axis current or the active power for the FS-MPVOC or FS-MPDPC, respectively. Moreover, in order to reduce system's cost and complexity and avoid sensors noise, a SMO is proposed to estimate the grid-side variables. Furthermore, due to presence of a *CL* filter at the output of CSI, resonance may occur. Therefore, an active damping method for each of the proposed control strategies is introduced instead of passive damping methods. Active damping increases the efficiency by eliminating the dissipative damping elements of the conventional passive damping, and enhances the quality of PV and grid powers. The obtained simulation and RT-HIL implementation results demonstrate the effectiveness of SMO, and exhibit the high performances of the proposed techniques in terms of fast dynamics, MPPT, and quality of grid powers for unity power factor operation, a reactive power injection cases.

References

[5.1]   D. Rekioua, E. Matagne, *Optimisation of Photovoltaic Power Systems: Modelisation, Simulation, and Control*. Springer-Verlag, 2012.

[5.2]   N. Femia, G. Petrone, G. Spagnuolo, M. Vitelli, *Power Electronics and Control Techniques for Maximum Energy Harvesting in Photovoltaic Systems*, CRC Press, 2013.

[5.3]   Y. Shtessel, C. Edwards, L. Fridman, A. Levant, *Sliding Mode Control and Observation*, Springer- birkhauser, 2014.

[5.4]   J. Rodriguez, F. Cortes, *Predictive Control of Power Converters and AC Drives*, John Wiley & Sons, Ltd, 2012.

[5.5]   V. Yaramasu, B. Wu, *Model Predictive Control of Wind energy Conversion Systems and AC Drives*, John Wiley & Sons, Ltd, 2017.

[5.6]   P. P. Dash, "A High-Performance Three-Phase Grid-Connected PV System Based On Multilevel Current Source Inverter," Ph.D. dissertation, Dept. of Elec. and Comp. Eng., Waterloo Univ., Waterloo, Canada, 2013.

[5.7]   B. Wu, Y. Lang, N. Zargari, S. Kouro, *Power Conversion and Control of Wind energy Systems*, John Wiley & Sons, Ltd, 2011.

[5.8]   H. Abu-Rub. M. Malinowski, K. Al-Haddad, Power Electronics for Renewable Energy Systems, Transportation, and Industrial Applications. John Wiley & Sons, Ltd, 2015.

[5.9]   Y. W. Li, "Control and Resonance Damping of Voltage-Source and Current-Source Converters With LC Filters," *IEEE Trans. on Industrial Electronics*, Vol. 56, No. 5, Nov. 2008, pp. 1511–1521

Chapter 6

Conclusion

6.1 General conclusion

After the energy crisis and environmental issues such as global warming and pollution, the development of renewable energy sources has attracted research attention. The penetration into the power grid of renewable power from resources such as solar, and wind energies has significantly increased. PV systems are considered to be one of the most efficient and well accepted renewable energy sources for small and large scale power generation, because of their suitability in distributed generation.

The main objective of this thesis is to make quality contributions in the field of power electronic interface for stand-alone and grid-connected PV systems. For this purpose, the less-investigated inverter topology, i.e., CSI was chosen. To make sure about the originality of the work and to avoid repetition of the past work, an extensive literature survey was carried out first. The literature survey covers a range of topologies employed for interfacing PVs. A part of literature survey focusses on existing control strategies and modulation techniques. Whereas the last part addresses grid-connected PV systems that incorporate CSI as their power conditioning unit. The survey was a useful way to determine the research gap in the field of CSIs for PV applications. In the third part of this work, the different components of the systems under study were designed and modeled. The PV array has been modeled using the well-known single diode equivalent electrical circuit. CSI working principles have been explained. Then, the possible switching states, space current vectors, and model of CSI have been presented. The design and modeling of the output filter for stand-alone mode and for grid-connected mode have been achieved as well.

In chapter four, stand-alone CSI is addressed. It has been proposed for this purpose two new voltage control techniques that control directly the voltage of CSI, i.e., they do not employ regulation loops and modulators as compared with the other techniques in the literature. Furthermore, they do not have need for information about the type of the load connected at the

terminals of the inverter. The performance of the two voltage control strategies were verified through Matlab/Simulink numerical simulations, and practical results.

Chapter five focused on the design of controllers for a three phase single-stage grid connected PV fed CSI. The design involved developing a DC-link current controller, which allowed MPPT. The MPPT is based on the widely-used Perturb & Observe algorithm and can track the MPP in the order of milliseconds. Two control techniques were proposed in this chapter as well. Firstly, FS-MPVOC technique is exhibited. This technique is based on VOC and MPC, where the control of currents or powers is done indirectly through two current loops in the rotating frame dq which is made to be aligned on the grid voltage vector, and rotating at the same angular frequency. Therefore, for converting the three phase state variables to their corresponding dq frame equivalents, the transformation angle is derived from the PLL. The grid current d-axis component is generated by the DC link PI regulator, whereas the q-axis current component can be kept equal to zero to achieve unity power factor operation, as it can have a value depending on the grid operator's demand, and grid codes. The two current PI regulators generate the reference voltages that are fed to the predictive voltage controller which is the same used for stand-alone mode. Secondly, a DPC and MPC based technique called FS-MPDPC is proposed. FS-MPDPC can ensure a direct decoupled control of active and reactive powers without the need of PLL. The active power reference is generated by the DC link PI regulator, and the reactive power is set to zero for unity power factor operation or to a defined value according to grid operator's demand or grid codes. The control of the powers is done using a prediction model to predict their future behavior, and a cost function that selects the best inverter switching combination. In order to reduce the cost and complexity of the system, a SMO is introduced to estimate the grid-side variables. Simulation results, and RT implementation results -using HIL technique- exhibit the effectiveness and the good performance of the proposed control strategies.

6.2 Author's contribution

The main contributions of this thesis can be summarized as follows:

- ✓ A comprehensive overview and study of CSI working principle, modeling, design, and existing modulation and control techniques have been carried out.

- ✓ Novel voltage control strategies for CSI have been proposed. Both can control the load voltage directly without any modulators or regulation loops and independently of the type of the load. The first strategy is based on MPC theory, where the model of the CSI including the output filter is derived and used for the predictions and a cost function for the selection of the optimal command. The second one is a control algorithm that uses the same model of the first technique but in other way in order to control the CSI. The proposed algorithm needs only the errors between the references and measured values of the three load voltages.

- ✓ A three phase single-stage grid connected PV system has been analyzed, and two control techniques have been proposed to ensure all the control objectives of the system. Both techniques are based on MPC. The first one is an indirect power control strategy based on VOC, where the control of the currents was performed in the rotating frame *dq* using two PI regulation loops that generate the reference voltages which are imposed by the predictive voltage controller. A direct decoupled power control strategy was the second proposed technique named as FS-MPDCP. It is based -as mentioned before- on MPC, and DPC. This technique employs the system's model to predict the powers exchanged with the grid, then through an optimization of a cost function the control signals are generated to the power switches of the inverter.

- ✓ A fast and accurate SMO observer is also presented in order to reduce the complexity and the cost of the system and avoid sensors noise. The proposed SMO uses only grid current to estimate the other grid-side variables.

- ✓ In order to increase the system efficiency and improve its performances, Resonance active damping methods have been also proposed instead of conventional passive damping methods.

6.3 Recommendations for future research

The following topics have not been covered and can serve as ideas for future work.

- ➢ Addressing voltage support techniques, and reactive power injection methods using CSI during grid faults, and unbalanced grid conditions.

- ➢ Development of improved MPPT algorithms that could increase the harvested energy from PV sources, and thus increasing the efficiency of the whole system.

The MPPT techniques that present a good way of research are those based on artificial intelligence method, like fuzzy logic, neuronal networks, genetic algorithms, and others.

➢ Investigation of the effect of partial shading of PV arrays on the proposed techniques in this thesis.

➢ Investigation of common-mode voltage of CSI that could be mitigated by the use of four legs topology of CSI. This concern has been well addressed for VSI-based topologies.

➢ Integration options of PVs using different current source inverter configurations could include parallel connection of CSIs (multi-level CSIs).

➢ Investigation of stand-alone photovoltaic storage pumping systems using CSI for water supply applications.

Appendix A

Systems' Parameters

A.1 Stand-alone system

Table A.1 Stand-alone system electrical circuit parameters

Quantity	Value
DC current I_{dc}	10 A
DC link inductor L_{dc}	50 mH
Capacitor filter C_f	150 μF
Load resistance R	22/44 Ω
Load inductance L	10 mH
Rectifier load resistance R_{rec}	100 Ω
Rectifier load capacitance C_{rec}	4.7 μF

A.2 Grid connected PV system

A.2.1 PV array parameters

Table A.2 PV module parameters

Quantity	Value
Power Rating P_{mp}	120 W
Open Circuit Voltage V_{oc}	42.1 V
Short Circuit Current I_{sc}	3.87 A
Voltage at Maximum Power V_{mp}	33.7 V
Current at Maximum Power I_{mp}	3.56 A
Maximum System Voltage V_{max}	600 V
Temperature Coefficient of I_{sc}	0.065 %/°C
Temperature Coefficient of V_{oc}	-0.38 %/°C
Temperature Coefficient of P_{mp}	-0.50 %/°C

Number of series connected cells N_{sc}	72
Number of parallel connected cells N_{pc}	1
Series resistance R_s	0.553
Parallel Resistance R_p	850

A.2.2 Grid connected CSI parameters

Table A.3 Grid connected CSI electrical circuit parameters

Quantity	Value
DC link inductor L_{dc}	50 mH
DC link inductor internal resistance R_{dc}	0.2 Ω
Capacitor filter C_f	150 µF
Filter inductance L_f	10 mH
Inductor filter internal resistance R_f	0.1 Ω
Grid voltage V_g	110 V_{rms}
Grid frequency f	50 Hz
Passive damping resistor R_d	50 Ω
Active damping virtual resistor used in FS-MPVOC R_{vd1}	5 Ω
Active damping virtual resistor used in FS-MPDPC R_{vd2}	50 Ω

Appendix B

Experimental hardware design

B.1 Stand-alone CSI experimental test bench

Figure B.1 show the stand-alone system test bench using a low power CSI prototype. The DC programmable power source is programmed to supply a constant DC current, and the DC link inductor is used to further smooth the DC link current. The DSP of Texas instruments (TI F28M36x) is programmed using Matlab® Embedded Coder at a sampling time of 40μs.
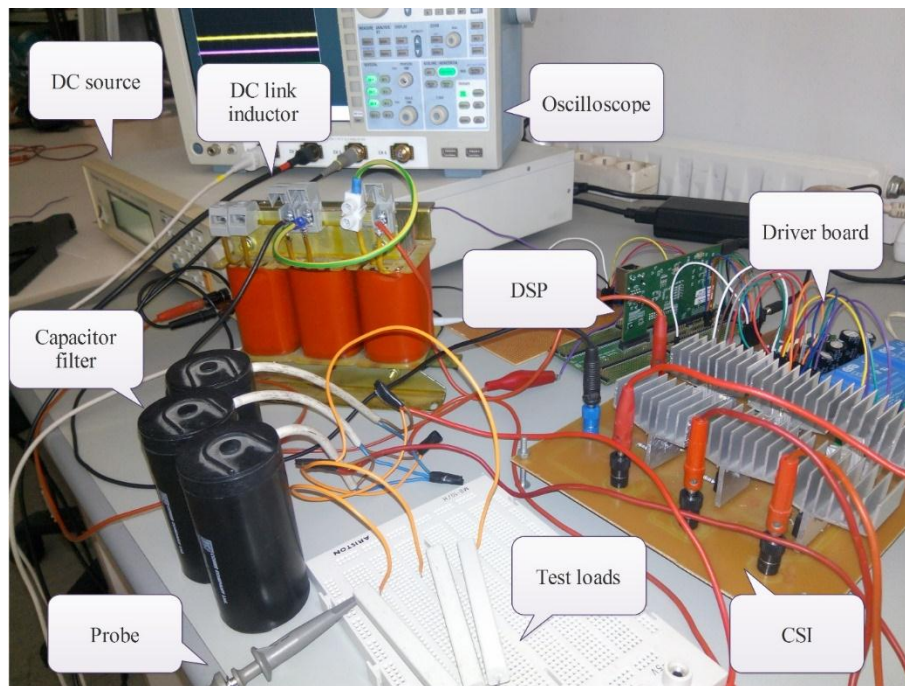
Figure B.1 Experimental stand-alone CSI test bench

B.2 CSI prototype design

Figure B.2, and B.3 show the printed circuit board (PCB) design of CSI power circuit in ISIS/ARES platform, and the two sides of the PCB of the CSI prototype, respectively. The CSI prototype consists of six unidirectional switches (IGBT is series with a diode). The IGBTs are triggered through a gate resistor.

The CSI driver board (Figure B.5) that ensures a galvanic isolation between the power circuit and the DSP is designed in ISIS/ARES software as shown if Figure B.4.
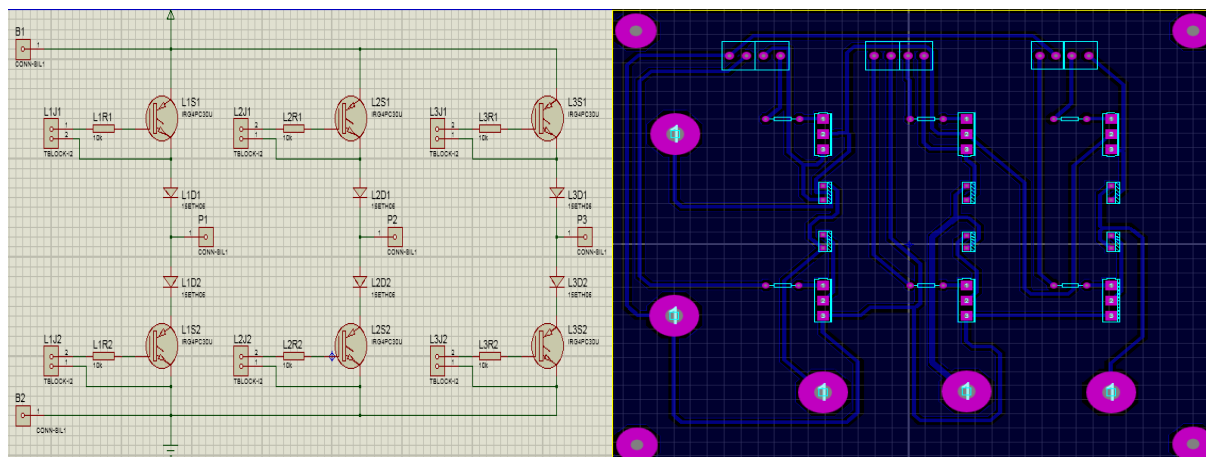
Figure B.2 CSI electrical circuit design in ISIS/ARES software
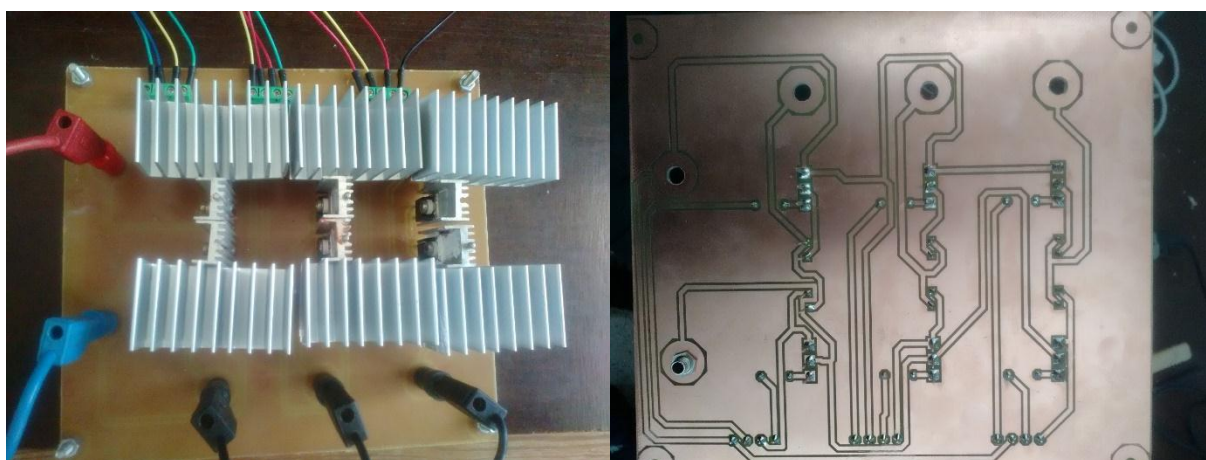
Figure B.3 Both sides of CSI prototype

The driver board consists of six optocoupler drivers supplied by four isolated DC voltages of 15 V. Three of which, are used for the supply of the drivers connected with CSI upper switches. Whereas, the fourth is used for lower switches drivers, since they have same ground connection.

Figure B.4 CSI driver board design in ISIS/ARES software
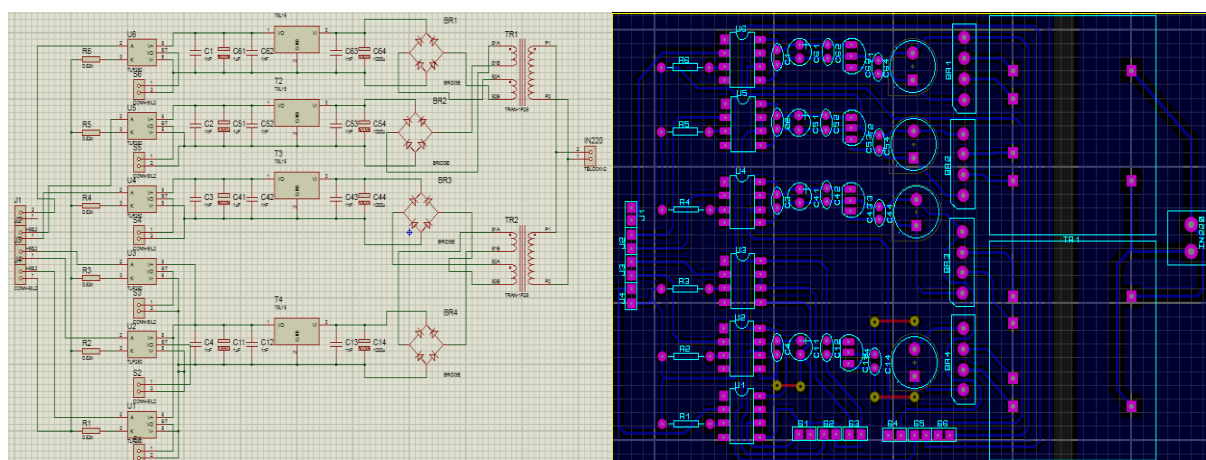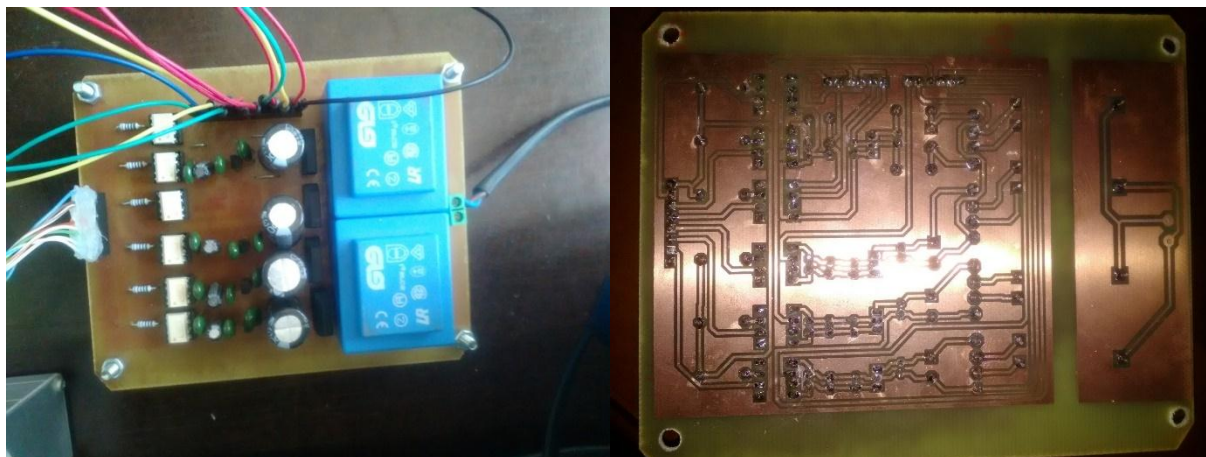
Figure B.5 Both sides of CSI driver board

Table B.1 References of important components used in experiments

Component	Reference
DSP	TI f28M36x concerto
IGBT	IRG4PC30U
Diode	15ETX06
Optocoupler/Driver	TLP250
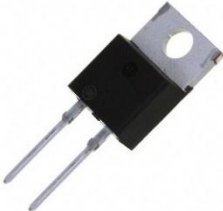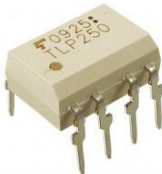
Scientific productions

❖ *Journal papers*

[1] **Hamza Feroura**, Fateh Krim, Billel Talbi, Abdelbaset Laib, Abdesslam Belaout, "Finite-Set Model Predictive Direct Power Control of Grid Connected Current Source Inverter," *Elektronika ir Elektrotechnika*, Vol. 23, No. 5, Oct. 2017. http://dx.doi.org/10.5755/j01.eie.23.5.19240

[2] **Hamza Feroura**, Fateh Krim, Billel Talbi, Abdelbaset Laib, Abdesslam Belaout, "Sensorless field oriented control of current source inverter fed induction motor drive," *Rev. Roum. Sci. Techn. – Électrotechn. et Énerg.*, Vol. 63, No. 1, Apr. 2018.

[3] Billel Talbi, Fateh Krim, Toufik Rekioua, Abdelbaset Laib, **Hamza Feroura**, "Design and hardware validation of modified P&O algorithm by fuzzy logic approach based on model predictive control for MPPT of PV systems," *Journal of Renewable and Sustainable Energy*, Vol. 9, No. 4, Aug. 2017. http://dx.doi.org/10.1063/1.4999961

❖ *International conferences*

[1] **Hamza Feroura**, Fateh Krim, Billel Talbi, Abdelbaset Laib, "Photovoltaic grid connected current source inverter with resonance active damping method," *Proc. ICENT'17*, M'sila, Algeria, Nov. 2017.

[2] **Hamza Feroura**, Fateh Krim, Billel Talbi, Abdelbaset Laib, "Finite-set model predictive voltage control for islanded three phase current source inverter," *Proc. ICEE'17*, Boumerdes, Algeria, Oct. 2017.

[3] **Hamza Feroura**, Fateh Krim, Billel Talbi, Abdelbaset Laib, Abdesslam Belaout "Finite-set model predictive direct power control of grid connected current source inverter," *Proc. 21st international conference electronics*, Lithuania, Jun. 2017.

[4] **Hamza Feroura**, Fateh Krim, Billel Talbi, "A fuzzy logic control strategy for three phase current source inverter based on model predictive current control," *Proc. CEE'16*, Batna, Algeria, Oct. 2016.

[5]   **Hamza Feroura**, Khouni Larbi, Fateh Krim, "Improved control strategy for three phase current source inverter with fuzzy logic controller based on lyapunov's direct method," *Proc. ICATS'15*, Annaba, Algeria, Nov. 2015.

[6]   Billel Talbi, Fateh Krim, Abdelbaset Laib, **Hamza Feroura**, "High-accuracy sliding mode observer for boost converter with MPC switching control," *Proc. ICENT'17*, M'sila, Algeria, Nov. 2017.

[7]   Abdelbaset Laib, Fateh Krim, Billel Talbi, **Hamza Feroura**, "Current oriented MPPT based on fuzzy logic and predictive controllers for photovoltaic systems with SEPIC converter," *Proc. ICENT'17, M'sila*, Algeria, Nov. 2017.

[8]   Abdelbaset Laib, Fateh Krim, Billel Talbi, **Hamza Feroura**, "Fuzzy logic maximum power point tracking through sliding mode current control for PV systems," *Proc. IC-AIRES'17*, Tipaza, Algeria, Oct. 2017.

[9]   A. Belaout, F. Krim, B. Talbi, **H. Feroura**, A. Laib, S. Bouyahia, A. Arabi, "Development of real time emulator for control and diagnosis purpose of Photovoltaic Generator," *Proc. ICSC'17*, Batna, Algeria, May. 2017.

[10]   Billel Talbi, Fateh Krim, **Hamza Feroura**, "Modified P&O algorithm by Takagi-Sugeno fuzzy logic approach for MPPT of PV systems," *Proc. ICATS'15*, Annaba, Algeria, Nov. 2015.

[11]   Billel Talbi, Fateh Krim, **Hamza Feroura**, "Predictive torque and flux control for three-phase induction motor," *Proc. IECEC'15*, Setif, Algeria, Oct. 2015.

❖ *Other events*

[1]   **Hamza Feroura**, Fateh Krim, "Conception et réalisation d'un onduleur de courant triphasé pout les systèmes photovoltaiques," *Doctoriales de l'UFAS1 dédiées à l'innovation*, Setif, Algeria, May. 2016.

Abstract

Current Source Inverter (CSI) topology is gaining acceptance as a competitive alternative for grid interface of renewable energy systems due to its unique and advantageous features. Merits of CSI over the more popular voltage source inverter (VSI) topology have been elaborated on by a number of researchers. However, there is a lack of quality work in control strategies of CSI topology for both stand-alone and grid connected modes. Therefore this thesis contributes by proposing new voltage control techniques, and power control techniques for stand-alone and grid-connected modes, respectively. Existing voltage control techniques for stand-alone CSI are conventional, and complex. They employ usually modulators and regulation loops which are designed depending on the connected load, this reduces the accuracy and stability of the controllers. For this reason, two direct voltage control methods have been proposed in this work. The proposed methods overcome the aforementioned drawbacks of conventional methods. In the other side, PV grid connected CSI systems available in the literature suffer from many problems such like complexity of control strategies, poor power control, filter resonance, and low efficiency. Therefore, new high-performance control strategies are introduced to get over these problems. The proposed techniques can fulfill all the control objectives of the system, i.e. fast and accurate maximum power point tracking, decoupled control of active and reactive powers exchanged with the grid, low distorted grid currents, unity power factor operation or reactive power injection, depending on grid operator demand, and high efficiency through the use of active damping methods. Moreover, system cost and complexity are reduced, and better performances are reached by the use of a sliding mode observer (SMO) instead of hardware sensors. Simulation results using Matlab/Simulink, experimental results, and real-time (RT) implementation results have been carried out to assess the different control techniques proposed in this thesis.

Keywords: Renewable energies, PV systems, CSI, stand-alone mode, grid connected mode, active resonance damping, SMO.

Résumé

La topologie de l'onduleur de courant est de plus en plus acceptée comme une alternative compétitive pour l'interface au réseau des systèmes d'énergie renouvelable en raison de ses caractéristiques uniques et avantageuses. Les avantages de l'onduleur de courant face à l'onduleur de tension qui présente la topologie la plus connu, ont été élaborés par un nombre de chercheurs. Cependant il existe un manque de travail de qualité concernant les stratégies de commande de ce type d'onduleur. Pour cela, cette thèse contribue en proposant de nouvelles techniques de contrôle de tension, et contrôle de puissance ou de courant pour les onduleurs de courant autonome, et ceux connecté au réseau, respectivement. Les techniques de contrôle de tension pour les onduleurs de courant sont conventionnelles, et complexes. Ils emploient généralement des boucles de régulation et des modulateurs qui sont conçus en fonction de la charge connectée. Cela réduit la précision et la stabilité des contrôleurs. Pour cette raison, deux méthodes de contrôle de tension sont proposées dans ce travail. Les méthodes proposées surmontent les inconvénients précédemment cités des méthodes classiques. D'autre côté, les systèmes photovoltaïque connectés au réseau à base de l'onduleur de courant qui sont disponibles dans la littérature souffrent de nombreux problèmes tels que la complexité des stratégies de contrôle, la mauvaise maitrise des puissances, la résonance du filtre, et la faible efficacité. Pour cette raison, de nouvelles stratégies de commande de haute performance sont introduites surpasser ces problèmes. Les techniques proposées peuvent s'acquitter de toutes les objectifs de contrôle du système, c.-à-d. rapidité et précision lors de la poursuite du point maximale de puissance, contrôle découplé des puissances active et réactive échangées avec le réseau, faible distorsion des courants du réseau, facteur de puissance unitaire ou injection de puissance réactive, en fonction de la demande de l'opérateur du réseau, une grande efficacité grâce à l'utilisation de méthodes d'amortissement actif de résonance. De plus, le coût du système et la complexité sont réduits, et de meilleures performances sont obtenues par l'utilisation d'un observateur en mode de glissement au lieu des capteurs. Des résultats de simulation à l'aide de la plate-forme Matlab/Simulink, des résultats expérimentaux, et des résultats de simulation en temps réel ont été effectués afin d'évaluer les différentes techniques de contrôle proposées dans cette thèse.

Mots clés: Energies renouvelables, systèmes photovoltaïques, onduleur de courant, onduleur autonome, onduleur connecté au réseau, amortissement actif de résonance, observateur à mode de glissement

ملخص

عاكس الموجة المغذى بمصدر تيار يحظى بقبول كبديل لعاكس الموجة المغذى بمصدر توتر ليكون كواجهة وصل بين مصادر الطاقات المتجددة و الشبكة الكهربائية نظرا لمميزاته المفيدة و الفريدة. مميزات هذا العاكس تم التطرق إليها من عدد من الباحثين. لكن رغم ذلك هنالك نقص في إستراتيجيات التحكم لهذا النوع من العواكس. من أجل هذا, هذه الأطروحة تساهم بإقتراح تقنيات تحكم جديدة. فيما يخص العواكس المستقلة أو المربوطة مع الشبكة. طرق التحكم الموجودة حاليا قديمة و معقدة نظرا لإستعمالها مغيرات و حلقات تنظيم. لتصميم هذه الأخيرة يجب معرفة نوع الحمولة الموصولة. الطرق المقترحة تتميز بكونها تلغي هذه السلبيات. من جهة أخرى أنظمة الطاقة الشمسية المتصلة بالشبكة عن طريق عواكس التيار الموجودة في المراجع تعاني من عدة مشاكل أبرزها التعقيد في طرق التحكم, عدم التحكم الجيد في الطاقات, الرنين في الفلتر, و المردودية الضعيفة. لهذا السبب, تم إقتراح نوعين جديدين من إستراتيجيات التحكم للتغلب على هذه المشاكل. هذه الإستراتيجيات تحقق كل أهداف النظام كتتبع القيمة الأعظمية للطاقة, تأمين تحكم منفصل للطاقتين النشيطة و المفاعلة, حقن تيارات حسنة سواء بمعامل جودة أحادي أو بحقن طاقة مفاعلة إعتمادا على الطلب, و تخميد نشيط للرنين في الفلتر, بالإضافة إلى هذا تم تصميم مراقب إنزلاقي بدلا من المستشعرات المادية وهذا من أجل تقليص ثمن و تعقيد النظام. كل التقنيات المقترحة تم تقييمها عن طريق المحاكاة ببرنامج ماتلاب, و نتائج تطبيقية و محاكاة في الوقت الحقيقي.

كلمات مفتاحية: مصادر الطاقات المتجددة, أنظمة الطاقة الشمسية, عاكس التيار, العواكس المستقلة, العواكس المربوطة مع الشبكة, تخميد نشيط للرنين, مراقب إنزلاقي.